Magnetic Field Simulation and Mapping for the Q^{p}_{Weak} Experiment

by

Peiqing Wang

A Thesis

Submitted to the Faculty of Graduate Studies

in Partial Fulfillment of the Requirements

for the Degree of

Master of Science

Department of Physics and Astronomy

University of Manitoba

Winnipeg, Manitoba, Canada

Acknowledgments

I would like to thank these people who have provided support, encouragement, guidance and assistance in the preparation of this thesis.

First and foremost, my extra special thanks goes to my supervisor, Dr. Shelley Page, who has provided me with the opportunity to work in the subatomic group and offered insight and guidance for my work in experimental physics. My extra special thanks also goes to my thesis advisor, Dr. Willie Falk, who has been abundantly helpful, and has assisted me in the details of my research and thesis.

Then, I would like to greatly thank Dr. Lawrence Lee for being my summer research mentor, Dr. Jeffery Martin for passing on numerous hand-on experiences to me, Dr. James Birchall for giving me many advices. Without the generous help of these individuals, this thesis would not have been possible. I would also like to extend my extra special thanks to my family and friends for the support over the years.

Finally, NSERC Canada is gratefully acknowledged for funding the experiment.

Abstract

The Q^p_{Weak} experiment at Thomas Jefferson National Accelerator Facility (Jefferson Lab) will measure the proton's weak charge by measuring the parity violating asymmetry in elastic electron-proton scattering at very low momentum transfer $Q^2 = 0.03$ (GeV/c)^2, with the aim of determining the proton's weak charge with 4% combined statistical and systematic errors. The experimental apparatus includes a longitudinally polarized electron beam, a liquid hydrogen target, a room temperature toroidal magnetic spectrometer, and a set of precision detectors for the scattered electrons. The toroidal magnetic spectrometer, which will deflect away the inelastic scattered electrons and focus the elastic scattered electrons onto the detectors, plays a crucially important role in the experiment. In this thesis, in order to meet the requirements for the installation and calibration of the toroidal magnetic spectrometer, the numerical simulation of the spectrometer's magnetic field based on a realistic magnet model is discussed, a precise 3D field mapping is introduced, and some simulation results are provided. The zero-crossing analysis technique, which can be used to precisely infer the individual coil locations of the toroidal magnet, is presented and explored in detail.

Table of Contents

1 Introduction **1**

1.1 Background and Scientific Motivation 1

1.1.1 The Standard Model 1

1.1.2 Electroweak Interaction 5

1.1.3 Parity Violating Electron-Proton Scattering 7

1.1.4 Running of the Electroweak Mixing Angle 12

1.2 Experiment Overview 16

1.2.1 Basic Requirements 16

1.2.2 Experimental Setup 18

1.2.3 Experimental Sensitivity 21

2 QTOR Magnet **24**

2.1 The Toroidal Magnetic Spectrometer 24

2.2 The Design and Manufactured QTOR Coils 34

2.3 Motivation for the Magnetic Field Simulation and Mapping 37

3 Calculating the Magnetic Field **41**

3.1 Basic Functions and Algorithms 41

3.1.1 The Functions of the Simulation Programs 41

3.1.2 Basic Algorithms 42

3.2 Realistic Model of the QTOR 45

3.2.1 Coordinate Systems 46

3.2.2 Procedure of Setting up a Realistic Model 48

3.2.3 Modeling the Shape of the Coils 58

3.2.4 Correction for Thermal Effects 62

3.3 Simulation Programs 66

3.4 Calculation Results 68

3.4.1 General Behavior of the Magnetic Field . . . 68
3.4.2 Zero-Crossing Points . . . 74
3.4.3 Field Symmetry . . . 74
3.4.4 The Scattered Electron Trajectories . . . 79
3.4.5 Effects of the Field Mapper Misalignments . . . 79
3.4.6 Effects of Coil Displacements . . . 82
3.5 Accuracy of Approximations in the Magnetic Field Calculations . . . 85
3.5.1 Assessment of the Validity of Approximations . . . 86
3.5.2 Uncertainties of the Magnetic Field Calculation . . . 89
3.5.3 Uncertainties in Zero-Crossing Points . . . 91

4 Magnetic Field Mapping 94
4.1 Basic Requirements for the Field Mapping . . . 94
4.2 Field Mapper . . . 95
4.2.1 Field Mapping Device . . . 96
4.2.2 Supervisory Control and Data Acquisition Software . . . 99
4.3 Field Mapping Procedure . . . 102
4.4 Field Mapping Issues . . . 106

5 Analyzing Zero-Crossing Measurements 108
5.1 Zero-Crossing Methodology . . . 108
5.2 Algorithms . . . 112
5.2.1 Zero-Crossing Displacement Vector . . . 112
5.2.2 Sensitivity Matrix . . . 112
5.2.3 Solving the Linear Equations . . . 117
5.3 Demonstration of the Zero-Crossing Technique . . . 118

6 Summary and Conclusion 120

Appendices 127

A Original QTOR Design Drawings 127

B Dimensions of the Manufactured Coils 134

C Directional Vectors and Derivatives for Hall Probe Misalignments 138

D The Q^{p}_{Weak} Collaboration 143

List of Figures

1.1 An electron and its mirror image 9
1.2 Electron-proton scattering process 10
1.3 The running of $\sin^2 \theta_W$ 14
1.4 The experiment apparatus 19
1.5 Elastic event distribution 20

2.1 A typical toroidal magnet 25
2.2 Q^p_{Weak} toroidal magnet 26
2.3 An electron's trajectory in the Q^p_{Weak} toroidal field 27
2.4 Deflection of electron in a magnetic field 28
2.5 The azimuthal magnetic field components 29
2.6 Electron separation and focusing 30
2.7 Electron distribution (beam's eye view) 32
2.8 Electron distribution in one octant 33
2.9 Coil winding effects 35
2.10 A manufactured coil 35
2.11 Coil specifications 36
2.12 Pancake widths 37
2.13 Pancake lengths 38
2.14 Effect of displacing one coil radially 40
2.15 Effect of rotating coil 40

3.1 TOROID/lab frame 46
3.2 Coils and coil carriers 47
3.3 Sector N frame 47
3.4 Current element 49
3.5 Initial placement of pancakes 50
3.6 Initial placement of coils (isometric view) 50

3.7 Initial placement of coils (looking downstream) 51
3.8 Shift of current element 51
3.9 QTOR shifted along X 56
3.10 QTOR rotation 56
3.11 Final positions of coils 57
3.12 Leads and jumpers 57
3.13 Straight and curved sections of pancakes 59
3.14 Differential arc length 60
3.15 Intervals of pancake straight sections 61
3.16 Dot-matrix representation of the QTOR 63
3.17 Dot-matrix representation of a coil 64
3.18 Dot-matrix representation of connections 65
3.19 The order of coils 69
3.20 A "cut-view" of the QTOR along the X-Z plane 70
3.21 B_ϕ on the $\phi = 0$ plane 71
3.22 B_r on the $\phi = 0$ plane 71
3.23 B_z on the $\phi = 0$ plane 72
3.24 B_x on an upstream $z = -190$ cm plane 72
3.25 B_y on an upstream $z = -190$ cm plane 73
3.26 B_z on an upstream $z = -190$ cm plane 73
3.27 Positive and negative B_x regions on an upstream $z = -190$ cm plane 75
3.28 Zero-crossing points for B_x components 75
3.29 Positive and negative B_y regions on an upstream $z = -190$ cm plane 76
3.30 Zero-crossing points for B_y components 76
3.31 Positive and negative B_z regions on an upstream $z = -190$ cm plane 77
3.32 Zero-crossing points for B_z components 77
3.33 Field difference between sector 1 and sector 5 78
3.34 Averaged electron trajectory positions 78
3.35 Trajectory intersections ($\theta = 6^o$ and $\phi_{sector} = 0^o$) 80
3.36 Trajectory intersections ($\theta = 12^o$ and $\phi_{sector} = 10^o$) 80
3.37 Zero-crossing positions in different scan-planes (nominal coil placement) 83
3.38 Variation of the distances between $B_y = 0$ points with scan planes 83
3.39 B_y zero-crossing positions (random coil placement) 86
3.40 Coordinate system for magnetic field calculation of a conductor element 88
3.41 Dot-matrix representation of the conductor cross section 88
3.42 Magnetic field comparison for different sized current elements 90

3.43 An uncertainty map on the X-Z plane 92
3.44 An uncertainty map on $z = -190$ cm plane 92

4.1 Measuring the field of QTOR 97
4.2 Front view of probe assembly 98
4.3 Side view of probe assembly 98
4.4 Layout of the control system 100
4.5 Main graphical user interface of MaVeriK 103
4.6 Scan lines 104

5.1 Coil location parameters 110
5.2 Misalignment angles for Hall probe 115
5.3 Reproduction of coil displacements 119

A.1 Cross-section of the copper conductor 128
A.2 Layer-1 coil conductor layout 129
A.3 Layer-2 coil conductor layout 130
A.4 Coil assembly diagram 131
A.5 Inter-pancake connection pieces 132
A.6 Inter-coil connection elements 133

B.1 Coil dimension measurement 137

List of Tables

1.1 The generations of matter 2
1.2 Basic parameters of the Q^p_{Weak} experiment 21
1.3 The anticipated experimental uncertainties 22

3.1 The current element displacements and unit vector changes for coil rotations 53
3.2 Corresponding coil shifts for 1 unit QTOR shift 54
3.3 Distances between $B_y = 0$ points 84
3.4 Coil displacement parameters 85
3.5 Uncertainties of zero crossing positions 93

4.1 Selection of scan directions and zero-crossing points 105

5.1 Hall probe misalignment parameters 115

C.1 Directional vectors for Hall probe 1 139
C.2 Directional vectors for Hall probe 2 140
C.3 Hall probe misalignment derivatives (upstream end of QTOR) 141
C.4 Hall probe misalignment derivatives (downstream end of QTOR) 142

Chapter 1

Introduction

The proton's weak charge (Q_W^p) is a basic property of the proton, which determines how a proton responds to the weak interaction — in a similar fashion, the proton's electric charge determines how a proton responds to the electromagnetic interaction. The proton's weak charge can be predicted with great accuracy in the Standard Model of elementary particle interactions. A precise measurement of Q_W^p will enable us to test whether the Standard Model in fact provides an exact description of the weak interaction or whether an important "new physics" process remains to be accounted for. The Q_{Weak}^p collaboration at Jefferson Laboratory[1] is developing an experiment which will precisely measure the parity violating asymmetry in elastic electron-proton scattering in order to determine the proton's weak charge. This chapter gives a brief introduction to the proposed Q_{Weak}^p experiment.

1.1 Background and Scientific Motivation

1.1.1 The Standard Model

Developed at the beginning of 1970's, the well known Standard Model is a simple and comprehensive theory that addresses questions, which have been long asked, such as: "what is our world made of?" and "what holds it together?". As one of the greatest achievements of physics in the

[1] See Appendix D for a collaboration list.

twentieth century, this theory successfully incorporates quantum electrodynamics (QED), quantum chromodynamics (QCD) and the electroweak theory. The Standard Model asserts that the fundamental particles that make up all matter are quarks and leptons, and they interact through the strong, weak, and electromagnetic fundamental interactions by exchanging force carrier particles.

Fundamental building blocks of matter

Today, we know of 6 quarks, which are: u (up quark), d (down quark), c (charm quark), s (strange quark), t (top quark), b (bottom quark), and 6 leptons, which are: e (electron), ν_e (electron neutrino), μ (muon), ν_μ (muon neutrino), τ (tau), and ν_τ (tau neutrino), as well as their anti-particles. These quarks and leptons are spin 1/2 fermions. They are all point-like particles, and no excited states have been observed so far. Thus they are considered to be the most elementary particles of matter, and are grouped into so-called "generations" according to increasing mass (see Table 1.1).

Fermions	Generation			bosons	
	I	II	III		
Quarks	up **u** 0.003 GeV/c^2 +2/3	charm **c** 1.3 GeV/c^2 +2/3	top **t** 175 GeV/c^2 +2/3	photon γ 0 0	Force Carriers (spin=1)
(spin=1/2)	down **d** 0.006 GeV/c^2 -1/3	strange **s** 0.1 GeV/c^2 -1/3	bottom **b** 4.3 GeV/c^2 -1/3	gluon **g** 0 0	
Leptons	electron neutrino ν_e $< 1 \times 10^{-8}$ GeV/c^2 0	muon neutrino ν_μ < 0.0002 GeV/c^2 0	tau neutrino ν_τ < 0.02 GeV/c^2 0	Z boson **Z^0** 91.187 GeV/c^2 0	
(spin=1/2)	electron **e** 0.00051 GeV/c^2 -1	muon μ 0.106 GeV/c^2 −1	tau τ 1.7771 GeV/c^2 −1	W boson **$W^\pm$** 80.4 GeV/c^2 ±1	

Table 1.1: The generations of matter are organized by increasing mass (values are given at bottom-left corner for each flavor, in units of GeV/c^2) and decreasing electric charges: +2/3, -1/3 and 0, -1 (values are given at bottom-right corner for each flavor, in units of proton's charge)[1].

Quarks are confined in hadrons and cannot appear in isolation. Hadrons include mesons and baryons; they are the stable bound state configurations of quarks — a meson consists of a quark and

an anti-quark; a baryon consists of three quarks. Ordinary matter is made of electrons and two kinds of hadrons: protons (each a u-u-d quark triplet), and neutrons (each a u-d-d quark triplet). These are the first generation of matter particles. The heavier generations of particles only existed in the early stages of the universe. Today, they can be created in high energy accelerator collisions or in cosmic ray interactions. However, all but the proton, electron and neutrinos are unstable and quickly decay into the stable first generation particles.

Fundamental interactions

All physical phenomena are based on the four fundamental interactions: gravitation, the electromagnetic interaction, the strong interaction and the weak interaction. In the Standard Model, the interactions are communicated between particles by the exchange of intermediate vector bosons (see Table 1.1). These spin 1 particles are gluons in strong interactions, photons in electromagnetic interactions, and W^+, W^- and Z^0 bosons in weak interactions[2].

Among these basic interactions, electromagnetic interactions are experienced by particles that possess the properties of electric charge and/or magnetic moment; the strong interactions act between quarks to bind hadrons together; the weak interactions are primarily responsible for the decay interactions (massive hadrons and leptons decay into lighter hadrons and leptons, for instance). Each of these three interactions is associated with a charge: electric charge for the electromagnetic interaction, strong charge (color charge) for the strong interaction, and weak charge for the weak interaction. The interactions between particles occur only if the particles possess the corresponding charge. For example, quarks carry strong, electric and weak charge, but leptons only carry weak and electric charge. Thus, there is no strong interaction between quarks and leptons. The strengths of interactions can be characterized by their charges and appropriate coupling constants. A familiar example is the electromagnetic interaction that binds an electron and a proton to form a hydrogen atom: the Coulomb potential describing this interaction can be written as: $V(r) = -\frac{1}{4\pi\epsilon_0}\frac{e^2}{r}$, where $\pm e$ are the electric charges of the proton and electron, and $1/4\pi\epsilon_0$ is the coupling constant.

[2]Gravitation is not yet included in the Standard Model.

Beyond the Standard Model

There are many predictions that can be made through the theory of the Standard Model, and many of these predictions have been verified by experimental tests. For example, the Standard Model predicts that there exist the weak force carrier bosons — the W, Z bosons and some of the properties (like masses and decay modes) of these particles. Later on, all of these particles were observed and their predicted properties were confirmed by experiments [1].

Despite the fact that the Standard Model has had enormous success, there are many reasons that lead us to believe that the Standard Model is not a complete theory of fundamental particles and interactions; it does not predict and explain everything. For instance, it cannot predict particle masses (such as the mass of the top quark m_t) without experimental data; a large number of parameters need to be measured and inserted into the theory, and so on. In order to illustrate what some of the Standard Model's flaws and limitations are, let us consider a concrete experimental example: neutrino oscillation, which was observed and published by the Super-Kamiokande Collaboration in 1998 [2][3]. This is the first experimental deviation from the Standard Model. Neutrino oscillation refers to the evidence that the three types of neutrinos, ν_e,ν_μ and ν_τ, are actually linear combinations of several mass eigenstates ν_1, ν_2 and ν_3 that travel in space with slightly different frequencies due to their mass differences[4]. As a result, an initial pure neutrino beam, e.g. ν_μ, will subsequently contain admixtures of all three neutrino types after propagating through space. The neutrinos can oscillate if and only if they have masses. However, in the Standard Model, neutrinos are massless; they cannot oscillate. Therefore, the observation of neutrino oscillations implied that the Standard Model needed to be revised to accommodate this experimental fact.

To discover a more complete theory beyond the Standard Model, we need to measure the unknown parameters, test its predictions, look for new phenomena not predicted in the current model, and so on. The only way to settle these questions is through experiments; the Q^p_{Weak} experiment at

[3]The Super-Kamiokande Collaboration provided evidence that two-flavor neutrinos ($\nu_\mu \leftrightarrow \nu_\tau$) oscillate with $\sin^2 2\theta > 0.82$ and $5 \times 10^{-4} < \Delta m^2 < 6 \times 10^{-3}$ eV^2 at 90% confidence level.

[4]The wave function for a propagating neutrino in free space is given by $\psi(\mathbf{r}, t) = \psi_0 e^{-i(Et - \mathbf{p}\cdot\mathbf{r})/\hbar}$, where $E = \sqrt{p^2 + m^2}$ is the total energy; $\mathbf{p}$ is the momentum, $\hbar = h/2\pi$ (h is the Planck's constant). The mass m thus influences the oscillation frequency.

Jefferson Laboratory will be one such important experimental test.

1.1.2 Electroweak Interaction

As a logical extension of the work of Maxwell, who revealed the electric and magnetic forces as being different aspects of a single electromagnetic interaction, the Standard Model revealed the electromagnetic and weak interactions as being different aspects of a single electroweak interaction. The 1979 Nobel prize in physics was awarded to Sheldon Glashow, Steven Weinberg, and Abdus Salam for their development of the electroweak theory [3].

The electroweak theory has united electromagnetic interactions and weak interactions into one unified electroweak interaction; the electromagnetic interactions proceed by the exchange of photons, γ, and the weak interactions proceed by the exchange of massive vector bosons, $W^{\pm}$ and Z^0. The weak interactions are seen much less frequently than the electromagnetic interaction because the interaction rates depend on the mass of the exchanged particle — the $W^{\pm}$ and Z^0 bosons are very heavy, and this mass effect makes the interaction at low energies weak and short range.

By analogy to electromagnetism, where it is recognized that the electric fields and magnetic fields are treated as components of a single field tensor with six components that transform into one another under Lorentz transformations, the electroweak unification treats four interaction fields, each mediated by a massless gauge boson (a postulated triplet bosons, $W^i_\mu, i = 1, 2, 3$, and a neutral singlet boson, B_μ)[5], as different components of a single multicomponent quantum field. These bosons are related by rotations in an abstract space; these rotations transform the different field components into one another. The field equations are symmetric (fundamentally characterized by the $SU(2) \times U(1)$ gauge group) with respect to these rotations, and consequently we would expect all these bosons have the same mass (zero). However, due to the feature of spontaneous symmetry breaking, the solutions of the field equations have less symmetry than the equations themselves. The symmetry breaking mechanism (the Higgs mechanism) endows the massless gauge bosons with large rest mass, and separates the interaction into the electromagnetic sector and the weak

[5]Here the notations follow the convention in reference [1].

sector. This spontaneous breakdown of symmetry results from the energy difference between the initial high energy symmetric configuration and the final low energy asymmetric configuration—the initial symmetric configuration with equal (zero) masses for the gauge bosons is unstable, whereas the final asymmetric configuration with unequal masses is stable; the fields then spontaneously settle into the asymmetric configuration, with large masses for the $W^{\pm}$ and Z^0 bosons and zero mass for the photon. Thus, the electroweak theory reveals the hidden relationship between the massless photon and the massive $W^{\pm}$ and Z^0 bosons.

In this unified theory, the photon γ, the $W^{\pm}$ and Z^0 bosons are the observable consequence of the hypothetical zero-mass four-component field. The proposed existence of one heavy, spin-0 Higgs boson causes a mixing of the two electrically neutral components of the field (W^3_μ and B_μ) into the massless photon and massive Z^0, and gives mass to the charged components (W^1_μ and W^2_μ). The mixing is a rotation expressed as linear combination of W^i_μ and B_μ [4]:

$$|W^{\pm}> = (|W^1_\mu > \mp i|W^2_\mu >)/\sqrt{2}, \tag{1.1}$$

$$|\gamma> = \cos\theta_W|B_\mu > + \sin\theta_W|W^3_\mu >, \tag{1.2}$$

$$|Z^0> = -\sin\theta_W|B_\mu > + \cos\theta_W|W^3_\mu > . \tag{1.3}$$

The rotation is parameterized by an angle θ_W called the electroweak mixing angle or Weinberg angle (in practice the quantity $\sin^2\theta_W$ is far more frequently used), which is defined as [5]:

$$\sin^2\theta_W = 1 - \frac{M_W^2}{M_Z^2}, \qquad \cos\theta_W = \frac{M_W}{M_Z}, \tag{1.4}$$

where M_W and M_Z, are the W and Z^0 masses, respectively.

The weak mixing angle θ_W is the central parameter of electroweak theory. It also describes the relative strengths of the electromagnetic and weak interactions [5]:

$$\sin\theta_W = \frac{e}{g} = \frac{g'}{\sqrt{g^2+g'^2}}, \qquad \cos\theta_W = \frac{e}{g'} = \frac{g}{\sqrt{g^2+g'^2}}, \qquad \tan\theta_W = \frac{g'}{g}, \tag{1.5}$$

where the weak couplings for W_μ and B_μ are denoted by the weak charges g and g'; the electromagnetic coupling is denoted by the electric charge e.

The electroweak mixing angle plays a role in defining a particle's weak charge. For the proton, the relation between the electroweak mixing angle and the weak charge is given to the lowest order in perturbation theory by [6][7]:

$$Q_W^p = 1 - 4\sin^2\theta_W. \tag{1.6}$$

The numerical value of weak mixing angle $\sin^2\theta_W$ is about 0.23. This implies that the weak charge of the proton is almost zero, although its electromagnetic charge is one (in units of e). In contrast to the proton, the neutron's weak charge is 1, but its electromagnetic charge is 0. Therefore, for a heavy atom $A(Z, N)$, the weak charge is determined by [1]:

$$Q_W \simeq Z(1 - 4\sin^2\theta_W) - N, \tag{1.7}$$

where Z is the atomic number, A is the mass number and $A = Z + N$.

1.1.3 Parity Violating Electron-Proton Scattering

Handedness and the parity transformation

A coordinate system (x, y, z) is called a "right-handed" system (RHS) if $\hat{x} \times \hat{y} = \hat{z}$; a coordinate system (x', y', z') is called a "left-handed" system (LHS) if $\hat{x'} \times \hat{y'} = -\hat{z'}$. The parity operation ($\pi$) causes a RHS to transform into a LHS, i.e., it consists of a simultaneous reflection of all space coordinates through the origin: $\mathbf{r} \rightarrow -\mathbf{r}$. The parity operation is equivalent to a reflection plus a 180° rotation transformation. If the rotational invariance of observable properties is assumed, the parity transformation is indeed equivalent to a mirror reflection.

In particle physics, particles may also be classified as either "right-handed" or "left-handed" according to their helicity, which is defined as the expectation value of the intrinsic angular momentum

projected onto the direction of motion:

$$h = \frac{\mathbf{s} \cdot \mathbf{p}}{|s||p|} \,. \tag{1.8}$$

A particle with positive helicity ($h > 0$, spin pointing in its direction of motion) is said to be "right-handed"; a particle with negative helicity ($h < 0$, spin pointing in the opposite direction) is "left-handed". For massive fermion particles, the helicity can be prepared in an arbitrary state varying from $h = -1$ to $h = +1$, so they can either be right-handed or left-handed; for the weak interaction field particles ($W^{\pm}$ and Z^0 bosons), by contrast, the helicity can only be -1, thus they are left-handed only. This feature is built into the Standard Model description of weak interactions, and it gives rise to parity violation in a variety of processes, as described below.

For an experimental system of interacting particles, a parity operation refers to replacing that system with its mirror image. This spatial inversion operation can be done through changing left-handed particles to right-handed ones — simply speaking, we reverse the spin direction of the interacting particles with respect to their direction of motion. To illustrate, consider an electron and its mirror image (see Fig. 1.1): the electron travels toward a mirror and its spin is in the direction of its motion, so it is right-handed (helicity = +1); the image electron has the same spin direction and reversed direction of motion with respect to the object electron's, so the image electron is left-handed (helicity = -1). To obtain the mirror image, i.e., to perform a parity operation on the electron, we simply need to flip the electron's spin.

Parity violation

Parity conservation means that there are no physical consequences of a parity operation, i.e., the mirror-reflected physical system obeys the same physical laws as the original system. Otherwise, parity violation occurs. For a system of interacting particles, we can measure the rate for a particle interaction and compare with the mirror image of that interaction. If the rates are different from each other, then parity violation has taken place.

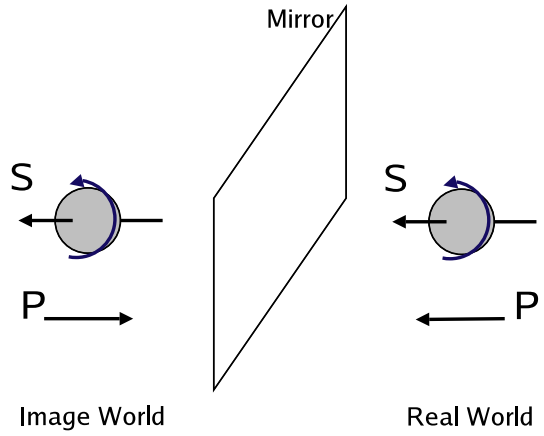

Figure 1.1: A right-handed electron and its left-handed mirror image.

Electromagnetic and strong interactions are independent of handedness, since they have the same strength for left-handed and right-handed particles. Hence, the processes involving these interactions are parity-conserving. The weak interaction is asymmetric for right-handed and left-handed particles because the force carrier particles $W^{\pm}$ and Z^0 are always left-handed. This built-in feature of the weak force carriers makes the weak interaction handedness-dependent, and thus any process involving the weak interaction is a parity-violating process.

The first experimental demonstration of parity violation in weak interactions was carried out by C. S. Wu et al. in 1956, through studying the β decay of ^{60}Co [8]. This experiment employed a low temperature (0.01 K) and a strong magnetic field to align the spin of ^{60}Co (J=5) nuclei; the relative electron intensities along and against the field direction were measured; then the mirror image of the decay process was achieved by reversing the magnetic field direction to flip the spin of ^{60}Co. The results showed that the β counting rate reversed as the magnetic field direction was reversed; the electrons "prefer" to be emitted opposite to the nuclear spin, i.e., the rate in the mirror system is different from the original rate, and thus parity is violated.

Parity violation exists in a typical particle scattering process due to the weak interaction. The scattering process itself is a powerful tool in the investigation of a particle's structure and properties. Therefore, the combination of the two, i.e., parity-violating scattering is an important method for

exploring weak-interaction-related phenomena.

Electron scattering formalism

The kinematics of an electron with momentum $\mathbf{p_0}$ scattering from a stationary proton with mass M determines the outgoing electron's momentum $\mathbf{p'}$ at scattering angle θ (see Fig. 1.2). Conserving

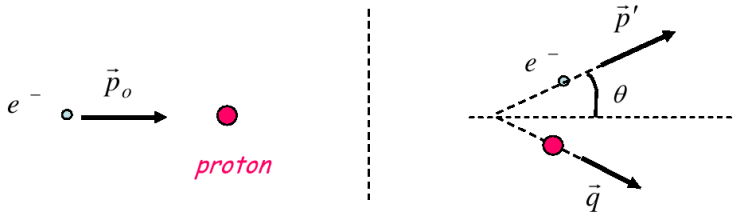

Figure 1.2: Electron-proton scattering process

energy and momentum for the process of elastic scattering with relativistic electrons, we find:

$$p' = \frac{p_0}{1 + \frac{p_0}{M}(1 - \cos\theta)}. \tag{1.9}$$

For relativistic electrons, their total energies $E' \simeq p'$ and $E_0 \simeq p_0$. Defining the 4-momentum transfer Q between the incoming and outgoing electrons as $Q \equiv \left[(\mathbf{p_0} - \mathbf{p'}), i(E_0 - E')\right]$, we have:

$$Q^2 = (\mathbf{p_0} - \mathbf{p'})^2 - (E_0 - E')^2 \simeq 2E_0E'(1 - \cos\theta). \tag{1.10}$$

The cross-section for the elastic scattering of relativistic electrons from protons[6] is given by the well known Rosenbluth Formula [9]:

$$\frac{d\sigma}{d\Omega} = \left(\frac{d\sigma}{d\Omega}\right)_{Mott}\left[\left(\frac{G_E^2 + \tau G_M^2}{1 + \tau}\right) + 2\tau G_M^2 \tan^2\frac{\theta}{2}\right] \qquad \text{with} \quad \tau = \frac{Q^2}{4M^2}\,, \tag{1.11}$$

[6]We account only for one photon exchange in the process described here.

where

$$\left.\frac{d\sigma}{d\Omega}\right|_{Mott} = \frac{(\hbar c\alpha)^2}{4E_0^2\sin^4(\theta/2)}\left(\frac{E'}{E_0}\right)\cos^2(\theta/2) = \frac{(\hbar c\alpha)^2\cos^2(\theta/2)}{4E_0^2\sin^4(\theta/2)[1+2\frac{E_0}{M}\sin^2(\theta/2)]} \tag{1.12}$$

(α is the fine-structure constant).

The differential cross-section $\left.\frac{d\sigma}{d\Omega}\right|_{Mott}$ describes the cross-section for electrons scattering from a point-like spin-0 target. The form factors G_E and G_M are functions of momentum transfer and can be well determined by experiment [10]. They describe the distributions of electric charge and magnetic moment inside the proton, i.e., they provide a description of the proton's electromagnetic structure. In the case $Q^2 \rightarrow 0$ (point-like limit), G_E is equal to the normalized electric charge and G_M coincides with the magnetic moment. The differential cross-section $\frac{d\sigma}{d\Omega}$ depends on the fourth power of the electric charge since it is proportional to α^2, and the electromagnetic coupling constant α is proportional to e^2. The form factors G_E and G_M determined from "ordinary" (parity-conserving) electron scattering should really be denoted as G_E^γ and G_M^γ to emphasize that they are electromagnetic structure functions probed by the electromagnetic field particle γ, the photon.

In the Q_{Weak} experiment, we want to determine the proton's weak charge to infer the weak mixing angle, which can be isolated via parity-violating electron scattering. In the scattering process, parity violation arises through the interference between the weak neutral-current (Z^0 exchange) and the purely electromagnetic contributions to the transition amplitude, i.e., there is an interference term between parity-conserving (PC) and parity-violating (PV) amplitudes due to γ and Z^0 exchange. The interference then can be isolated by measuring the PV cross-section asymmetry for elastic scattering:

$$A_{PV} = \frac{(\frac{d\sigma}{d\Omega})_+ - (\frac{d\sigma}{d\Omega})_-}{(\frac{d\sigma}{d\Omega})_+ + (\frac{d\sigma}{d\Omega})_-}\,, \tag{1.13}$$

where "+" and "−" refer to the electron beam helicity. This in turn can be expressed, by analogy to equation 1.11 as [11]:

$$A_{PV} = \left[\frac{-G_F Q^2}{4\pi\alpha\sqrt{2}}\right]\left[\frac{\epsilon G_E^\gamma G_E^Z + \tau G_M^\gamma G_M^Z - (1-4\sin^2\theta_W)\epsilon' G_M^\gamma G_A^Z}{\epsilon(G_E^\gamma)^2 + \tau(G_M^\gamma)^2}\right], \tag{1.14}$$

where

$$\epsilon = \frac{1}{1 + 2(1+\tau)\tan^2(\theta/2)}, \qquad \epsilon' = \sqrt{\tau(1+\tau)(1-\epsilon^2)}, \tag{1.15}$$

and G_F is the Fermi constant.

The form factors $G_E^Z(Q^2)$ and $G_M^Z(Q^2)$ are introduced here to describe the electric and magnetic structure as probed by the Z boson. The $Q^2 \to 0$ limit of $G_E^Z(Q^2)$ gives the proton's weak charge. It has been shown that for forward-angle scattering where $\theta \to 0$, $\epsilon \to 1$ and $\tau << 1$, the asymmetry can be written as [6][11]:

$$A_{PV} = \frac{-G_F}{4\pi\alpha\sqrt{2}}[Q^2 Q_W^p + F^p(Q^2,\theta)] \xrightarrow{Q^2\to 0,\theta\to 0} \frac{-G_F}{4\pi\alpha\sqrt{2}}[Q^2 Q_W^p + Q^4 B(Q^2)]\,, \tag{1.16}$$

where F^p and $B(Q^2)$ are hadronic form factors, and Q_W^p is the proton's weak charge.

Note that the asymmetry A_{PV} is proportional to $Q^2 Q_W^p$ at low Q^2. Neglecting radiative corrections (to be discussed in the following section), the leading term in the equation is simply $Q_W^p = 1 - 4\sin^2\theta_W$. $B(Q^2)$ is a hadronic form factor term that contains the form factors G_E^γ, G_M^γ and G_E^Z, G_M^Z. Thus, if the parity-violating asymmetry A_{PV} is measured very precisely, and the hadronic form factors are extrapolated from other experimental results, the proton's weak charge and hence the weak mixing angle can be determined. The nucleon structure contributions contained in $B(Q^2)$ can be reduced by measuring A_{PV} at low momentum transfer, since $B(Q^2)$ enters to order Q^4, and Q_W^p enters to order Q^2. However, a side-effect of lowering the momentum transfer is that it also reduces the sensitivity to Q_W^p. A number of experiments [12] studying parity-violation at forward angles at higher momentum transfer can be used to determine and correct the value of $B(Q^2)$ and to optimize the value of momentum transfer Q^2 for the Q_{Weak}^p experiment.

1.1.4 Running of the Electroweak Mixing Angle

When a particle interacts with various fields, the effective values of its physical properties, such as mass, charge, and so on, may change. These changes arise due to radiative corrections in quantum

field theory. In QED, for example, an electron interacts with other charged particles via exchanging virtual photons. The virtual photons form a photon cloud around the electron since they are continually emitted and reabsorbed. They can also temporarily transform into virtual electron-positron pairs that will be polarized by the parent electron (the so-called "vacuum polarization" effect); the vacuum polarization will then produce a shielding effect on the parent electron's charge. The shielding effect is probed to a different extent at different energy scales, and thus leads to an energy dependent interaction strength.

Radiative corrections in the Standard Model are responsible for changing the effective QED coupling $\alpha(\mu^2)$ and QCD coupling $\alpha_s(\mu^2)$) with energy scale μ, which can be predicted to high precision using current perturbation theory techniques. This "running of couplings" for the weak interaction causes the effective weak mixing angle to change slowly as a function of μ^2 ($\mu^2 \sim Q^2$). This phenomenon is known as the "running of the weak mixing angle", which is a key prediction that can be made through the electroweak theory of the Standard Model[6][7].

The curve in Fig. 1.3 shows the variation of the weak mixing angle with momentum transfer Q, which is calculated using the modified minimal subtraction scheme[1][6]. The precise measurements in electron-positron colliding beam experiments at the Z^0 pole [7] determine the overall magnitude of the curve. The turning point of the curve corresponds to the momentum transfer $Q = M_W$.

If the running of $\sin^2\theta_W$ can be precisely tested by experiment, the electroweak theory of the Standard Model then can be checked rigorously. Any deviation between the prediction and experimental value will indicate possible "new physics" that is not included in the current model and perturbation theory running calculations.

To test the running of the weak mixing angle, one can conduct measurements of some observables, which are sensitive to the weak mixing angle, to extract the value of $\sin^2\theta_W$ at various energy scales. However, to date, the existing world data have not precisely confirmed this running feature of $\sin^2\theta_W$, since those experiments have not obtained statistically significant deviations from the

[7] Energy scale of value $\sim$ 91.2 GeV, which corresponds to the Z^0 boson resonance in the e^+e^- collision.

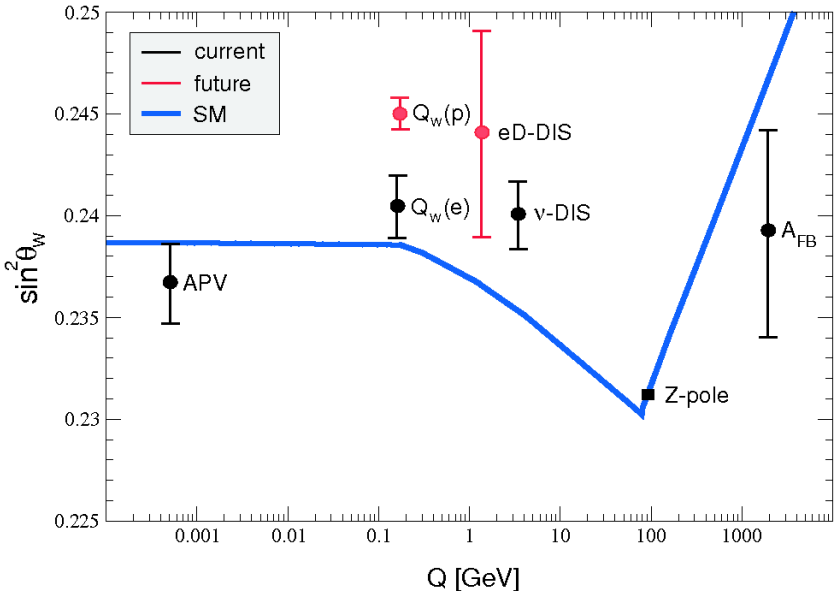

Figure 1.3: The running of weak mixing angle $\sin^2\theta_W$

prediction at low momentum transfer. This situation is shown in Fig. 1.3 using the black error bars for existing results (the proposed future measurements are indicated by the red error bars).

As is seen from Fig. 1.3, the measurements performed at LEP (the Large Electron-Positron Collider that was built at CERN) and SLC (the Stanford Linear Collider) near the Z^0 pole are very precise, which are used to set the overall magnitude of the running of $\sin^2\theta_W$ curve. The other three off-peak measurements, APV (atomic parity violation), Q_W(e) (SLAC E-158) and ν-DIS (NuTeV, deep inelastic neutrino-nucleus scattering), test the "running" at different momentum transfers with roughly the same uncertainties on the extracted value of $\sin^2\theta_W$.

The APV experiment [13] measured the weak charge of the Cesium nucleus ($Q_W(Cs)$) by exploiting parity-violating effects in atomic Cesium, then extracting the weak mixing angle at very low Q^2. However, the reliability of the result for $\sin^2\theta_W$ is subject to theoretical atomic structure uncertainties.

The NuTeV experiment [14] at Fermilab infers the value of $\sin^2\theta_W$ at $Q \sim 3$ GeV through the deep inelastic scattering of neutrinos from a BeO target. The result has a slightly greater precision

than the one from atomic parity violation, but the contributions and uncertainties from the radiative corrections, and possible isospin symmetry violation can not be clearly interpreted yet [15].

The E158 experiment at SLAC [22], which measured the weak charge of the electron (Q_W^e), is a parity violating Møller scattering (electron-electron) experiment at low Q^2. The extracted value of $\sin^2\theta_W$ within its statistical and systematic accuracy is consistent with the Standard Model expectation. Because this is a pure leptonic measurement, it has a very clean interpretation. However, the experimental uncertainty is still too large to signal new physics or put significant constraints on the current model.

The current situation of $\sin^2\theta_W$ measurements motivates the preparation of new experiments. The Q^p_{Weak} collaboration at Thomas Jefferson National Accelerator Facility (Jefferson Lab) is developing an experiment which will precisely measure the parity violating asymmetry in elastic electron-proton scattering to infer the proton's weak charge and hence the weak mixing angle[16]. As a fundamental property, the proton's weak charge has never been directly measured. The Q^p_{Weak} experiment will provide the first precision measurement of the proton's weak charge.

To lowest order in perturbation theory, protons and electrons have equal and opposite weak charges: $Q_W^{p,e} = \pm(1 - 4\sin^2\theta_W)$. This implies, for the extraction of $\sin^2\theta_W$ from the weak charge measurements, that the uncertainty:

$$\Delta(\sin^2\theta_W) = \frac{1}{4}\Delta Q_W^{p,e} = \frac{1}{4}\Big(\frac{\Delta Q_W^{p,e}}{Q_W^{p,e}}\Big)Q_W^{p,e} = \frac{1}{4}\Big(\frac{\Delta Q_W^{p,e}}{Q_W^{p,e}}\Big)(1 - 4\sin^2\theta_W). \tag{1.17}$$

The value of the weak mixing angle, $\sin^2\theta_W$, is numerically close to 0.23. This implies that $\Delta(\sin^2\theta_W)/\sin^2\theta_W \simeq 0.087(\Delta Q_W/Q_W)$. Consequently, the factor 1/4 makes a weak charge measurement on the proton or electron particularly sensitive to deviations arising from new physics[8]. In contrast, the APV experiment measures $Q_W(Z,N)$ for a heavy atom; due to the dominant neutron contributions to the atom's weak charge, the observable Q_W^p is suppressed; the required experimental precision for the APV is about an order of magnitude larger than needed for directly measuring

[8]It should be noted, however, that there are different radiative corrections to Q_W^p and Q_W^e. As a result, the measured values are quite different at low Q^2 ($Q_W^p = 0.0716$ and $Q_W^e = -0.0449$) [6][7].

the weak charge of proton or electron to extract $\sin^2\theta_W$ to comparable accuracy. Moreover, the theoretical uncertainties in the interpretation of parity violating elastic scattering at low Q^2 are extremely small, which makes the parity violating elastic scattering asymmetry interpretable as a new physics probe.

Comparing with the SLAC E-158 "e-e" scattering experiment, the proposed Q^p_{Weak} "e-p" scattering experiment will be performed at similar momentum transfer ($Q^2 \simeq 0.03$ (GeV)^2), but with higher precision, and significantly smaller statistical and systematic errors. The Q^p_{Weak} experiment aims to reach a 4% measurement of Q^p_W, which corresponds to an uncertainty of ~ 0.0008 in $\sin^2\theta_W$ ($\Delta(\sin^2\theta_W)/\sin^2\theta_W \sim 0.35\%$); the E-158 experiment has a combined statistical and systematic error of $\sim 9\%$, which corresponds to an uncertainty of ~ 0.0018 in $\sin^2\theta_W$ ($\Delta(\sin^2\theta_W)/\sin^2\theta_W \sim 0.79\%$) [23].

1.2 Experiment Overview

1.2.1 Basic Requirements

The Q^p_{Weak} experiment will extract the proton's weak charge from a precision measurement of the parity violating asymmetry A_{PV} in elastic e-p scattering. Neglecting the contribution of the hadronic structure function $B(Q^2)$, the expected asymmetry can be estimated according to equation 1.16 as:

$$A_{PV} \sim \left[\frac{-G_F}{4\pi\alpha\sqrt{2}}\right] Q^2 Q^p_W \sim -2\times 10^{-7}\,, \tag{1.18}$$

where $G_F = 1.17\times 10^{-5}$ GeV^{-2}, $\alpha^{-1} = 137$, $Q^2 = 0.03$ GeV^2, $Q^p_W = 1 - 4\sin^2\theta_W \sim 0.08$.

In order to determine Q^p_W to the uncertainty of $\pm 4\%$, the uncertainty of asymmetry (ΔA_{PV}) should be no greater than 1×10^{-8}. There are many sources that can lead to a significant false asymmetry, since A_{PV} is only approximately -0.2 ppm[9]. Therefore, the e-p scattering experiment has to be carried out to a high statistical precision to meet these challenges, which in turn requires:

[9] Another important term entering the asymmetry equation 1.16 is the hadronic structure function $B(Q^2)$, which depends on the results of other experiments. In fact, $B(Q^2)$ contributes -1×10^{-7} to the asymmetry; hence, $A_{PV} \sim -0.3$ ppm, as discussed in section 1.2.3.

- a highly polarized, high current electron beam, whose polarization can be measured to high accuracy[10];
- a reliable, long liquid hydrogen target, which should have minimal density fluctuations while being operated at high beam current;
- a high quality magnetic spectrometer, whose focusing properties can cleanly separate the elastic and inelastic events; this also should be highly symmetric to reduce systematic error sensitivities.
- a low noise, stable integrating detector system with large solid angle acceptance and uniform response, which can measure the high rate of elastically scattered electrons in a high radiation environment.

Equation 1.16 shows that the asymmetry at $Q^2 \to 0$ is proportional to Q^2, and so any measured Q^2 errors will apply to the interpretation of A_{PV}. Therefore, a good Q^2 determination is critical for the asymmetry measurement. From equations 1.9 and 1.10, we see that the value of Q^2 can be determined by measuring the energy of incident electrons (or the momentum of scattered electrons) and the corresponding scattering angles. In the experiment, the elastically scattered electrons will be distributed across the main detectors' acceptance, including also some inelastic events which arise from the target, the detector wall and the general background in the experimental hall. In practice, the Q^2 for the elastic events needs to be measured, averaged over the detector acceptance and weighted by the detectors response to obtain the averages $< Q^2 >$ and $< Q^4 >$ for interpretation of A_{PV}. This requires:

- finding the scattering vertex to determine the radiation energy loss of the incident electron;
- measuring the beam energy, determining the scattering angle and the momentum of the elastically scattered electrons;

[10]Note that the experimental asymmetry is PA_{PV}; thus, it is important to understand the role of polarization.

- providing accurate measurements of the elastic electron and the inelastic electron contributions to the detector signal;
- suppressing background contributions.

To accomplish the $< Q^2 >$ and $< Q^4 >$ determination, a set of high accuracy tracking detectors and apparatus should be employed in the experimental setup. However, due to the statistical error requirement for measuring A_{PV}, the rate in the main experiment will be very high (about 1 MHz/cm^2 at the main detectors at the planned beam current of 180 μA). The tracking detectors cannot respond properly at such a rate. A way to solve this problem is to do the tracking measurements using low beam current ($\leq$ 10 nA calibration mode), then extrapolate the results to the high beam current operation (180 μA production mode).

1.2.2 Experimental Setup

The Q^p_{Weak} experiment will be prepared according to the requirements discussed in the previous section. The overall layout of the experiment is shown schematically in Fig. 1.4. The key elements of the experimental apparatus include a longitudinally polarized electron beam, a liquid hydrogen target, a room temperature 8-fold symmetric toroidal magnetic spectrometer, 8 Čerenkov detectors for the scattered electrons at forward angles, and a set of tracking devices. The experiment has two operating modes: one is the low-current calibration mode for the Q^2 acceptance mapping; the other is the high-current production mode for the asymmetry determination. In the production mode, the tracking detectors will not be used.

In the experiment, the $\sim$ 85% longitudinally polarized electron beam is incident on a 35 cm liquid hydrogen target. The $\sim 8^o$ forward scattered electrons are selected by a double collimator and then pass through the toroidal magnetic field of the magnetic spectrometer that has a field integral of about 0.67 T·m along the envelope of the elastic electron trajectories. This magnetic field deflects the elastic electrons by about 10^o and provides a clean separation between the elastically scattered electrons and inelastically scattered electrons. The elastic electrons are focused onto a set of eight,

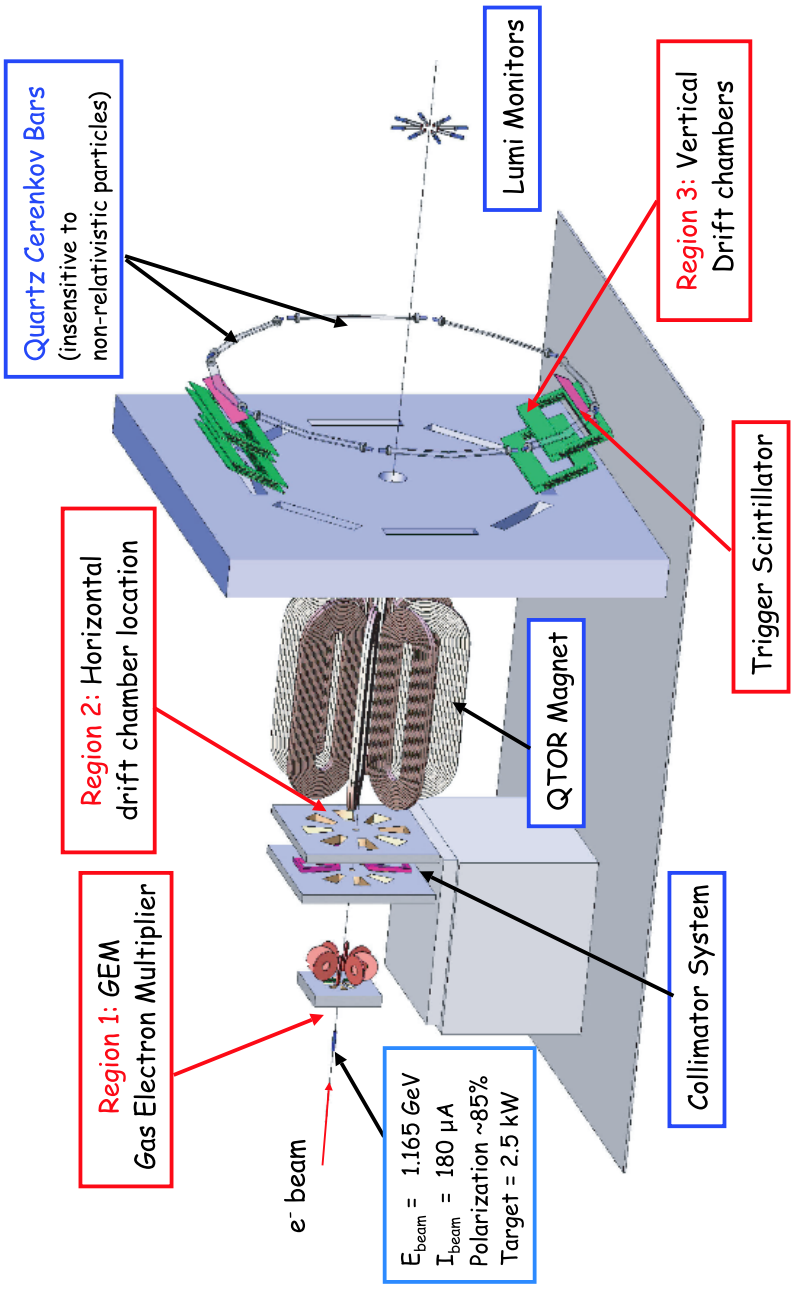

Figure 1.4: The Q^p_{Weak} experimental apparatus. The scattered electrons are selected by a double collimator system and are deflected by the QTOR magnet to the quartz Čerenkov detector bars. A small red mini-torus is shown downstream of the first collimator, originally planned to sweep low energy electrons out of the path of the region 2 tracking chambers, but it will not be used for the Qweak measurements. The tracking detectors will not be used during high current running to measure the parity violating asymmetry.

200 cm × 18 cm rectangular quartz bars and produce Čerenkov light in the bars. The Čerenkov photons are detected by photo-multiplier tubes (PMTs). The Čerenkov signal is read out either in current mode to achieve the high statistical precision required for the asymmetry measurements or in counting mode for the accurate Q^2 mapping. The inelastically scattered electrons are bent out of the detector acceptance by the spectrometer, so they only make a tiny contribution to the Čerenkov signal. A typical distribution of elastic events at a Čerenkov detector is shown in Fig.1.5.

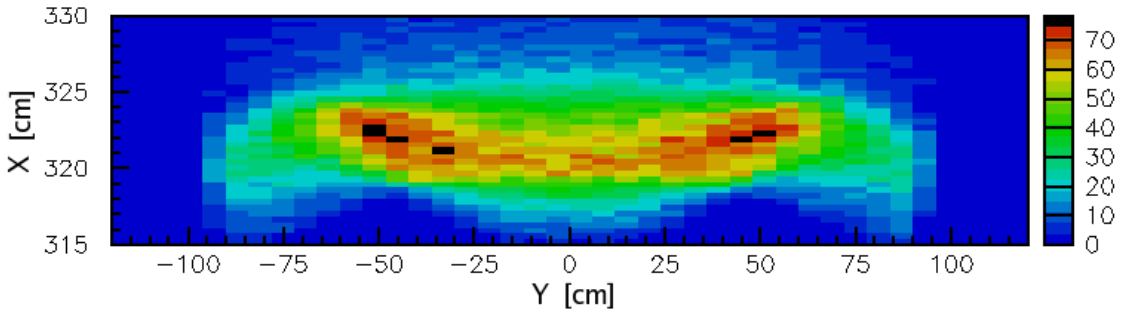

Figure 1.5: A simulated distribution of elastic events at a Čerenkov detector (courtesy J. Birchall, used with permission). The center of the target is 650 cm upstream from the center of the magnetic spectrometer, and the detector bar is on the focal plane located 570 cm downstream from the center of the magnetic spectrometer. The X-coordinates (indicating the distance to the beam axis) are across the detector bar, and the Y-coordinates are along the detector bar. Note also that the X and Y scales are not the same; the X direction corresponds to the scattering angle θ, while the Y direction corresponds to the azimuthal angle ϕ. The scales at the right show the event rate (in arbitrary units).

The tracking system can precisely determine the 4-momentum transfer Q^2 and the contribution of inelastic scattering events to the Čerenkov detector signal. The system includes three regions of tracking chambers, a focal plane electron flux scanner (not shown in Fig. 1.4), trigger scintillators and associated shielding.

The Region-I tracking chamber is a gas electron multiplier (GEM) used to locate the scattering vertex; the Region-II horizontal drift chambers (HDCs) combined with the Region-I GEM can determine the scattering angle of elastic electrons. The Region-III system has two vertical drift chambers (VDCs), which are used to measure the momentum of electrons, and define particle trajectories incident on the Čerenkov bars.

The focal plane electron flux scanner consists of a small active area quartz Čerenkov detector and a pair of air-core light guide pipes. The scanning Čerenkov signal is read out by PMTs in counting mode for all beam currents. It can map the light distribution of the main Čerenkov bars at both low beam current and high beam current so that the Q^2 mapping at low beam current can be extrapolated to high beam current with confidence. The trigger scintillators are mounted immediately downstream of the Region-III VDCs. This fast response system will provide the trigger and timing for other detectors.

The basic parameters of the experiment are presented in Table 1.2. A proposed 2200 hour production measurement for Q_W^p will be used to determine the proton's weak charge to $\sim 4\%$ combined statistical and systematic uncertainty. The experiment is now in the construction phase; the installation is expected to be carried out at Jefferson Lab in 2009.

Parameter	*Value*
Incident Beam Energy	1.165 GeV
Beam Polarization	85%
Beam Current	180 μA
Target Thickness	35 cm
Running Time	2200 hours
Nominal Scattering Angle	8.4$^{\mathrm{o}}$
Scattering Angle Acceptance	$\pm 3^{\mathrm{o}}$

Table 1.2: Basic parameters of the Q_{Weak}^p experiment

1.2.3 Experimental Sensitivity

The Q_{Weak}^p experiment has a complementary dependence on physics beyond the Standard Model compared to other existing and planned experiments to search for the running of $\sin^2\theta_W$. To reveal the physics behind the experimental data, it is necessary to analyze the source and magnitude of errors to find the clues that may reveal new physics. The uncertainties in the Q_{Weak}^p experiment are the combination of statistical and systematic uncertainties. Both types of uncertainties should be reduced to be as small as possible; in addition, the remaining systematic uncertainties should be

theoretically interpretable. Table 1.3 shows the anticipated experimental uncertainties [24] in the Q^p_{Weak} experiment.

Source	$\Delta A/A$	$\Delta Q^p_W/Q^p_W$
Statistical (2200 hours production)	1.8%	2.9%
Systematic:		
Hadronic structure corrections	–	2.2%
Beam polarization	1.0%	1.6%
Average Q^2 determination	0.7%	1.1%
Helicity-correlated beam properties	0.5%	0.8%
Background	0.5%	0.8%
Total systematic	2.3%	4.3%

Table 1.3: The anticipated experimental uncertainties in the Q^p_{Weak} experiment

The ultimate goal of the experiment is to determine Q^p_W with 4% combined statistical and systematic uncertainties. From equation 1.17, we know this uncertainty corresponds to $\sim 0.3\%$ precision on $\sin^2\theta_W$ at $Q^2 \sim 0.03$ (GeV)^2. In order to reach the proposed experimental goal, knowledge of the hadronic form factor $B(Q^2)$ correction must be acquired from other experiments. In equation 1.18, we estimated the value of the asymmetry as approximately -0.2 ppm. That estimation only considers the weak charge contribution to the asymmetry. If other contributions are accounted for, the asymmetry at $Q^2 = 0.03$ (GeV)^2 can be written as [25]:

$$A_{PV} = A_{Q^p_W} + A_{hadronic} + A_{axial}\,, \tag{1.19}$$

where $A_{Q^p_W} \sim -0.19$ ppm, $A_{hadronic} \sim -0.09$ ppm and $A_{axial} \sim -0.01$ ppm. The total asymmetry is expected to be approximately -0.3 ppm.

The nucleon structure (containing $G^\gamma_{E,M}$, $G^Z_{E,M}$) contributions to the asymmetry are about 31%, constrained by HAPPEX [26][27][28], G^0 [29] and MAMI PVA4 [30][31] experiments. The third term, the e-N axial-vector form factor (G^e_A) contribution, has large electroweak radiative corrections; its contribution to the asymmetry is about 4%. The quadrature sum of expected $\Delta A_{hadronic}/A$ ($\sim$ 1.5%) and $\Delta A_{axial}/A$ ($\sim$ 1.2%) uncertainties contribute 1.9% to the uncertainty of Q^p_W.

The hadronic corrections enter at order Q^4 in the parity-violating asymmetry, whereas the value of Q_W^p enters the order Q^2. Decreasing the value of Q^2 can reduce the uncertainties on Q_W^p. However, the sensitivity for Q_W^p would also be suppressed at the same time. The optimized value for Q^2 is about 0.03 $(\text{GeV})^2$. This small momentum transfer requires low beam energy ($\sim$ 1.165 GeV) and small scattering angle ($\sim 8^{\text{o}}$) for the elastic electrons.

Chapter 2

QTOR Magnet

The Q^p_{Weak} toroidal magnetic spectrometer (QTOR) plays a critically important role in the Q^p_{Weak} experiment. It is used to separate the elastically scattered electrons and inelastically scattered electrons and to focus the elastic electrons onto a set of quartz Čerenkov detector bars. This chapter introduces the magnetic field requirements of the Q^p_{Weak} experiment, the principle of the toroidal magnetic spectrometer, the QTOR design, and the manufactured magnet coils, as well the motivation of the magnetic field simulation and mapping effort.

2.1 The Toroidal Magnetic Spectrometer

For the parity-violating asymmetry (A_{PV}) measurement in the Q^p_{Weak} experiment, only the elastic electrons' contribution to the scattering cross section should be measured. The scattered electrons at a certain angle are a mixture of elastically and inelastically scattered electrons. The inelastic electrons must be bent out of the detectors' acceptance to avoid contamination of the elastic signal. This requires a spectrometer that can cleanly separate the elastic and inelastic channels. Due to the high statistical requirement of the Q^p_{Weak} experiment, the rates in the Čerenkov detectors must be very high. Thus, the acceptance of detectors should be as large as possible to detect as large a fraction of the elastic electrons as possible. This requires the spectrometer to have an open geometry to

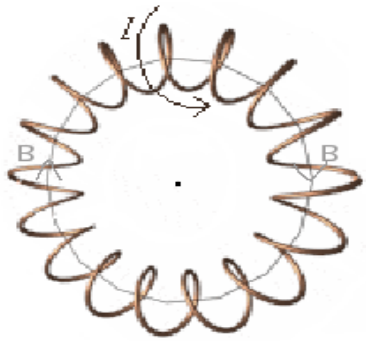

Figure 2.1: A typical toroidal magnet.

allow for maximum detector solid angle, and to have focusing properties so that a detector system of reasonable size can be mounted at the focal plane to measure the elastic asymmetry with negligible contamination from inelastic scattering and other background processes. In addition, axially symmetric acceptance in the experiment is very important because it reduces the sensitivity to a number of systematic error contributions. This requires that the spectrometer must be highly symmetric with respect to the beam line. When taking into account all of these requirements, a toroidal magnetic spectrometer appears to be the best choice.

An ideal toroidal magnet has a doughnut-shaped magnetic field flux geometry. This toroidal magnetic field is axially symmetric. Along the axis is a field free region. A charged particle traveling through the field will be deflected toward or away from the axis, depending on the charge of the particle and the direction of the magnetic field. A typical toroidal magnet is a solenoid that is looped back on itself to form a ring and wound with a wire carrying current I (see Fig. 2.1).

In the Q^p_{Weak} experiment, the toroidal magnetic spectrometer is refered to as "QTOR". In order to allow the scattered electrons to pass through the magnetic field without scattering from the magnet coils, i.e., to meet the open geometry requirement, the Q^p_{Weak} toroidal spectrometer field is produced by a set of eight identical field coils with $\Delta\phi = 45^{\circ}$ gaps between them (the layout is shown in Fig. 2.2). The resulting field is not that of an ideal toroid, but it does allow for the required focusing properties in an open geometry.

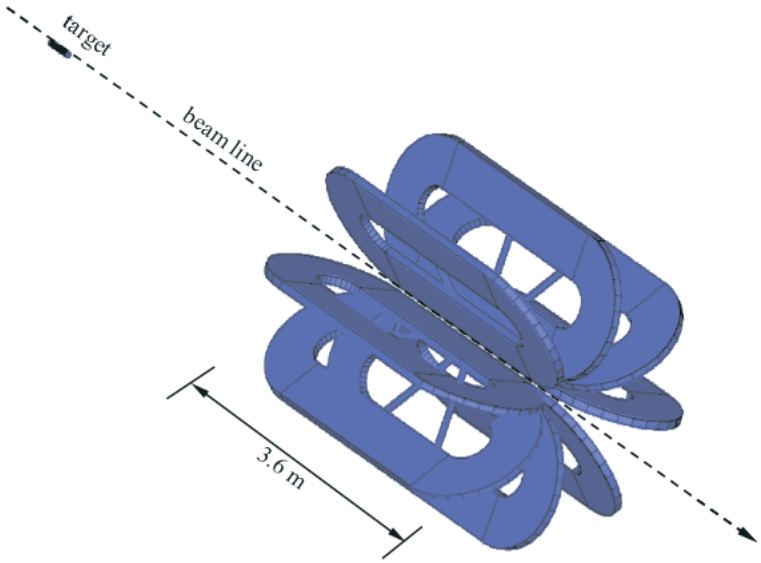

Figure 2.2: The layout of the Q^p_{Weak} toroidal magnetic spectrometer (QTOR) and its position relative to the target.

Prior to the commencement of this work, some preliminary studies for the QTOR had been made [16]. Basically, the optimized QTOR design is a resistive (normal temperature) toroidal magnet with an eight-fold symmetric structure. It has the following features:

- each of the eight coil packages has a simple racetrack shape;
- each coil package consists of two layers, called the “double pancake” structure;
- each pancake consists of two semicircular curved sections and two straight sections;
- each semicircular curved section has an inner radius 0.24 m and an outer radius 0.75 m;
- each straight section is 2.20 m long;
- the coil’s conductor is made of copper with a rectangular cross section (5.84 cm by 3.81 cm, or 2.3 in by 1.5 in);
- the copper conductor has a hole in the center (2.03 cm or 0.8 in in diameter) for water-cooling.

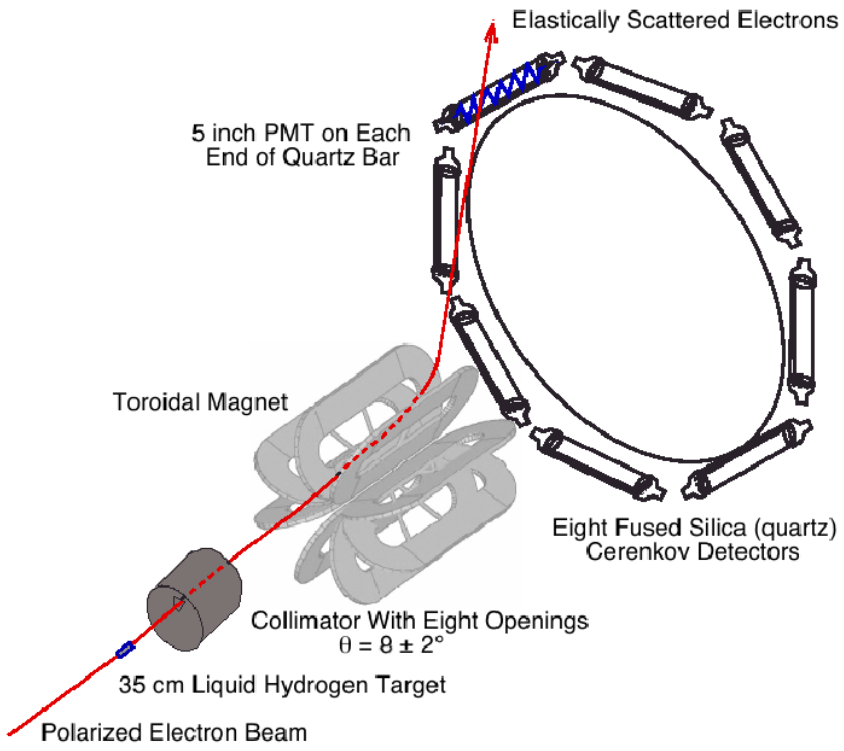

Figure 2.3: An electron's trajectory in the Q^p_{Weak} toroidal magnetic field.

The QTOR is an iron-free magnet (i.e., there is no magnetic material used). The coils are driven by a DC power supply with a maximum current of about 9 kA. This design is based on an existing resistive toroidal magnet BLAST [32] at MIT-Bates Laboratory[1]. The resistive magnet is preferred in the Q^p_{Weak} experiment mainly because of its simplicity and low cost relative to a superconducting one.

To explore the basic properties of the QTOR magnet, we start by considering the kinematics for electron-proton elastic scattering, which are given by equation 1.9. Neglecting the energy loss in the target, the momenta of elastically scattered electrons at $\theta_e = 8.0^o$ are $p' \simeq 1.151$ GeV (beam energy

[1]The William F. Bates Linear Accelerator Center at Massachusetts Institute of Technology (USA), the planned test site for the QTOR.

$E_0 = p_0 = 1.165$ GeV). In the magnetic field **B**, the electrons are deflected under the Lorentz force:

$$\mathbf{F} = -e\mathbf{v} \times \mathbf{B} = d\mathbf{p}/dt, \tag{2.1}$$

which leads to

$$d\mathbf{p} = -e(\mathbf{v}dt) \times \mathbf{B} = -e\, d\mathbf{l} \times \mathbf{B}. \tag{2.2}$$

Fig. 2.4 shows the relation between the momentum change and deflection angle when a moving electron experiences a magnetic field, from which we obtain:

$$d\theta = \frac{dp}{p} = \frac{e}{p} B_\perp\, dl, \tag{2.3}$$

where $B_\perp$ is the magnetic field component perpendicular to the electron's trajectory. Thus, the field integral can be expressed as:

$$\int B_\perp\, dl = \Delta\theta \frac{p}{e}. \tag{2.4}$$

The design of the Q^p_{Weak} experiment requires that the QTOR can bend the $\sim 8^o$ elastically scattered electrons by about 10^o (the electron's trajectory is sketched in Fig. 2.3). That in turn requires that the field integral along the paths of elastic electrons should reach 0.67 T·m (e.g., for $\Delta\theta = 10^o$, $p = 1.15$ GeV/c, the field integral has a value of approximately 0.67 T·m).

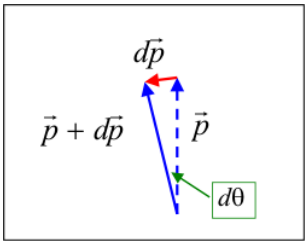

Figure 2.4: Deflection of electron in a magnetic field

The inelastic electrons have much smaller momentum at the same scattering angle as the elastic electrons. The kinematics for electron-proton inelastic scattering (refer to Fig. 1.2) are given by:

$$p' = \frac{p_0 - (M' - M) - \frac{(M'-M)^2}{2M}}{1 + \frac{p_0}{M}(1 - \cos\theta)} , \tag{2.5}$$

where M' is the mass of the proton's excited state. The Δ^+ resonance of the proton is at 1.232 GeV (294 MeV above the mass of the proton) with width $\sim$ 118 MeV. The momenta of these elastically scattered electrons at $\theta_e = 8.0^o$ can then be calculated as: $p' \simeq 0.815$ GeV. Using equation 2.4 and the values $\int B\, dl \simeq 0.67$ T·m, $p = 0.815$ GeV, we can estimate the deflection angle of the inelastic electrons as[2]: $\Delta\theta \simeq 14^o$. The inelastic electrons are deflected by about 14^o so that they are out of the acceptance of the main Čerenkov detectors. Thus, the difference of the deflection angles separates the elastic and inelastic channels at the detectors (refer to Fig. 2.6).

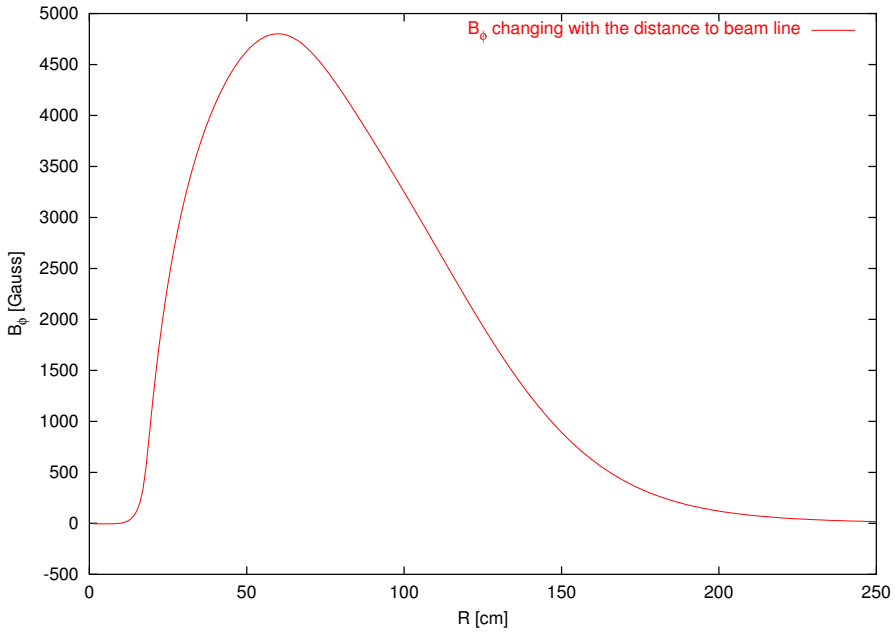

Figure 2.5: The azimuthal magnetic field components B_ϕ on a median plane between two coils as a function of distance (R) from test point to the beam line.

As the electrons cross the field region of QTOR, they experience a transverse magnetic field component, i.e., the azimuthal magnetic field component B_ϕ. B_ϕ changes radially from zero to a

[2]In fact, an inelastic electron experiences a weaker field and shorter path than an elastic electron, so its field integral is smaller than 0.67 T·m. Thus, the real deflection angle will be smaller than the estimated 14^o.

maximum value, then again to zero with increasing distance from the beam line to the test point (see Fig. 2.5). The decreasing slope of B_ϕ, i.e. $\partial B_\phi / \partial r$, provides the focusing property of QTOR. Focusing occurs because the elastic electrons with smaller target scattering angles (and larger momenta) are incident closer to the field peak than the elastic electrons with larger scattering angles (and smaller momenta); thus, the small angle scattered electrons experience larger field strength and larger field integral than the large angle scattered electrons[3]. As a result, the small angle scattered electrons are bent more by the field than the large angle scattered electrons, and their trajectories will cross (or get very close to each other) at a certain point (the focal point, refer to Fig. 2.6). Therefore, the QTOR acts like a magnetic convex lens, which focuses the elastic electrons onto the detectors at the focal plane.

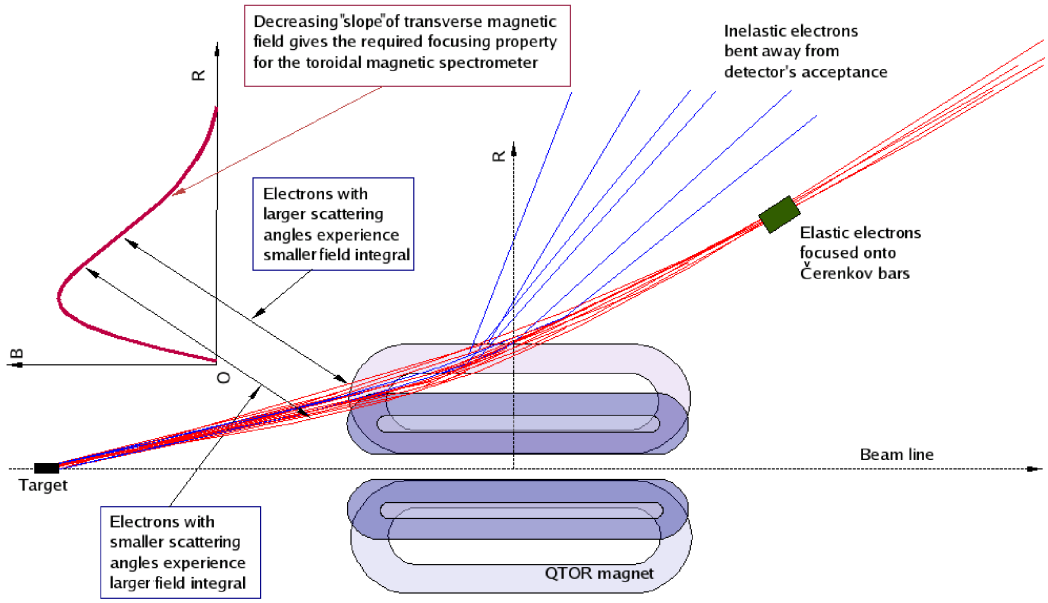

Figure 2.6: Electron separation and focusing

Since they are emitted within a finite range of scattering angles, instead of being focused exactly at a point, the elastically scattered electrons accepted by the collimator system will have a certain

[3] As indicated in equation 1.9, the scattered electron momenta also vary with scattering angle; however, this variation is small compared to the change in the field integral, and hence the focusing is essentially all due to the variation in field integral.

distribution within a small area at the focal plane. The distribution is also affected by the following distinct effects:

- the variation of electron energy loss in the target, which determines the width of the distribution along X (see Fig. 2.8),
- the azimuthal angle dependence of the toroidal magnetic field, which determines the shape of the distribution along Y (see Fig. 2.8),
- and the scattering angle dependence of the scattering cross section (i.e., $\frac{d\sigma}{d\Omega} \sim 1/\sin^4\frac{\theta}{2}$, see equation 1.12), which accounts for the distribution across the width (18 cm) of the detector bars.

The combined effects give rise to a distribution pattern of electrons at the focal plane. Fig. 2.7 shows the distribution of elastically and inelastically scattered electrons on the focal plane (beam's eye view). The elastically scattered electrons have a "moustache-shaped" distribution (Fig. 2.8) in each octant (the open space between two coils).

These optical properties of the QTOR magnet had been studied through early simulations to optimize the design of the magnet and the position of the target and the detector plane [16]. In those simulations, the coils were modeled out of circular arc and straight conductor segments. A magnetic field calculation was then carried out to generate a field map by integrating over the distribution of conductor current density using the Biot-Savart Law (as described in section 3.1.2). The field map was input into the GEANT[4] simulation package developed for the experiment, and the trajectories of electrons were tracked. The simulation results showed that the QTOR design had the required focusing and separating properties. The optimum positions of the target and the focal plane are 6.5 m upstream and 5.7 m downstream from the center of the QTOR, respectively, for a current of 8615 A in the QTOR conductor.

[4]GEANT is a set of simulation software packages that describe the passage of particles through the matter[17][18][19].

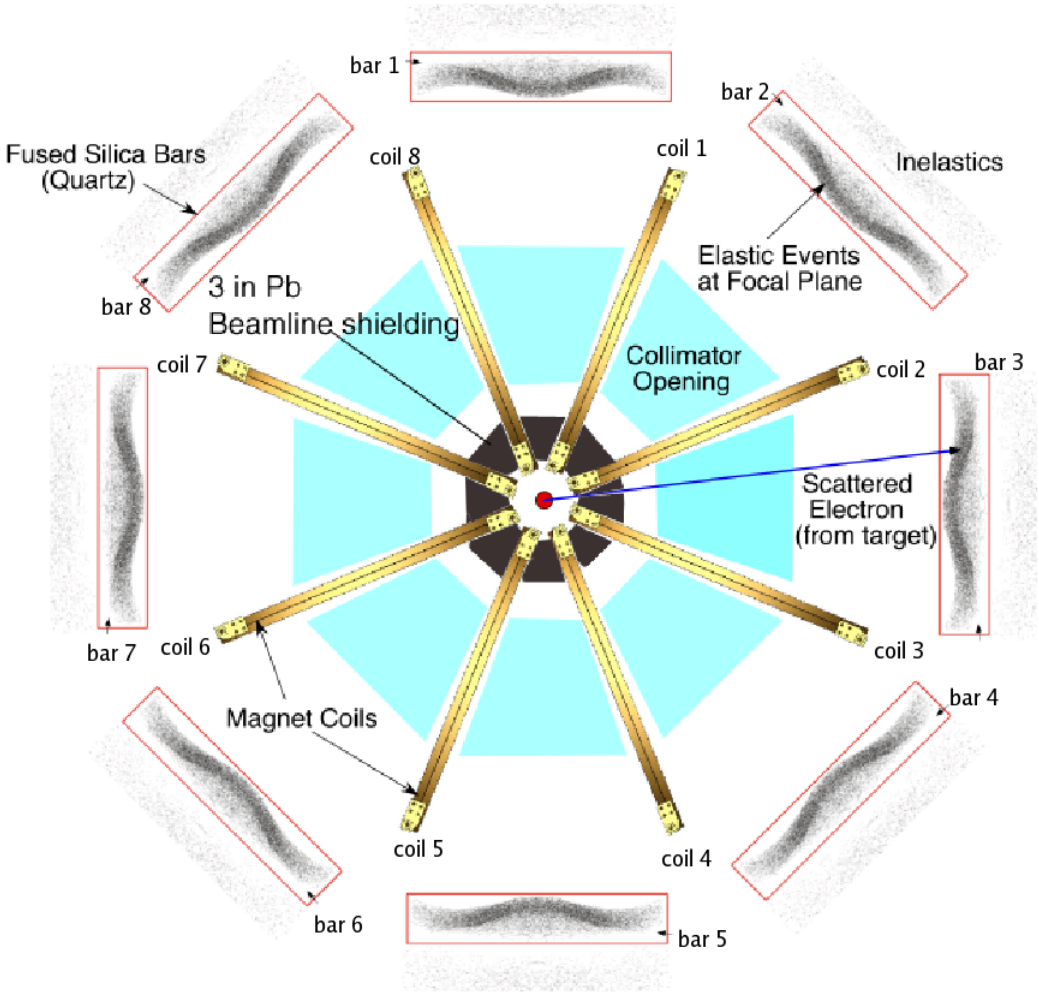

Figure 2.7: Electron distribution (beam's eye view). The coils and detector bars (or openings between coils) are numbered 1-8.

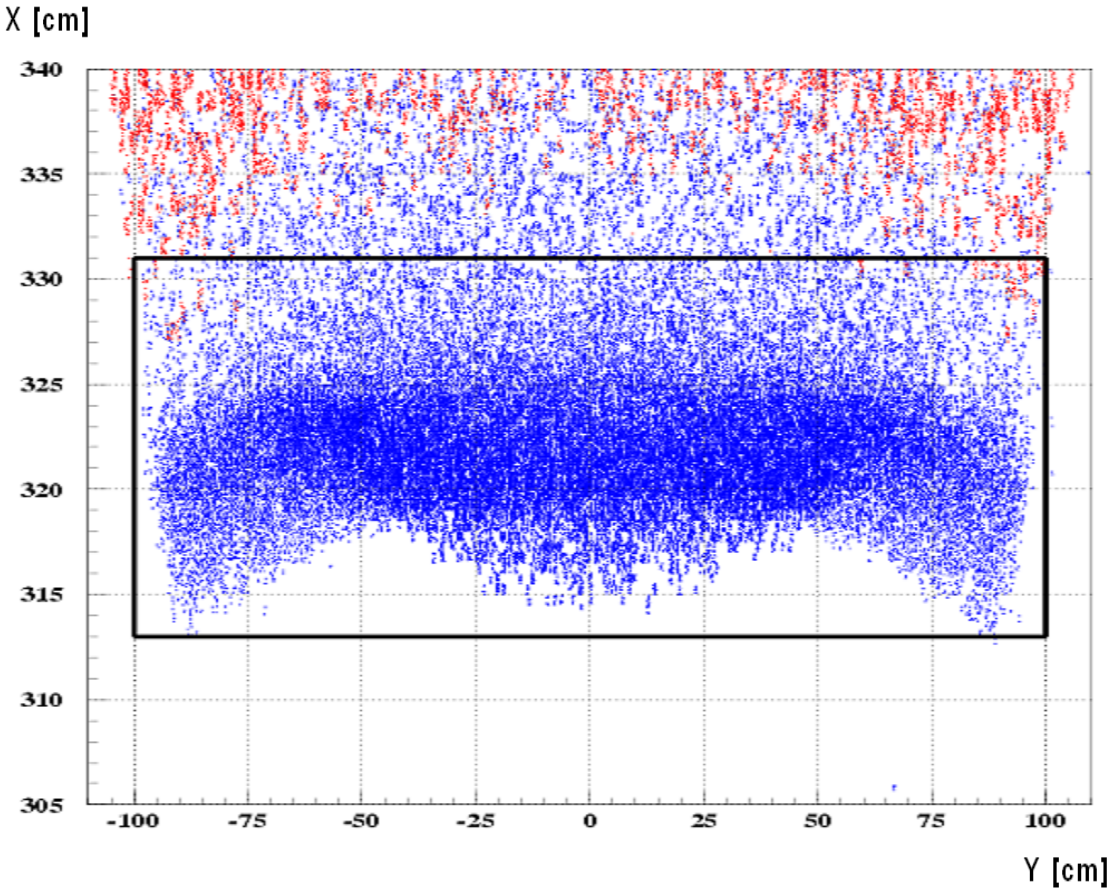

Figure 2.8: Electron distribution at focal plane (Z = 570 cm) in one octant [21]. The majority of elastic events (blue dots), which should be within the detector's acceptance (black frame), are in the shape of a "moustache". The inelastic events (red dots) are distributed above the "moustache", and will make the minimum contribution to the detector signals. These distributions were generated by a GEANT simulation with $\theta_e = 9.0^o \pm 2.0^o$ and $\phi_e = 0.0^o \pm 15.0^o$. X, Y and Z coordinates are defined in the sector frame (see 3.2.1), i.e. X and Y are defined across and along the detector bars, respectively, Z is along the beam line, and the origin is at the center of the QTOR magnet.

2.2 The Design and Manufactured QTOR Coils

The original design drawings issued for QTOR coils, conductor, inter-coil connection bars can be found in Appendix A. Unfortunately, the manufacturer[5] was not able to fabricate the coils exactly according to the design, due to coil winding difficulties (see Fig. 2.9). Thus, the original specifications had to be revised during the fabrication process to adapt to the manufacturing capability. The revised version of the coil specifications is shown in Fig. 2.11.

These specifications required a total of eight coils to be fabricated. The coils will be assembled to constitute QTOR by aligning them in a support frame with an angular separation of 45^{o} between two adjacent coils[6]. One extra coil (the ninth coil) was made as a spare. The total length of each coil is 3.68 m (not including the leads) and the total width is 1.48 m. Two pancake structures, called layer-1 pancake and layer-2 pancake, respectively, are assembled to form a coil. Each pancake has 13 turns of windings. The conductor material is OFHC (Oxygen-Free High Conductivity) copper. The bare copper is insulated by fiberglass and epoxy coating. Fig. 2.10 shows a manufactured coil. The total weight for each coil (bare copper) is about 3300 kg.

The desired magnetic field strength requires a driven current of about 9 kA. This current can cause a voltage drop of about 18 V on each coil (26 turns of windings) since the resistance of a coil at 50 ^{o}C is $\sim$ 1.9 mΩ. The total power dissipation of QTOR is $\sim$ 1.2 MW (I = 8615 A, $T = 50^{o}$), which is carried away by the cooling water.

The manufacturing control reports issued by Sigmaphi, the manufacturer, indicated some dimensional inconsistencies. Therefore, an on-site inspection (at MIT-Bates) was made, and some further measurements were performed on the finished coils. The reconciled set of measurements representing all the individual pancake layers is given in Appendix B. Comparing with the revised design, the reconciled results show that the manufactured coils have as-built dimensions which are generally in good agreement. For example, the coil design specifies a pancake width of 1483$\pm$4 mm, the layer-1 pancake length of 3679 $\pm$ 3 mm and layer-2 pancake length of 3639 $\pm$ 3 mm. Fig. 2.12

[5]The coils were manufactured at Sigmaphi in Vannes, France, in 2005.

[6]At the time of writing, the QTOR assembly is underway at MIT-Bates Linear Accelerator Center, Middleton, MA, USA.

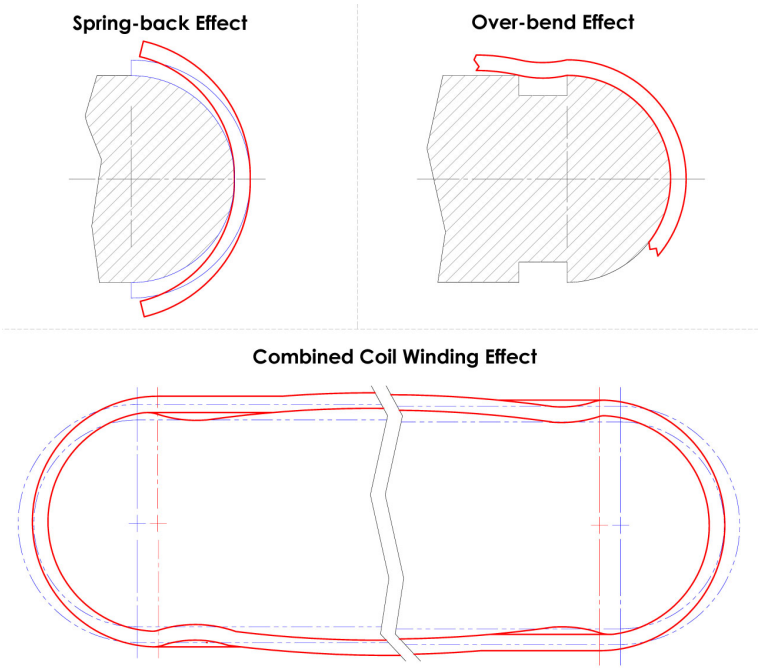

Figure 2.9: Coil winding effects, which result in the deformation of coils.

This item has been removed due to copyright issues. To view it, refer to its source.

Figure 2.10: A manufactured coil (coil-1, the spare coil). Photo by Guy Burguin (SIGMAPHI, France)

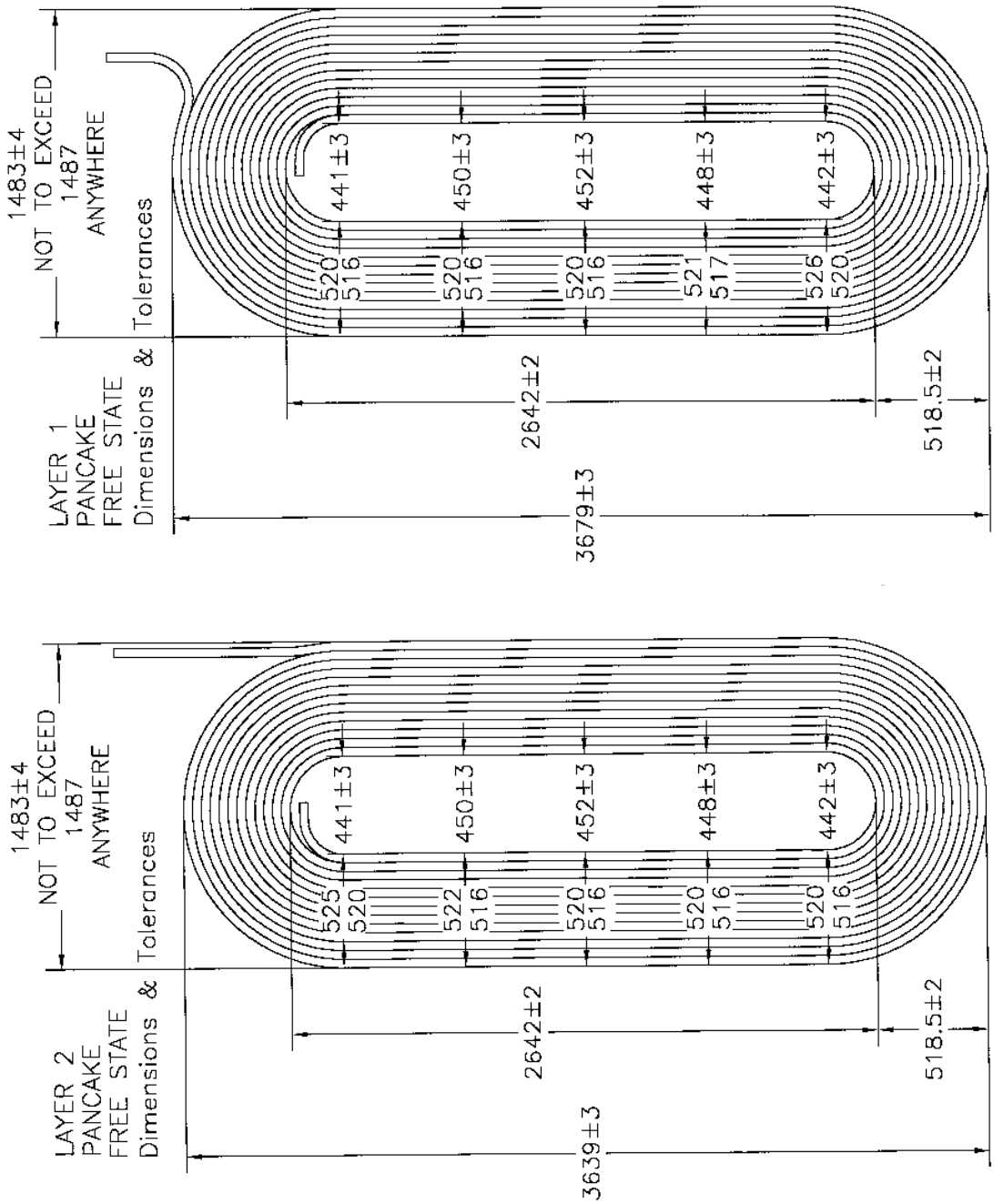

Figure 2.11: Revised coil specifications for Layer 1 (top) and Layer 2 (bottom) (Units: mm).

summarizes the pancake widths, measured near the exit end, center and entrance end. Fig. 2.13 presents a summary of pancake lengths; with a few exceptions, these results fall within the revised specifications. However, compared with the original design, on average, the manufactured coils are 10 mm wider and 16 mm shorter and the straight section is 22 mm shorter.

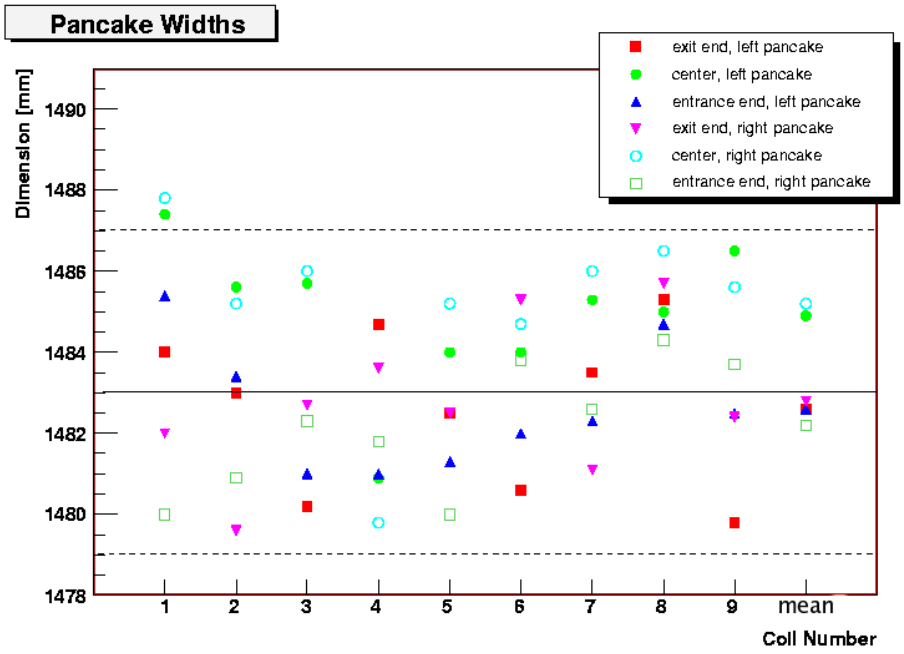

Figure 2.12: Pancake widths

2.3 Motivation for the Magnetic Field Simulation and Mapping

The Q^p_{Weak} experiment is a high precision experiment. In order to achieve the required precision, an in-depth study of the magnetic field generated by the QTOR spectrometer is needed. This study involves both magnetic field simulation and mapping, which must be carried out in the preparation phase of the experiment. In the preparation of the experiment, we need to simulate the tracking system, study the response of detectors, analyze the systematic uncertainties, etc. so as to optimize the experimental design. All of these studies in turn need a magnetic field map as input. Since a

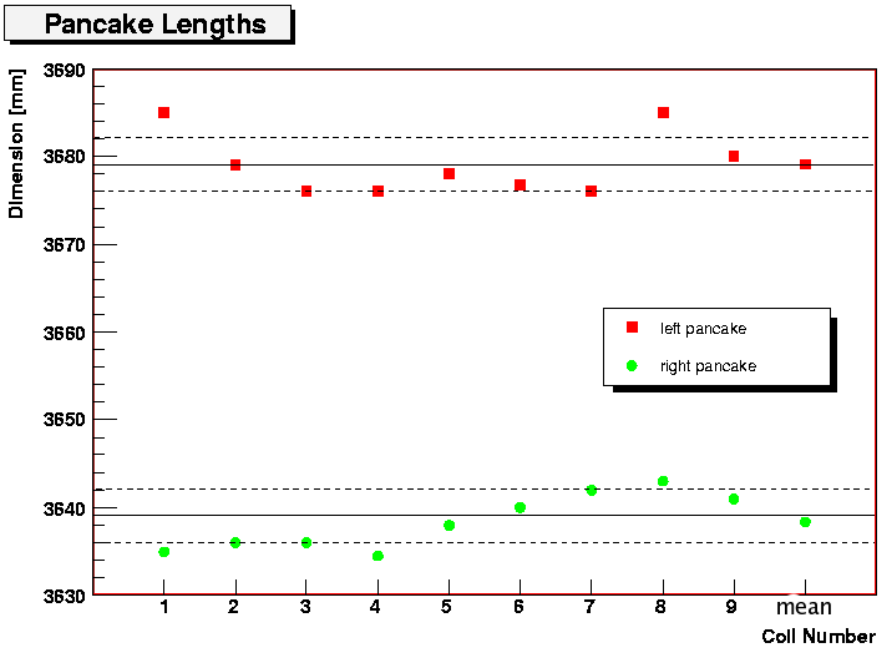

Figure 2.13: Pancake lengths

real field map can not be measured in the early phase of experimental preparation, the only way to obtain a realistic field map is through simulation.

Coil misalignments will cause the position and shape of the electron distribution on the detector bars to differ from the ideal. Using a calculated field map based on ideal identical coils, studies of tracking, detector response and systematic error sensitivities set the tolerances on the coil alignment and QTOR positioning. For example, Fig. 2.14 shows the effect of displacing one coil radially, and Fig. 2.15 shows the effect of an azimuthal rotation of a coil by $\pm 1^{o}$ about the beam line [20]. More GEANT simulations show that the tolerances on QTOR Magnet positioning and coil alignment are: radial positioning of each coil $\sim$ 3 mm, azimuthal positioning $\sim 0.1^{o}$, the overall alignment of the magnet transverse to the beam $\sim$ 3 mm [20]. Therefore, we need to measure the fields at some characteristic field points to infer the positions of coils to an adequate accuracy. On the other hand, the field integral $\int Bdl$ along the nominal electron trajectories should be matched to $\pm 0.4\%$ because of the requirement of Q^2 determination [33], and the axial symmetry of the magnetic field must also

be verified. Therefore, an accurate magnetic field map must be obtained through field mapping. In addition, due to some limits, such as the capabilities of the field mapping device, the huge cost of power consumption, and so on, not all field points can be measured at the full operating current. To achieve adequate knowledge of the field of the QTOR magnet, simulations must be carried out, followed by experimental measurements of the field at some selected points, to achieve more confidence at those field points that are not measured.

All of these considerations motivate us to conduct a precise QTOR magnetic field simulation and field mapping. The details are discussed in the following chapters.

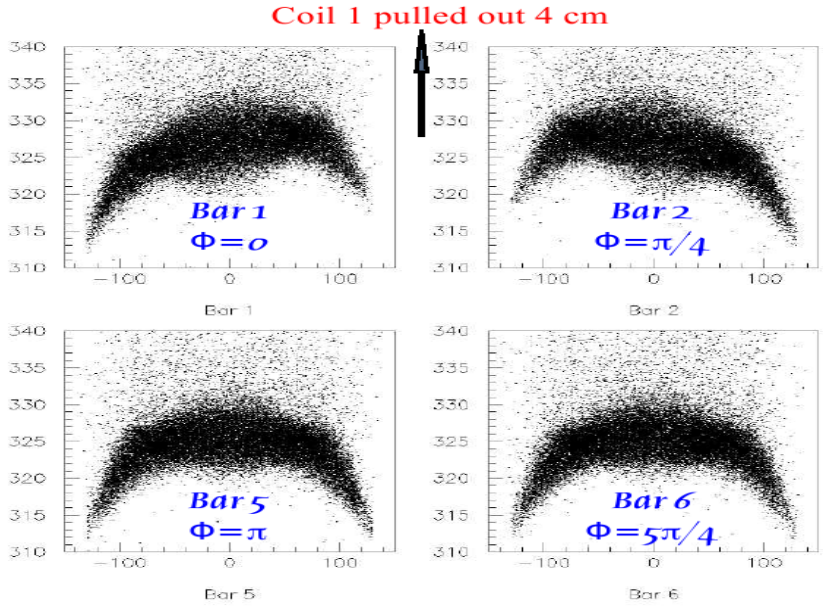

Figure 2.14: Effect of displacing one coil radially (courtesy J. Birchall, used with permission). The coils and detector bars are numbered 1 - 8 (refer to Fig. 2.7).

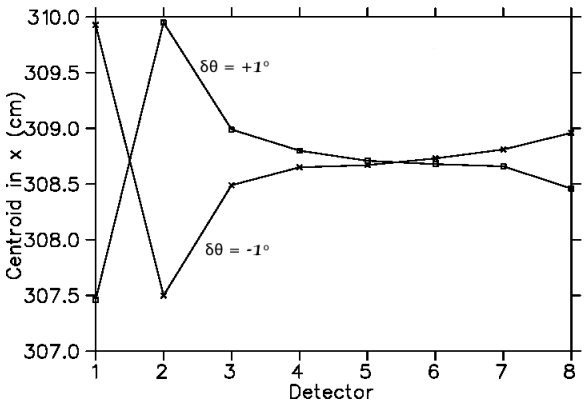

Figure 2.15: Movement of centroids for the elastic electron distribution across the widths of the detector bars when coil 1 is rotated by $\pm 1^{o}$ azimuthally about the beam line (courtesy J. Birchall, used with permission).

Chapter 3

Calculating the Magnetic Field

For an iron-free magnet, if a proper model of the distribution of conductor current density can be set up, the magnetic field can then be calculated using the Biot-Savart Law through numerical integration. This magnetic field calculating technique is adopted in the magnetic field calculation of the QTOR, which is introduced in detail in this chapter. This chapter also introduces many other details about different aspects of the QTOR simulation, including descriptions of the basic functions and algorithms of the magnetic field calculation programs and the procedure of setting up the realistic model based on the fabricated coils. The simulation results are discussed as well.

3.1 Basic Functions and Algorithms

3.1.1 The Functions of the Simulation Programs

The simulation programs of QTOR should provide not only a calculated field map, but also the data and analysis for the in-depth study of the magnetic field. These are difficult to obtain from general-purpose commercial field simulation software, such as TOSCA [34] and ANSYS [35]. The simulation programs must fulfil the following functions:

- Generate the field map (a collection of field point coordinates and the corresponding values of field components) over a specific field region;

- Calculate the fields and the field gradients at any selected field points;
- Perform scans to locate the characteristic field points (e.g. zero-crossing field points);
- Trace electron trajectories and compute the field integrals along the electron trajectories.

Apart from these basic functions, we also require the simulation programs to calculate the field for the the coils at nominal or specific positions, as well as the field for the coils randomly displaced. Thus, we can analyze the effects of coil displacement. All these requirements have been met by the simulation programs based on a realistic model of the QTOR.

3.1.2 Basic Algorithms

The magnetic field of QTOR is produced by a steady electric current. The differential element of magnetic field, $d\mathbf{B}$, produced by a steady current I can be described by the Biot-Savart Law [36]:

$$d\mathbf{B}(\mathbf{r}) = \frac{\mu_0}{4\pi}\frac{Id\mathbf{l}\times\mathbf{r}}{r^3}, \tag{3.1}$$

where $d\mathbf{l}$ is the differential length vector of the current element, $\mathbf{r}$ is the displacement vector pointing from the current element to the point of observation (field point), and μ_0 is the permeability of free space. If the QTOR is segmented into many tiny pieces that act as current elements, and in a certain Cartesian coordinate system the position vector of the i^{th} current element is denoted as $\mathbf{r}_i(x_i, y_i, z_i)$, then the differential length vector $d\mathbf{l}$ of that current element can be written in terms of its unit directional vector $(u_x,\ u_y,\ u_z)$ as:

$$d\mathbf{l}_i = dl_i\ (u_{ix}\,\mathbf{i} + u_{iy}\,\mathbf{j} + u_{iz}\,\mathbf{k}), \tag{3.2}$$

where the $\mathbf{i}$, $\mathbf{j}$ and $\mathbf{k}$ are unit direction vectors of $\mathbf{x}$, $\mathbf{y}$ and $\mathbf{z}$. The displacement vector pointing from the i^{th} current element to field point $\mathbf{r}_j(x_j, y_j, z_j)$ can be written as:

$$\mathbf{r}_{ji} = (x_j - x_i)\,\mathbf{i} + (y_j - y_i)\,\mathbf{j} + (z_j - z_i)\,\mathbf{k} = x_{ji}\,\mathbf{i} + y_{ji}\,\mathbf{j} + z_{ji}\,\mathbf{k}. \tag{3.3}$$

Following the equation 3.1, we can obtain the field components produced by the i^{th} current element at point j:

$$dB_x = \frac{\mu_0}{4\pi} I_i \, dl_i \, (u_{iy} \cdot z_{ji} - u_{iz} \cdot y_{ji}) / r_{ji}^3 \, , \tag{3.4}$$

$$dB_y = \frac{\mu_0}{4\pi} I_i \, dl_i \, (u_{iz} \cdot x_{ji} - u_{ix} \cdot z_{ji}) / r_{ji}^3 \, , \tag{3.5}$$

$$dB_z = \frac{\mu_0}{4\pi} I_i \, dl_i \, (u_{ix} \cdot y_{ji} - u_{iy} \cdot x_{ji}) / r_{ji}^3 \, . \tag{3.6}$$

From equations 3.4 – 3.6, we can calculate the field at any selected field point through numerical integration, i.e., summing over each current element's contribution to the field, if we have the knowledge about the positions, lengths and directions of all current elements in the QTOR, as well as the value of current in each current element.

Another important function of the simulation programs is to trace electrons through the spectrometer (i.e., find out the electron's position coordinates and velocities) and compute the field integrals along the electron trajectories, which is also based on the field calculation mentioned above. The Lorentz force **F** for a charged particle with relativistic mass m, electric charge q and velocity **v** in a magnetic field **B** is:

$$\mathbf{F} = m\frac{d^2\mathbf{r}}{dt^2} = q\mathbf{v} \times \mathbf{B}, \tag{3.7}$$

where $\mathbf{r}(x, y, z)$ is the displacement vector of the particle. In component form, equation 3.7 becomes:

$$\frac{d^2x}{dt^2} = \frac{q}{m}(v_y B_z - v_z B_y) \, , \tag{3.8}$$

$$\frac{d^2y}{dt^2} = \frac{q}{m}(v_z B_x - v_x B_z) \, , \tag{3.9}$$

$$\frac{d^2z}{dt^2} = \frac{q}{m}(v_x B_y - v_y B_x) \, . \tag{3.10}$$

Then, the coupled differential equations of motion can be written as:

$$\frac{dx}{dt} = v_x \,, \tag{3.11}$$

$$\frac{dv_x}{dt} = \frac{q}{m}(v_y B_z - v_z B_y) \,, \tag{3.12}$$

$$\frac{dy}{dt} = v_y \,, \tag{3.13}$$

$$\frac{dv_y}{dt} = \frac{q}{m}(v_z B_x - v_x B_z) \,, \tag{3.14}$$

$$\frac{dz}{dt} = v_z \,, \tag{3.15}$$

$$\frac{dv_z}{dt} = \frac{q}{m}(v_x B_y - v_y B_x) \,, \tag{3.16}$$

which can be solved iteratively. For example, through setting dt in equations 3.11 - 3.12 as a small step size (i.e., interval $dt = h$), we can write the coupled different equations and the particle's positions and velocities at step $(i + 1)$ in terms of step (i) as:

$$x_{(i+1)} = x_{(i)} + dx_{(i)}, \tag{3.17}$$

$$y_{(i+1)} = y_{(i)} + dy_{(i)}, \tag{3.18}$$

$$z_{(i+1)} = z_{(i)} + dz_{(i)}, \tag{3.19}$$

$$dx_{(i+1)} = v_{x(i)} \cdot h, \tag{3.20}$$

$$dy_{(i+1)} = v_{y(i)} \cdot h, \tag{3.21}$$

$$dz_{(i+1)} = v_{z(i)} \cdot h, \tag{3.22}$$

$$v_{x(i+1)} = v_{x(i)} + dv_{x(i)}, \tag{3.23}$$

$$v_{y(i+1)} = v_{y(i)} + dv_{y(i)}, \tag{3.24}$$

$$v_{z(i+1)} = v_{z(i)} + dv_{z(i)}, \tag{3.25}$$

$$dv_{x(i+1)} = \frac{q}{m}[v_{y(i)} \cdot B_{z(i)} - v_{z(i)} \cdot B_{y(i)}] \cdot h, \tag{3.26}$$

$$dv_{y(i+1)} = \frac{q}{m}[v_{z(i)} \cdot B_{x(i)} - v_{x(i)} \cdot B_{z(i)}] \cdot h, \tag{3.27}$$

$$dv_{z(i+1)} = \frac{q}{m}[v_{x(i)} \cdot B_{y(i)} - v_{y(i)} \cdot B_{x(i)}] \cdot h. \tag{3.28}$$

Thus, the numerical values at the $(i+1)^{th}$ step can be calculated in terms of values for position, velocity and magnetic field at the i^{th} step if the initial conditions (x_0, y_0, z_0) and (v_{0x}, v_{0y}, v_{0z}) are known. For a scattered electron, the initial conditions can be specified using e-p scattering kinematics. In order to improve calculation accuracy, the well-known 4^{th} order Runge-Kutta method [37] is applied in the actual simulation program, since it only needs one starting point and has relatively higher accuracy.

In addition, because the field integral can be expressed as (where $d\mathbf{l}$ is the displacement along the electron trajectory):

$$\int \mathbf{B} \times d\mathbf{l} = \int (dzB_y - dyB_z)\,\mathbf{i} + (dxB_z - dzB_x)\,\mathbf{j} + (dyB_x - dxB_y)\,\mathbf{k}, \tag{3.29}$$

by denoting the ξ component of field integral at the i^{th} step as $FI_{\xi(i)}$ ($\xi = x,\ y$ or z), we can obtain the field integral at $(i+1)^{th}$ step, i.e.,

$$FI_{x(i+1)} = FI_{x(i)} + h(v_{z(i)}B_{y(i)} - v_{y(i)}B_{z(i)}), \tag{3.30}$$

$$FI_{y(i+1)} = FI_{y(i)} + h(v_{x(i)}B_{z(i)} - v_{z(i)}B_{x(i)}), \tag{3.31}$$

$$FI_{z(i+1)} = FI_{z(i)} + h(v_{y(i)}B_{x(i)} - v_{x(i)}B_{y(i)}). \tag{3.32}$$

Since $v_{x(i)}$, $v_{y(i)}$, $v_{z(i)}$, $B_{x(i)}$, $B_{y(i)}$ and $B_{z(i)}$ can be acquired while tracking the particle, we can then conveniently evaluate the corresponding field integral along the particle's trajectory.

3.2 Realistic Model of the QTOR

If the QTOR is modeled properly, then the information about the as-built positions, lengths and directions of the current elements in the QTOR can be specified, and the magnetic field in turn can be calculated by summing over the contributions of all current elements. In order to model the QTOR, firstly we need to define the coordinate systems so as to conveniently define the geometry of the QTOR.

3.2.1 Coordinate Systems

In the simulation programs, several coordinate systems are defined. The most often used frame is the TOROID frame (or lab frame). In the TOROID frame (see Fig. 3.1 and Fig. 3.2 for reference), the X-axis points up vertically, the Y-axis is horizontal to the right, and the Z-axis is along the beam direction. The origin is at the center of the QTOR.

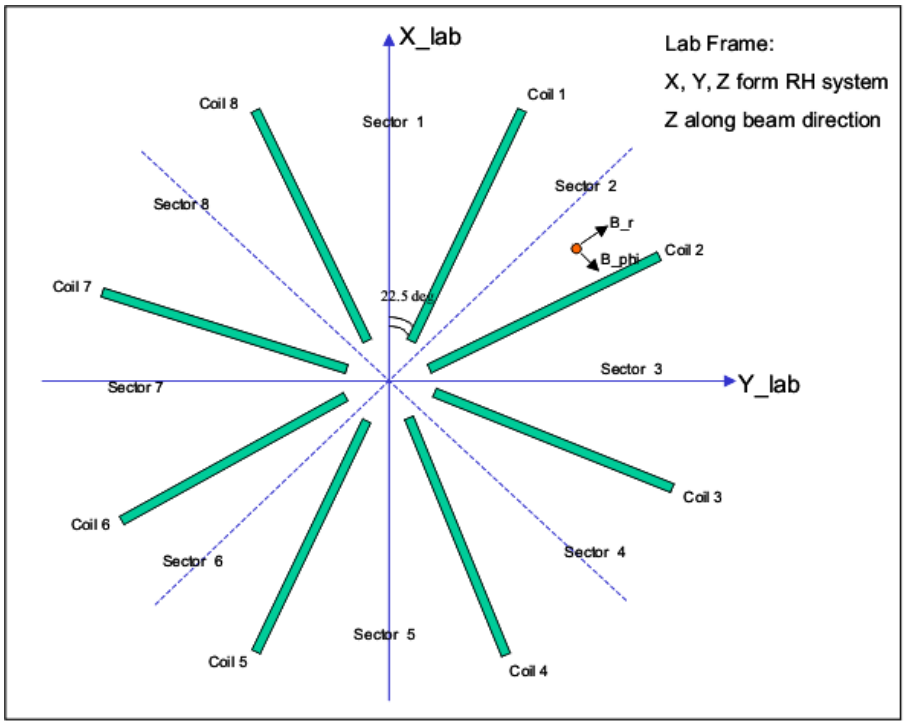

Figure 3.1: TOROID/lab frame

There are also some other coordinate systems defined in the simulation. For example, the SECTOR frame (see Figure 3.3) has the same Z-axis as the TOROID frame, but its X-axis is radially outward, bisecting the angle between two coils, and the Y-axis is perpendicular to the X-axis and in the direction to form a right-handed system. The SECTOR frame is defined for every sector of the magnet. Each SECTOR frame is convenient for describing the physical quantities and processes within that sector. The SECTOR frames are also convenient when we compare the physical quantities and processes in different sectors due to the symmetry of the toroidal magnet.

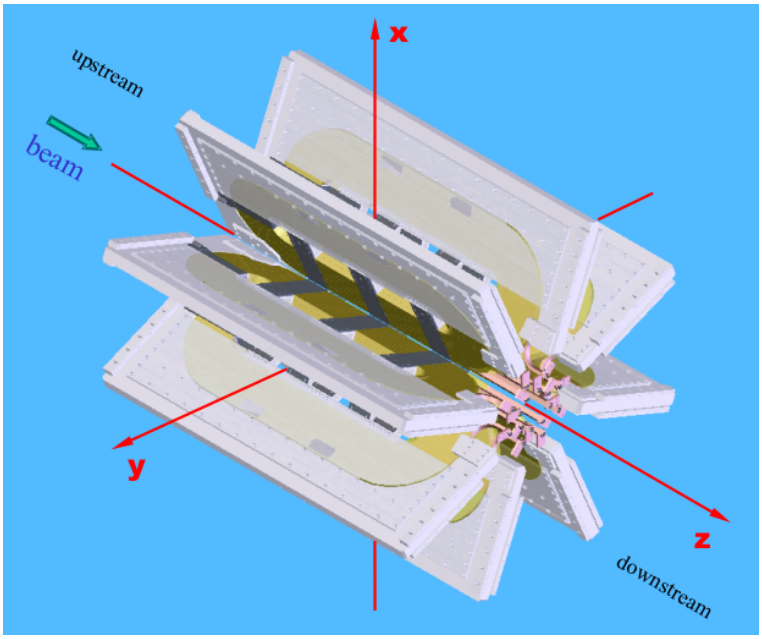

Figure 3.2: TOROID/lab frame shown with coils and coil carriers

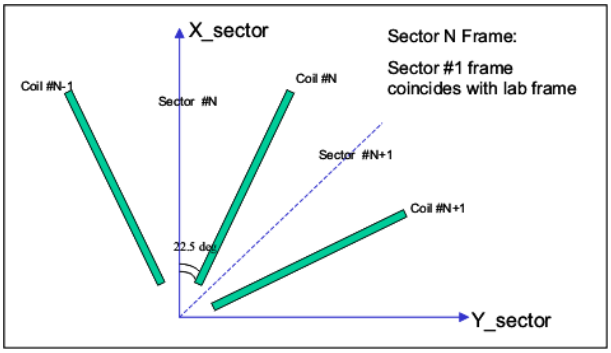

Figure 3.3: Sector N frame

The coil positions are numbered in the TOROID frame: the first coil is placed at azimuthal angle 22.5^o in the TOROID frame and the other coils are placed and numbered clockwise (looking downstream) from there. Sectors between two coils are also numbered clockwise with sector No.1 located between coil position No.8 and No.1. Thus, the SECTOR No.1 frame coincides with the TOROID frame (see Figure 3.1 for reference).

3.2.2 Procedure of Setting up a Realistic Model

From the algorithms mentioned in the previous section, we know that setting up a realistic model implies that we:

- define the position coordinates $\mathbf{r}_i(x_i, y_i, z_i)$ for each current element,
- calculate x, y and z components ($u_{ix},\ u_{iy},\ u_{iz}$) for the directional unit vector of the differential length vector $d\mathbf{l}_i$,
- specify the length dl_i for the differential length vector,
- and find the value of current I_i which flows through that current element.

This information can be obtained through the following procedure:

1. The conductors of the pancakes, the leads, the inter-pancake connecting bars and the inter-coil connecting bars are divided into small bars of about 2 cm length. The cross-section of each small bar (rectangular cross-section with a circle aperture in the middle) is further segmented into 4 areas (see Fig. 3.4). Thus, the QTOR is logically divided into many small pieces, and each small piece of the conductor is considered as a valid current element. Since the QTOR consists of eight coils, each coil consists of two pancake layers, and each pancake consists of two layers of current elements, there are in total 32 layers of current elements in the QTOR. The coordinates of the centroid of each current element are treated as the coordinates of the corresponding current element.

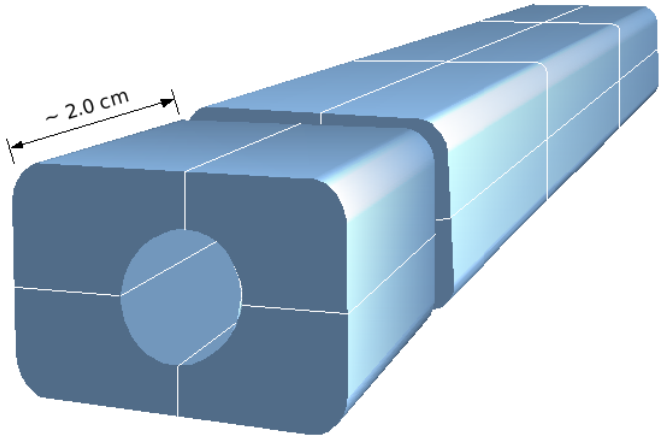

Figure 3.4: Coil conductors are logically divided into many small pieces longitudinally, and the conductor cross section is further segmented into four pieces as shown. Each segment acts as a current element. The current centroid is at ~ 1.040 cm vertically and ~ 1.634 cm horizontally for the segments, with respect to the center of the conductor cross section.

2. In the TOROID frame, we place each pancake onto the X-Z plane with the geometrical center of the pancake at (x_{center}, 0, z_{center}), respectively (Fig. 3.5). This is like placing the pancakes on a grid coordinate graph paper, and so the X and Z coordinates for each current element in that pancake, as well as the x and z components of the differential length vectors, are located and computed, and further stored in a large array. When locating the current elements, the actual measurements provided by the manufacturer on the fabricated pancakes and coils are used. Generally, the current elements in a given layer are well aligned in a plane, so we assume that they have the same Y coordinate. Thus, the Y coordinate for each current element is C if its centroid is at the positive side of the Y-axis or $-C$ if its centroid is at the negative side of the Y-axis (C = 1.634 cm, defined in Fig. 3.8), and the y components of the differential length vectors are zero. Then, we shift the pancakes in the Y direction to obtain the initial placements of coils (refer to Fig. 3.6 – Fig. 3.8, where the length of the conductor cross-section is denoted as L and the average spacing between two adjacent pancakes is denoted as D).

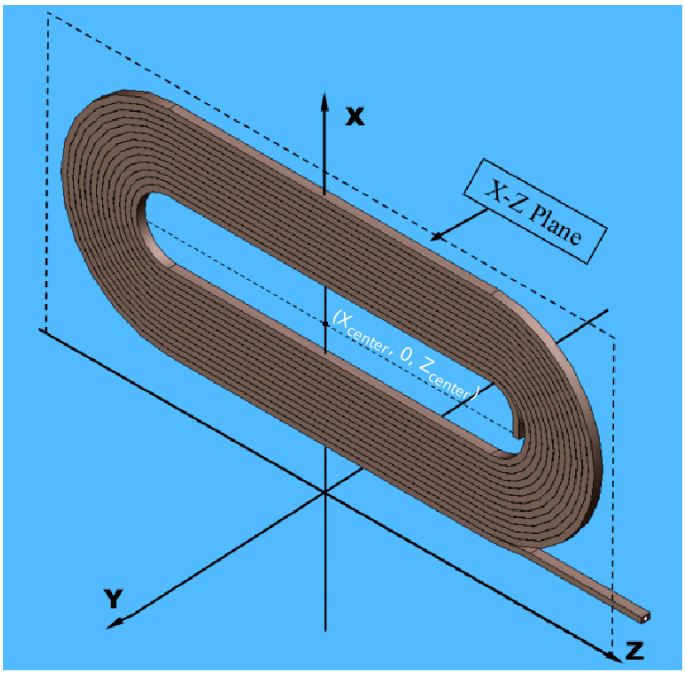

Figure 3.5: Initial placement of pancakes. Here, a pancake is placed on the X-Z plane in the lab frame.

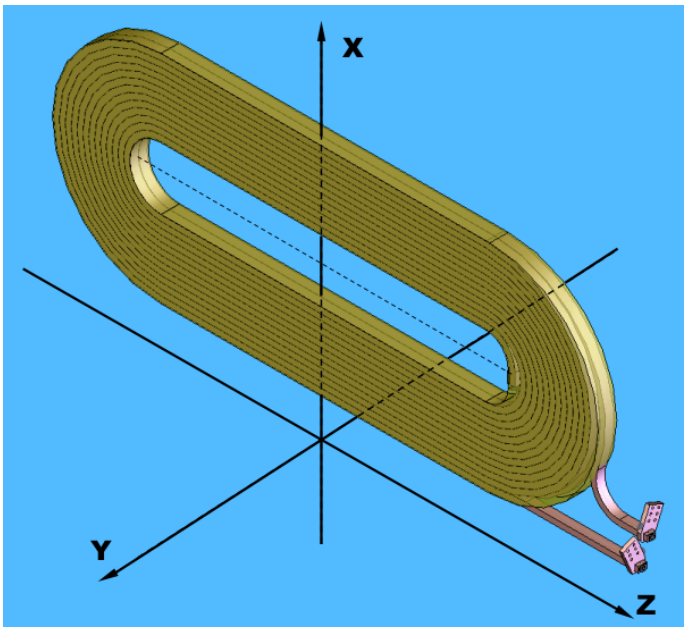

Figure 3.6: Initial placement of coils (isometric view)

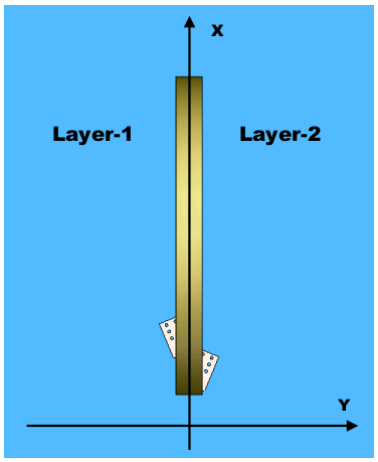

Figure 3.7: Initial placement of coils (looking downstream)

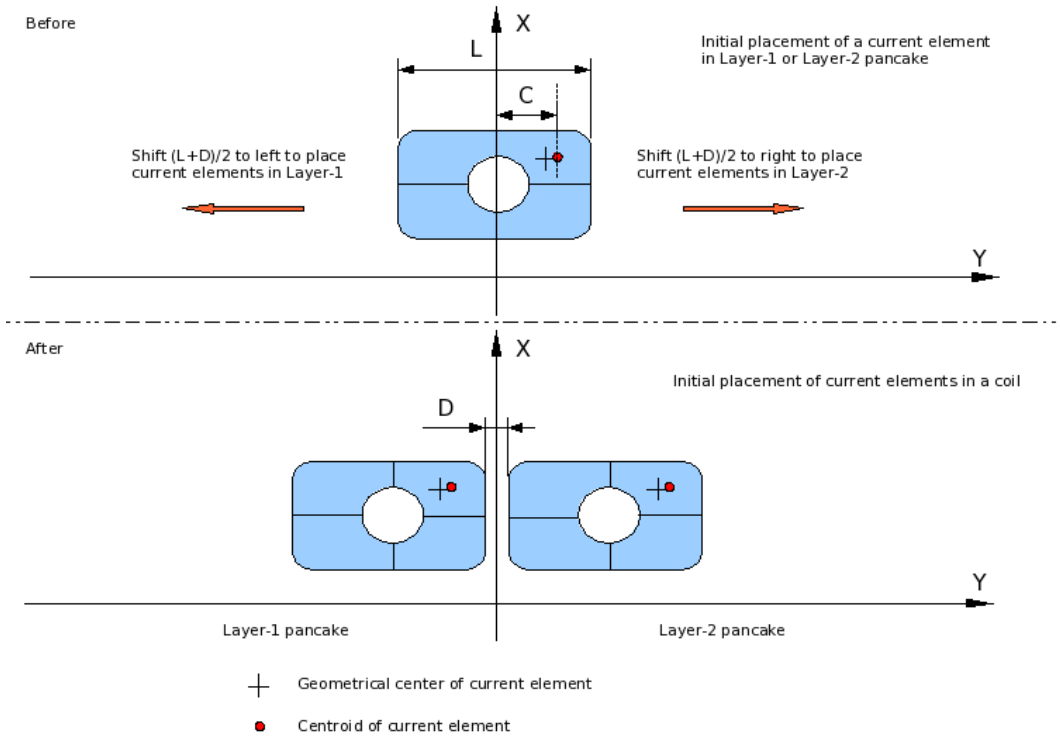

Figure 3.8: Shift of current element.

3. In order to account for the coil displacements (shifts and/or rotations) from their nominal locations[1], we define parameters of the coil displacements as follows (note that the center of the coil has coordinates ($x_{center},\ 0,\ z_{center}$)):

   - θ_x: rotational angle about an axis ("x-axis") that is parallel to the X-axis and passes through the point ($x_{center},\ 0,\ z_{center}$), in the direction $\mathbf{j} \times \mathbf{k}$,
   - θ_y: rotational angle about an axis ("y-axis") that is parallel to the Y-axis and passes through the point ($x_{center},\ 0,\ z_{center}$), in the direction $\mathbf{k} \times \mathbf{i}$,
   - θ_z: rotational angle about an axis ("z-axis") that is parallel to the Z-axis and passes through the point ($x_{center},\ 0,\ z_{center}$), in the direction $\mathbf{i} \times \mathbf{j}$,
   - dX: translation in the X-direction from the initial position,
   - dY: translation in the Y-direction from the initial position,
   - dZ: translation in the Z-direction from the initial position.

   The x-, y- and z- axes form a coordinate system (coil frame, see Fig 5.1 for reference). These displacement parameters are either produced randomly by the simulation programs, or are specified by the user for each coil, so as to investigate the effects of coil displacements. The coils are shifted according to the displacements resulting from the rotations and translations. Meanwhile, the differential length vectors are also corrected for the rotations. For example, for a current element located at the initial position ($x,\ y,\ z$) with an unit vector ($u_x,\ u_y,\ u_z$), the coil rotations by small angles (θ_x, θ_y, θ_z) will result in the corresponding current element displacements and unit vector changes. These changes are summarized in Table 3.1.

   The new position ($x',\ y',\ z'$) and the new unit vector ($u'_x,\ u'_y,\ u'_z$) then can be obtained by taking into account the coil translations dX, dY, dZ, and summing up all the changes resulting

[1] It is much easier to add in the coil displacements when the coils are placed in their initial positions as specified above than when they are in their final azimuthal positions.

Rotation of coil		θ_x	θ_y	θ_z
Current element displacement	dx	0	$R_z \sin\theta_y$	$R_x (\cos\theta_z - 1)$
	dy	$-R_z \sin\theta_x$	0	$R_x \sin\theta_z$
	dz	$R_z (\cos\theta_x - 1)$	$-R_x \sin\theta_y$	0
Change in unit vector	du_x	0	$u_z \sin\theta_y + u_x (\cos\theta_y - 1)$	$u_x (\cos\theta_z - 1)$
	du_y	$-u_z \sin\theta_x$	0	$u_x \sin\theta_z$
	du_z	$u_z (\cos\theta_x - 1)$	$-u_x \sin\theta_y + u_z (\cos\theta_y - 1)$	0

Table 3.1: The current element displacements and unit vector changes for coil rotations, where $R_x = x - x_{center}$ (x_{center} is the distance between x- and X- axes), $R_z = z - z_{center}$ (z_{center} is the distance between z- and Z- axes), and u_x, u_y, u_z are the components of the unit vector.

from each rotation as (the small-angle condition must be kept):

$$x' = x + dx(\theta_x) + dx(\theta_y) + dx(\theta_z) + dX \,, \tag{3.33}$$

$$y' = y + dy(\theta_x) + dy(\theta_y) + dy(\theta_z) + dY \,, \tag{3.34}$$

$$z' = z + dz(\theta_x) + dz(\theta_y) + dz(\theta_z) + dZ \,, \tag{3.35}$$

$$u'_x = u_x + du_x(\theta_x) + du_x(\theta_y) + du_x(\theta_z) \,, \tag{3.36}$$

$$u'_y = u_y + du_y(\theta_x) + du_y(\theta_y) + du_y(\theta_z) \,, \tag{3.37}$$

$$u'_z = u_z + du_z(\theta_x) + du_z(\theta_y) + du_z(\theta_z) \,. \tag{3.38}$$

Although the finite rotations do not commute, the approximations here are quite good for small angle rotations. The length of the unit vector may change slightly after a rotation. In order to preserve the length of the differential length vector, the unit vector needs to be re-normalized after all operations have been carried out.

The zero-crossing analysis (to be discussed in Chapter 5) needs to simulate the QTOR mis-

alignment (shifts and rotation with respect to the field mapper), which can also be simulated via coil shifts and rotations. In the simulation programs, the QTOR shifts and rotations are expressed with respect to the lab frame, and the coil shifts and rotations are expressed with respect to the coordinate frame shown in Fig. 5.1 (referred to as the "coil frame").

The effect on coil # 1, when the entire QTOR magnet is displaced by ΔX along X, is equivlent to the shifts: $dx = \Delta X \cos 22.5^{\circ}$ and $dy = -\Delta X \sin 22.5^{\circ}$, as shown in Fig. 3.9 (the individual coil shifts are expressed when the coil is in the vertical X-Z plane). Using $\cos 22.5^{\circ} = 0.924$ and $\sin 22.5^{\circ} = 0.383$, the individual coil shifts for QTOR shifted 1 unit along X and Y are summarized in Table 3.2, where the last two columns are obtained from rotating the diagram (Fig. 3.9) and re-labeling the axes.

Coil #	Shift $\Delta X = 1$, along X		Shift $\Delta Y = 1$, along Y	
	$dx = \cos\phi_n$	$dy = -\sin\phi_n$	$dx = \sin\phi_n$	$dy = \cos\phi_n$
1	0.924	- 0.383	0.383	0.924
2	0.383	- 0.924	0.383	0.383
3	- 0.383	- 0.924	0.924	- 0.383
4	- 0.924	- 0.383	0.383	- 0.924
5	- 0.924	0.383	- 0.383	- 0.924
6	- 0.383	0.924	- 0.924	0.383
7	0.383	0.924	- 0.924	0.383
8	0.924	0.383	- 0.383	0.924

Table 3.2: Corresponding coil shifts (in the coil frame) for displacement of the QTOR by 1 unit along the X and Y axes, where $\phi_n = (45n - 22.5)^{\circ}$, and n is the coil number.

A rotation of QTOR by $d\phi$ about the Z-axis is equivalent to the following rotations and displacements of each coil (with respect to the coil frame):

- rotation by $d\phi$ about the Z-axis,
- shift $dx = R_c\ (\cos d\phi - 1)$,
- and shift $dy = R_c \sin d\phi$,

where R_c is the distance from the coil center line to the beam axis (see Fig 3.10).

4. The final step is to rotate all coils about the Z-axis from their initial positions (in the X-Z plane) to their final azimuthal positions (see Fig. 3.11). By using a current element as representative, we can write this transformation as:

$$\begin{pmatrix} x' \\ y' \\ z' \end{pmatrix} = \begin{bmatrix} \cos\phi & -\sin\phi & 0 \\ \sin\phi & \cos\phi & 0 \\ 0 & 0 & 1 \end{bmatrix} \begin{pmatrix} x \\ y \\ z \end{pmatrix} \tag{3.39}$$

$$\begin{pmatrix} u'_x \\ u'_y \\ u'_z \end{pmatrix} = \begin{bmatrix} \cos\phi & -\sin\phi & 0 \\ \sin\phi & \cos\phi & 0 \\ 0 & 0 & 1 \end{bmatrix} \begin{pmatrix} u_x \\ u_y \\ u_z \end{pmatrix} \tag{3.40}$$

where ϕ is the azimuthal angle of each coil, and $\phi = 22.5^{\text{o}}, 67.5^{\text{o}}, \cdots, 337.5^{\text{o}}$ in the TOROID frame.

This procedure was used for setting up the position and the differential length vector for each current element in the coils. A similar procedure was followed for the inter-pancake connections and inter-coil connections (described in Appendix A). The incoming and outgoing current leads were treated separately (their shapes and positions can be seen in Fig. 3.12).

The current densities are assumed to be uniform in the straight sections of coils. The current of a single current element in the straight sections of coils is 1/4 of the total current, i.e. $I_i = I_{total}/4$, since the cross-section of conductor is divided into 4 equal areas. However, in the curved sections, the inner layer has a smaller radius of curvature than the outer layer, and hence the length of the inner layer (L_{inner}) is shorter than the length of the outer layer (L_{outer}). Therefore, the inner layer conductor has a smaller resistance and larger current than the outer layer conductor. For the curved

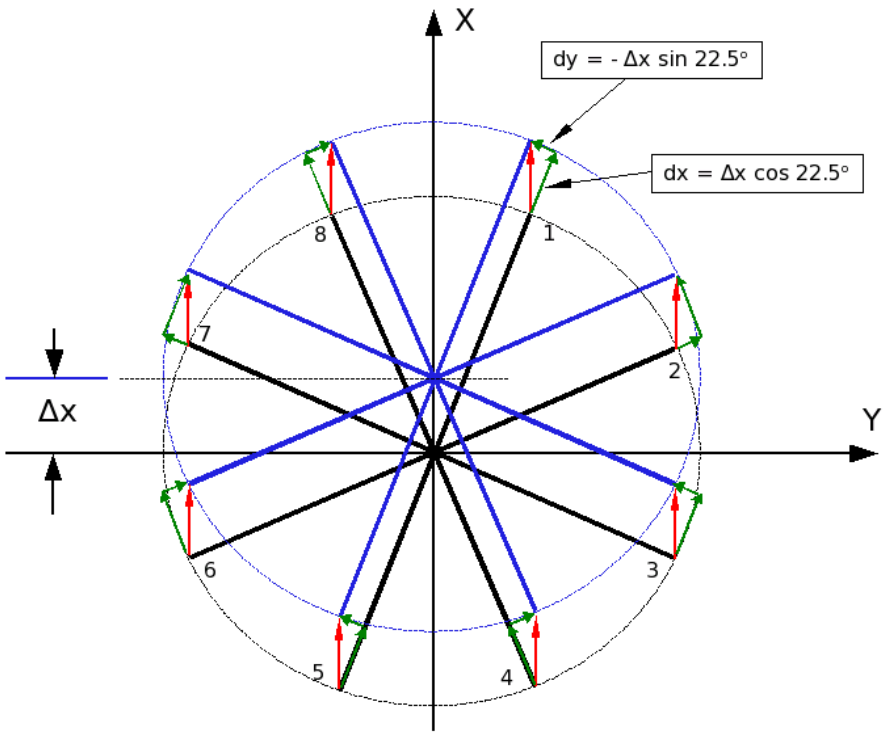

Figure 3.9: QTOR shifted by ΔX along X, where the black and blue lines indicate the coil positions before and after the shift, respectively; the red arrows indicate the coil shifts in the lab frame, and the green arrows indicate the corresponding shifts of individual coil in its own frame (the corresponding individual coil frame).

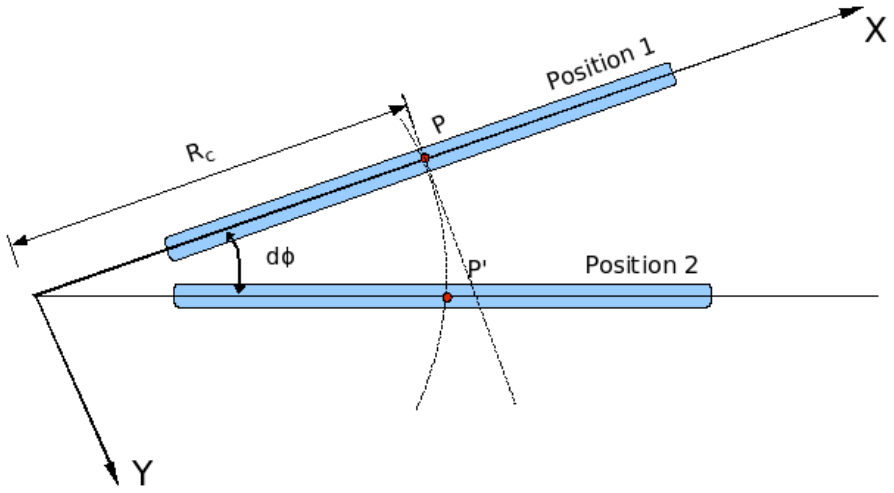

Figure 3.10: QTOR rotation

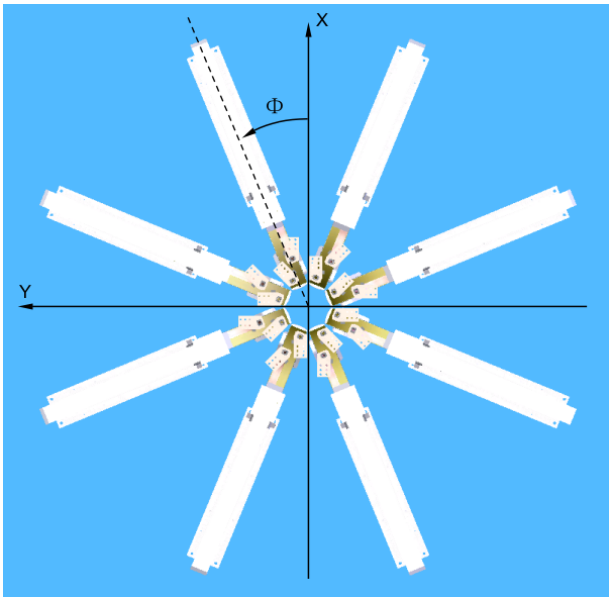

Figure 3.11: Final positions of coils in the lab frame (looking upstream, coil carriers are also shown)

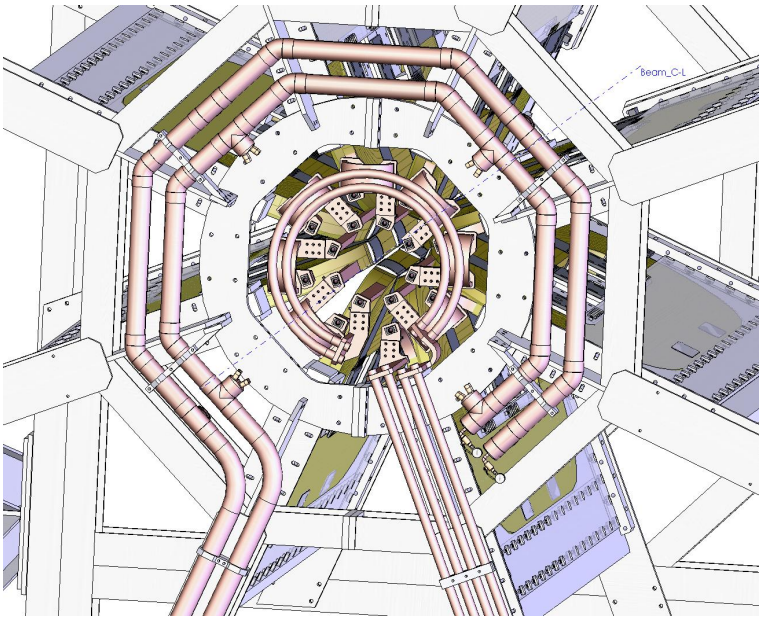

Figure 3.12: Leads and jumpers at the downstream end of the QTOR magnet (the large-diameter tubes are for plumbing). They are arranged at the downstream end so that their influnces on the magnetic field can be suppressed, since this region is far away from the envelope of electron trajectories.

sections in the coils, for example, we can easily obtain:

$$\frac{I_{inner}}{I_{outer}} = \frac{R_{outer}}{R_{inner}} = \frac{L_{outer}}{L_{inner}} \tag{3.41}$$

$$I = 2I_{inner} + 2I_{outer}. \tag{3.42}$$

The ratio I_{outer}/I_{inner} depends only on the bend radius of the conductor.

From the above discussion, all the required information about the current density distribution in the QTOR can be obtained, and then we can perform the numerical integral to calculate the field at any selected point, and further to perform all the required functions for the simulation.

3.2.3 Modeling the Shape of the Coils

For locating the positions of current elements of the pancakes on the X-Z plane, the experimental measurements of the pancakes made by the manufacturer and augmented by the on-site measurements were used. Only about thirty measurements were made for each physical pancake. That means we only have a limited number of points from which to infer the locations of all the current elements in a pancake (the data for the actual measurements, reduced to the bare copper dimensions, are shown in Appendix B).

Each turn of the coil windings, which includes two layers of current elements, was divided into 6 sections (see Fig. 3.13). An ideal pancake has two nominally straight sections (section i and section ii) and two semi-circular ends (section iii, iv and section v, vi), as per design. However, the ends of the manufactured coils are not semi-circular; they are more like ellipses due to the coil deformation. By using the mean length of the straight sections, L (2178.0 mm, see Appendix B), new origins were defined as shown in Fig. 3.13, with respect to which ellipses which are defined as:

$$\frac{x^2}{a^2} + \frac{z^2}{b^2} = 1 \tag{3.43}$$

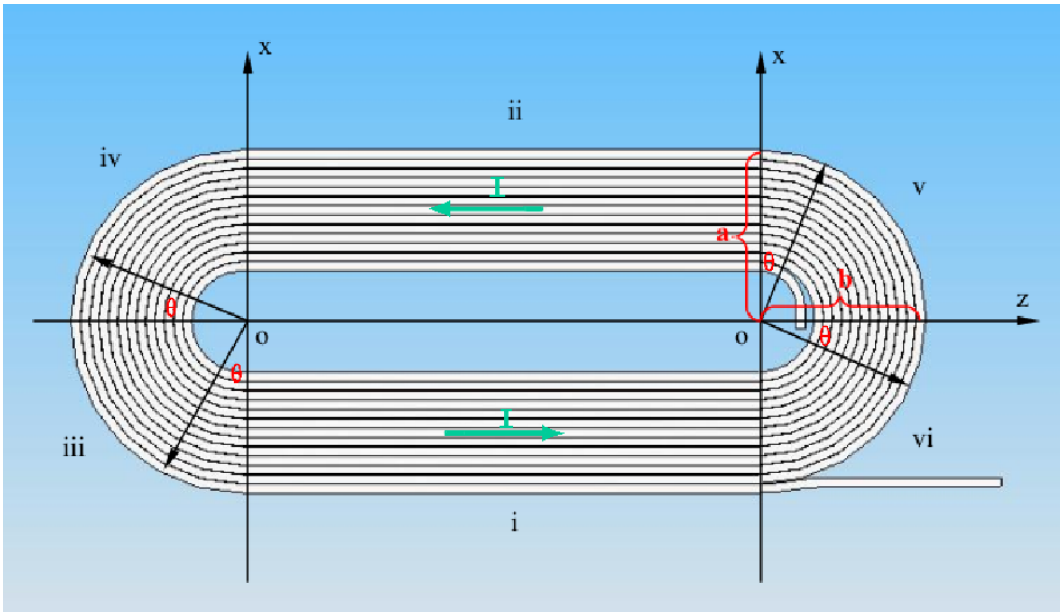

Figure 3.13: Straight and curved sections of pancakes

with intercepts a, b (a and b are generally very similar) and slope:

$$\frac{dx}{dz} = -\frac{a^2}{b^2}\frac{z}{x}\,. \tag{3.44}$$

It is convenient to use polar coordinates and employ fixed intervals $d\theta$ (θ is specified according to Fig. 3.13) for specifying the current elements. For the curved section v, making the substitutions $x = r\ \cos\theta$ and $z = r\ \sin\theta$ in equation 3.43 and taking derivatives, we have:

$$r = \Big(\frac{\cos^2\theta}{a^2} + \frac{\sin^2\theta}{b^2}\Big)^{-\frac{1}{2}}, \tag{3.45}$$

$$dr = r^3 \sin\theta\cos\theta\Big[\frac{1}{a^2} - \frac{1}{b^2}\Big]d\theta. \tag{3.46}$$

The differential arc length is (see Fig. 3.14):

$$ds = \sqrt{(r\,d\theta)^2 + (dr)^2}\,. \tag{3.47}$$

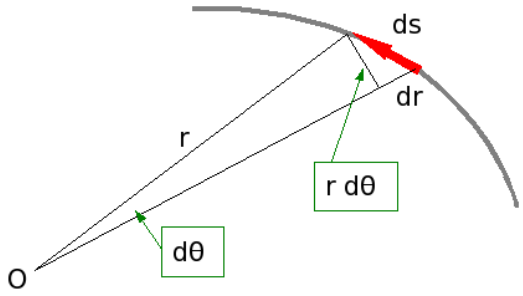

Figure 3.14: Differential arc length in the curved sections of pancakes

Because the average radius $\bar{r}$ for each curved section is approximately $\sqrt{ab}$, total arc length $S \sim 2\pi\bar{r}/4 = \frac{\pi}{2}\sqrt{ab}$. We divide S into $\sim$ 2 cm lengths, then $\delta\theta(\text{rad}) = \pi/S$ with S measured in cm [2]. Using θ as independent variable and defining $\delta\theta$ as steps with starting point at $\theta = \frac{1}{2}\delta\theta$, i.e., the middle of the first segment, we can solve for r, dr and ds from equations 3.45~3.47, then solve for components of dr and ds to obtain the coordinates and components of differential length vectors for the current elements. For example, for the current elements in section v, we have:

$$\theta = \frac{\delta\theta}{2} + \sum \delta\theta, \tag{3.48}$$

position coordinates:

$$z = r\ \sin\theta \tag{3.49}$$

$$x = r\ \cos\theta, \tag{3.50}$$

and components of differential length vector (normalized to ds):

$$ds_z = -\ \sin\theta \tag{3.51}$$

$$ds_x = \ \cos\theta. \tag{3.52}$$

[2]The differential arc length is $\sim$ 2 cm, so $\delta\theta = 2/\bar{r}$. From $S \sim 2\pi\bar{r}/4 = \pi\bar{r}/2$, we obtain $\delta\theta = 2/\bar{r} = 2/(2S/\pi) = \pi/S$.

The final coordinates for these current elements, with respect to the original TOROID frame, are obtained by the simple transformation:

$$z = r \sin\theta + \frac{1}{2} L\,, \tag{3.53}$$

$$x = r \cos\theta + R\,, \tag{3.54}$$

where L is the mean length of the straight section, R is the distance from coil center to beam line (nominal 91.44 cm). A similar procedure was also applied to the curved sections iii, iv and vi.

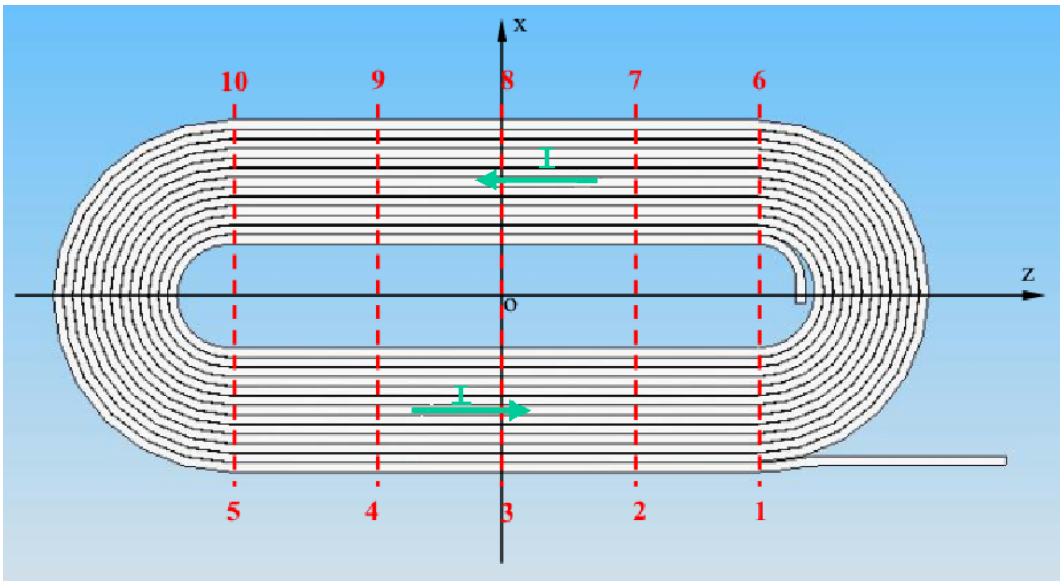

Figure 3.15: Intervals of pancake straight sections

The straight sections i and ii were not perfectly straight, but suffered some distortion during manufacture. According to the positions where the dimension measurements were made, we divide each straight section into 4 shorter straight sections, namely, interval 1-2, interval 2-3, $\cdots$, interval 9-10 (see Fig. 3.15 for reference). Since the coordinates of the upper and lower end points for the intervals, i.e., (x_L, z_L) and (x_U, z_U), are easy to obtain from the direct measurements, we can approximate an interval between a lower end point and an upper end point as a short straight line:

$$x = x_L + \frac{x_U - x_L}{z_U - z_L}(z - z_L) \tag{3.55}$$

with length:

$$S = \left[(z_U - z_L)^2 + (x_U - x_L)^2\right]^{\frac{1}{2}} \tag{3.56}$$

and slope:

$$\tan\theta = \frac{x_U - x_L}{z_U - z_L}, \tag{3.57}$$

where θ is the angle between the straight line and the Z-axis. If we divide S into $\sim$ 2 cm lengths (δS), then the position coordinates and components of differential length vectors for each current element in the straight sections can easily be calculated.

The above discussion outlined the mathematical representation of the general shape of the real physical coils. For the pancake quarter turns where the inter-pancake connections are made, and for the inter-pancake connections themselves and the external current leads and jumpers, we can use similar methods by dividing them into small arcs and straight intervals, and then find the position coordinates and components of differential length vectors for each current element.

The realistic model of QTOR can be conveniently visualized by plotting the locations of current elements[3]. We use colored dots to indicate the positions of current elements, and so these dots form an array that looks like an image of the QTOR. Fig. 3.16 shows such a "dot-matrix" representation for the QTOR, including the external current leads, jumpers, and so on, and Fig. 3.17 shows the "dot-matrix" representation for a coil, where a single dot indicates the approximate position of 5 current elements in order to make the image more clear. The "dot-matrix" representation in Fig. 3.18 indicates the positions and shapes of the current leads, jumpers and connection bars.

3.2.4 Correction for Thermal Effects

The high currents in the resistive coils of the QTOR can cause a temperature increase of the coils, although most of the Joule heating is carried away by the cooling water. The increased temperature

[3]The total number of current elements in the realistic model of QTOR is 3.2×10^5.

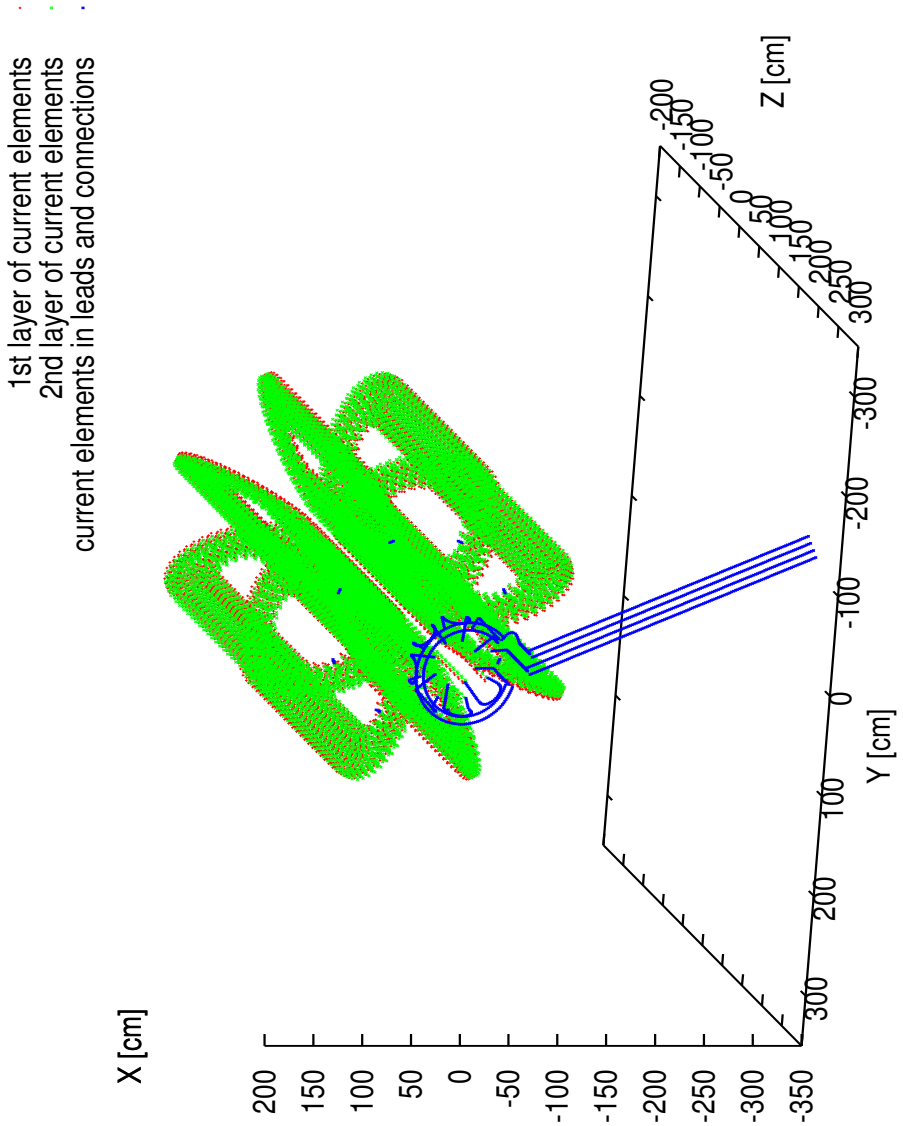

Figure 3.16: Dot-matrix representation of the QTOR by current elements used in the simulation. The first layer current elements in pancakes are marked by red dots; the second layer current elements in pancakes are marked by green dots; leads and connections are marked by blue dots.

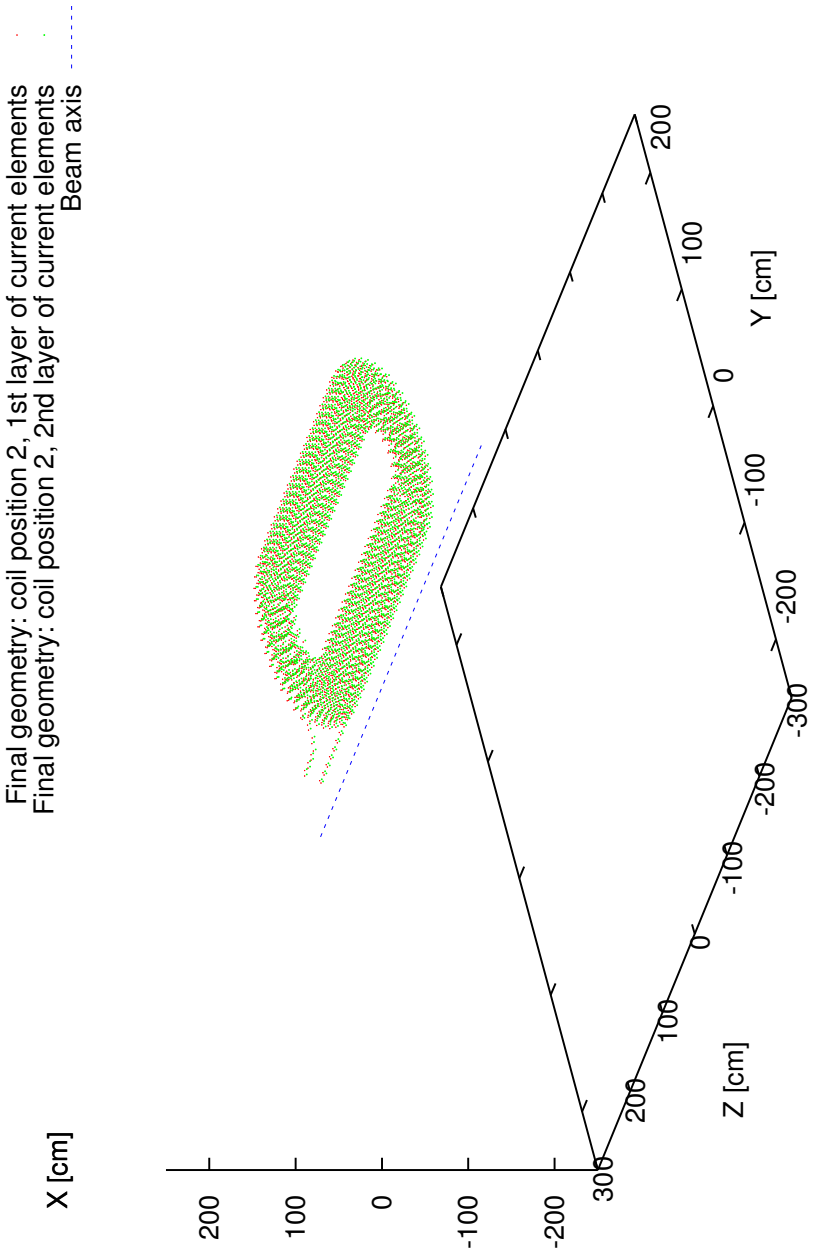

Figure 3.17: The geometry of Coil No. 3 placed at coil position 2 (lab frame) described by a dot-matrix representation of current elements used in the simulation. The first layer current elements in pancakes are marked by red dots; the second layer current elements in pancakes are marked by green dots. The beam axis is indicated by a blue dashed line.

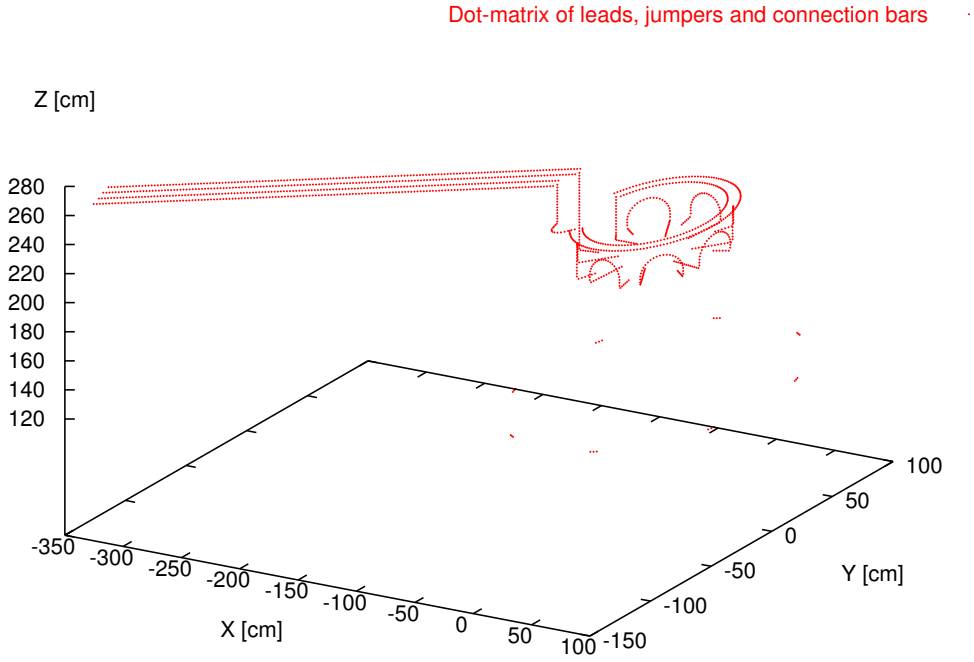

Figure 3.18: Dot-matrix representation of incoming/outgoing leads, inter-pancake connections and inter-coil connections (jumpers) by current elements used in the simulation (corresponding to the blue dots in Fig. 3.16)

will cause thermal expansion of the coils, which in turn will cause changes of the positions and lengths of the current elements. Since the positions and lengths of current elements are directly related to the calculation of the magnetic field, the effects of temperature changes must be taken into account[4].

In order to correct for the effect of a temperature increase, a factor "$SCALE$" is defined, by which all linear dimensions are scaled to take account of the thermal expansion due to the temperature increase:

$$SCALE = 1 + \alpha(T - T_0) \tag{3.58}$$

where α is the linear expansion coefficient of the conductor material. The basic linear dimensions, such as the radius of the current center of the first turn, the spacing between turns, the radial displacement of a segment, the lengths of the straight sections, and so on, have been defined at temperature T_0. At temperature T, we scale these basic dimensions by multiplying them by $SCALE$ to deduce the new basic dimensions, which set the length scale for finding all other dimensions and positions of current elements at temperature T. Note that the coils are constrained in their mounting frames, and therefore the measurement reference points should be the constrained points of coils, which must be specified before the above information can be used in calculating the corrected coordinate positions for the current elements[5].

3.3 Simulation Programs

The simulation programs for the QTOR are written in the FORTRAN programming language and structured into several functional modules:

- main.f: the main routine that provides options for different calculating tasks,

[4]The effect of temperature gradient in shifting the centroid of current element is not considered since the average effect cancels out.

[5]Nominally, the coils are constrained at the upstream end and at the outer radius. Thus the effect of temperature expansion is to shift the coil center to: $x'_{center} = x_{center} - \frac{W}{2}\,\alpha\,(T - T_0)$, $z'_{center} = z_{center} + (\frac{W}{2} + \frac{L}{2})\,\alpha\,(T - T_0)$, and to expand the straight section lengths of the coils to $L' = L \cdot SCALE$, where W is the width of a coil, and L is the straight section length of a coil (at temperature T_0).

- coil_data.f: for organizing all the coil data from the manufacturer's control report and inspections,
- coil0.f: for calculating the positions and the differential length vectors of all the current elements of a coil when it is initially placed on the X-Z plane,
- coils.f: for calculating the positions and the differential length vectors of all the current elements of the eight coils following rotation from the initial X-Z plane to their final positions,
- connections.f: for calculating the positions and the differential length vectors of all the current elements of the inter-pancake connections, inter-coil connections and current leads,
- mag_master.f: for setting up the geometry of the QTOR by calling the routines, such as coil0.f, coils.f, and so on, and controlling the direction of the program flow through reading in parameters from input files,
- field.f: for calculating the magnetic field for the QTOR at a single field point,
- scan.f: for calculating the magnetic field components at a number of points along a scan line, and locating the zero-crossing points,
- interp.f: for interpolating the zero-crossing point of a field component and calculating the fields and field gradients at that point,
- traj.f: for tracing electron trajectories through the magnetic field.

The inputs for the simulation programs include coil data and control parameters. The coil data are extracted from the manufacturer's control reports and an on-site inspection. The control parameters are data, such as the value of temperature, value of current, coil displacements, and so on. The output of the simulation programs includes the field map, zero-crossing points, electron trajectories, etc, which are organized in certain formats so that they are convenient for analyzing or easy to adapt to other simulations (for instance, the GEANT simulation of the Q^p_{Weak} experiment).

3.4 Calculation Results

The magnetic field calculations were carried out using the above-discussed algorithms and programs. In the calculation, a DC current 8615.0 A at temperature 20.0 ^{o}C was assumed, and the coils were placed in the specific order of 2, 3, 4, 5, 6, 7, 8, 9 (coil 1 is spare) in the coil positions 1, 2, 3, 4, 5, 6, 7, 8, respectively (see Fig. 3.19 for reference, where the coil positions are indicated using the sandwiched red and green dots. The incoming and outgoing current leads and jumpers are also indicated in the dot-matrix figure using the blue dots). The distance from the coil center to the beam axis was set at 91.44 cm (nominal value), for each coil. Note that the grid field points that are too close to the coils will lead to erroneous values of the magnetic field (see section 3.5). Thus the following exclusion zones (where magnetic field calculations are not reliable) should be observed:

- $-186 < z < 186$ cm and $16 < R < 21$ cm: no reliable values,
- $-186 < z < 186$ cm and $21 < R < 170$ cm: exclude regions where $R < 8/\sin\phi$ (ϕ measured from plane of coil).

3.4.1 General Behavior of the Magnetic Field

The following are some examples to illustrate the calculated results. Fig. 3.21 – Fig. 3.26 show the general shapes of the QTOR magnetic field, where Fig. 3.21 – Fig. 3.23 show the field shapes in sector 1 for $\phi = 0^{o}$, $0 \le R \le 250$ cm, $-250 \le z \le 250$ cm[6]; Fig. 3.24 – Fig. 3.26 show the shapes of the field components on an upstream $z = -190$ cm plane in sector 1 over $-15^{o} \le \phi \le 15^{o}$, $0 \le R \le 250$ cm, $z = -190.0$ cm (refer to Fig. 3.20 for the position of $Z = -190$ cm plane, and Fig. 3.11 for the definition of the azimuthal angle ϕ).

The field component of greatest interest is the azimuthal field component B_{ϕ}, since it is perpendicular to the momenta of scattered electrons, and causes the deflection of those electrons, resulting in their focusing onto the quartz detector bars. With increasing radial distance R, B_{ϕ} increases

[6] (R, ϕ, z) are the cylindrical coordinates of the lab frame, where z is along the beam line with zero at the center of the QTOR; R is the radial distance from the Z-axis (beam axis); ϕ is the azimuthal angle starting from the X-axis (vertical-up).

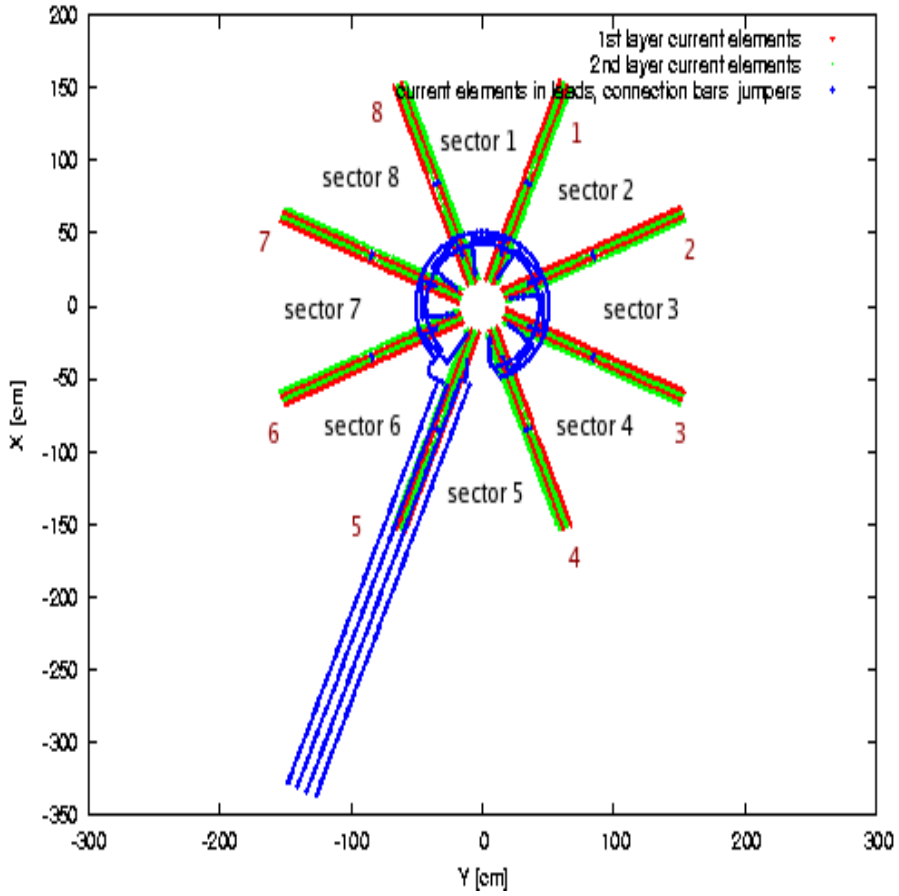

Figure 3.19: The order of coils (looking downstream) displayed in a dot-matrix format (blue dots indicate the current element positions in the current leads and jumpers). The coil 2 is placed at coil position 1 (22.5^{o} from the vertical X-axis). The coil 3 is placed at coil position 2 (67.5^{o} from the vertical X-axis), and so forth. The sector numbers are arranged clockwise. The sector 1 is in between coil position 8 and 1, the sector 2 is in between coil position 1 and 2, and so on.

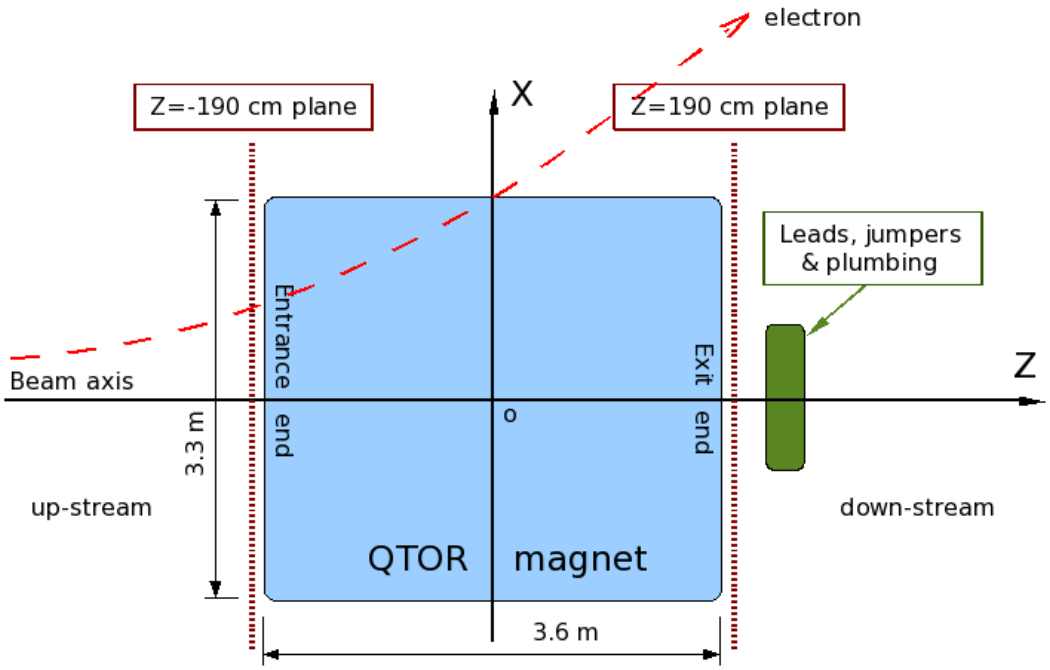

Figure 3.20: A "cut-view" of the QTOR along the X-Z plane

rapidly from zero at the beam line to its maximum value ($\lesssim$ 4800 Gauss) at $R \sim 60$ cm, and then drops off approximately as $1/R$ (refer to Fig. 2.5). For an ideal toroidal magnet, the radial component B_r and the z-component B_z are zero. The calculation based on the realistic model of the QTOR gives non-zero values for B_r and B_z at $\phi = 0$, especially near the leads at the downstream areas. At the upstream entrance end, this is due to the fact that coils are not identical. At the downstream exit end, the major reason for these non-ideal features is that the current leads, inter-pancake connection bars and inter-coil connection jumpers influence the magnetic field. The maximum values of the magnetic field for these abnormal field regions are less than several hundred Gauss compared to the main B_ϕ field of $\sim$ 5000 Gauss, and these regions are far away from the envelopes of the elastic electron trajectories, so their influences can be neglected. In other regions, B_r and B_z are negligibly small compared to the B_ϕ component.

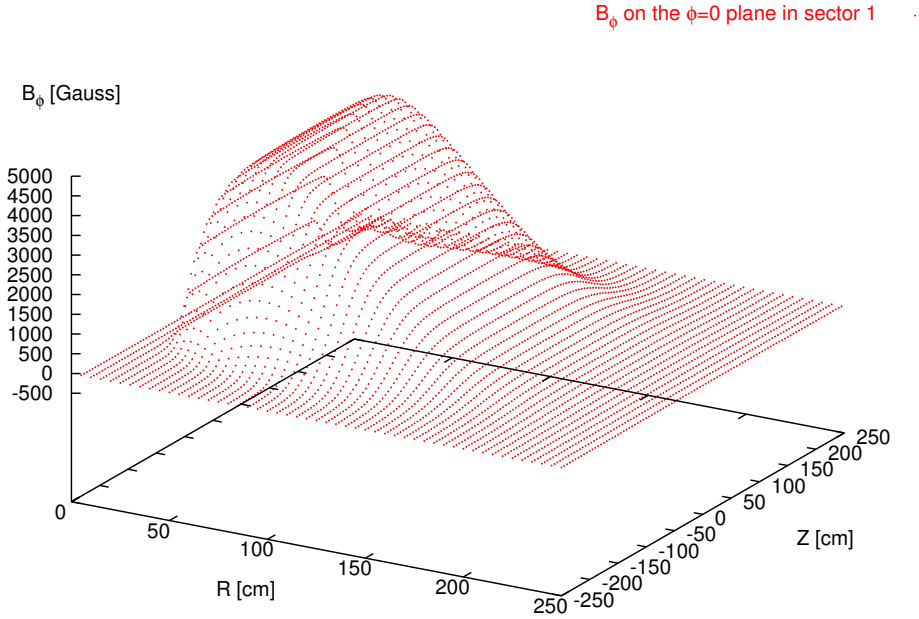

Figure 3.21: B_ϕ on the $\phi = 0$ plane in sector 1

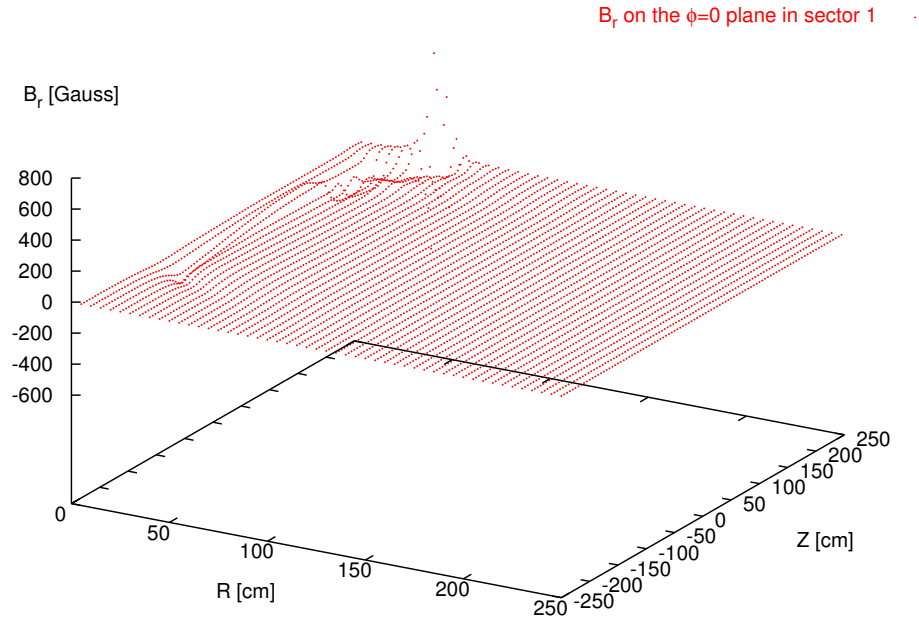

Figure 3.22: B_r on the $\phi = 0$ plane in sector 1

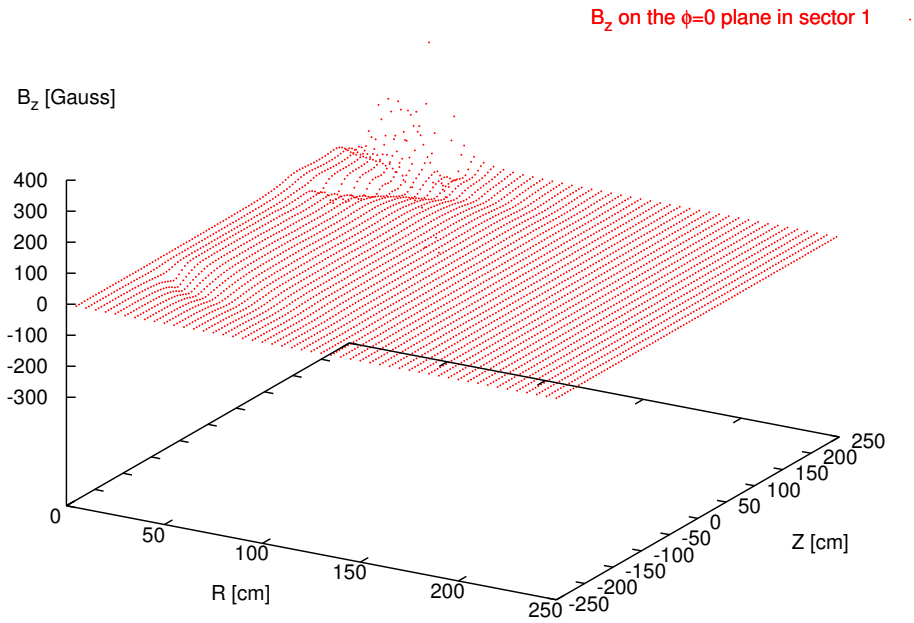

Figure 3.23: B_z on the $\phi = 0$ plane in sector 1

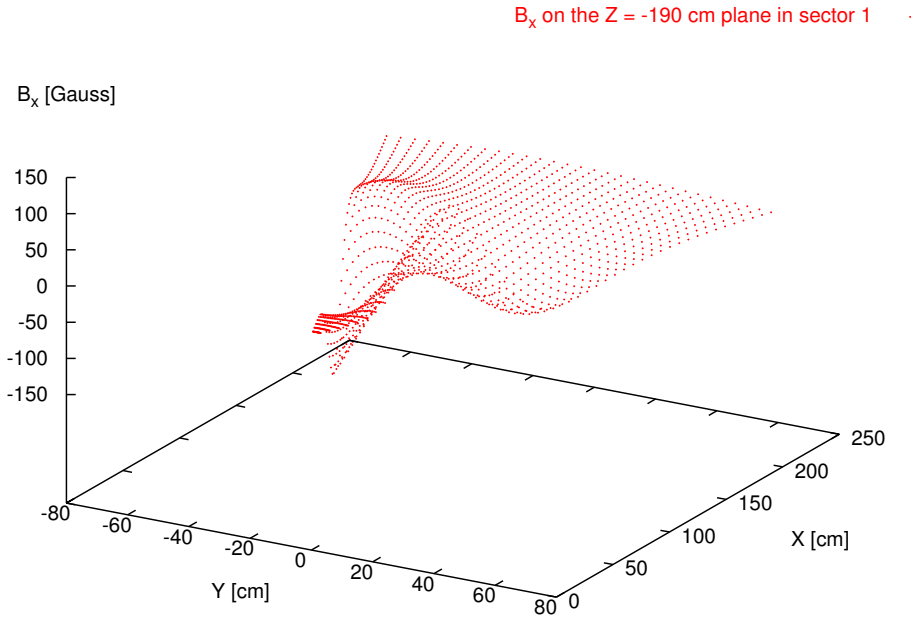

Figure 3.24: B_x on an upstream $z = -190$ cm plane in sector 1

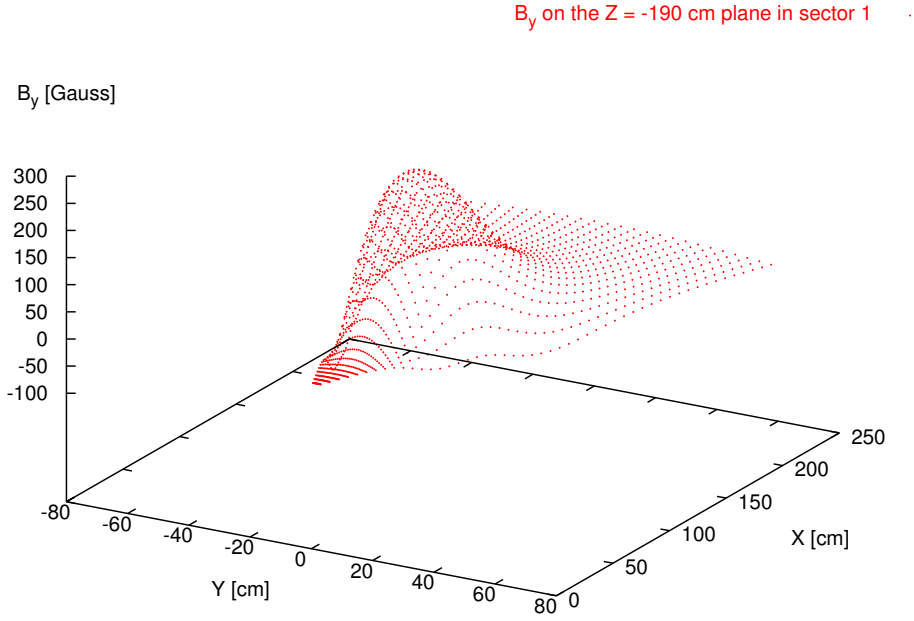

Figure 3.25: B_y on an upstream $z = -190$ cm plane in sector 1

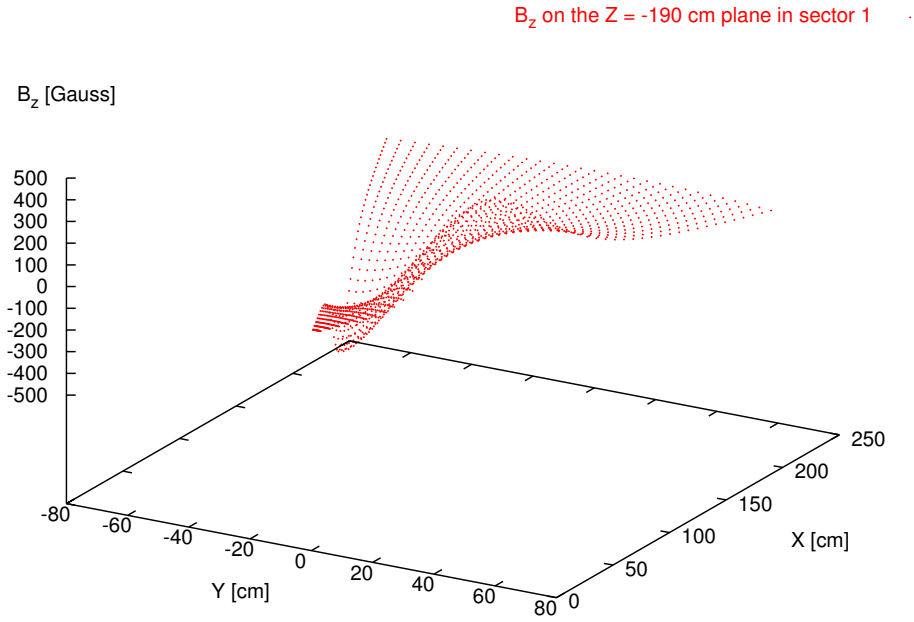

Figure 3.26: B_z on an upstream $z = -190$ cm plane in sector 1

3.4.2 Zero-Crossing Points

The shapes of the field components in the upstream fringe-field regions are shown in Fig. 3.24 – Fig. 3.26, from which we can see that the B_x, B_y and B_z components of the magnetic field on a plane that is perpendicular to the beam axis and near the end of the magnet may have either positive or negative values. Therefore, there are some field points in the region that have zero field values. These points are characteristic points for the magnetic field of QTOR, which we refer to as "zero-crossing" points. The locations of the zero-crossing points are very sensitive to the coil displacements. If the displacements of the zero-crossing points from their nominal positions are determined experimentally, the actual coil displacements then can be deduced (this technique will be discussed in detail in chapter 5).

The zero-crossing points can be located in the simulation programs by performing field scans along pre-defined paths. Fig. 3.27, Fig 3.29 and Fig. 3.31 show the positive and negative magnetic field regions outside QTOR magnet on $z = -190$ cm upstream plane in sector 1 ($-15^{\rm o} \leq \phi \leq 15^{\rm o}$). The zero-crossing points are located at the boundaries between the positive field regions (red crosses) and negative field regions (green dots). Fig. 3.28, Fig. 3.30 and Fig. 3.32 show the zero-crossing points for B_x, B_y and B_z components of sector 1 found by the simulation programs.

3.4.3 Field Symmetry

The calculated results show that the magnetic field of QTOR has a high degree of symmetry as expected, although there are small field variations from sector to sector. For example, through comparing the total magnetic field for sector 1 and sector 5 (see Fig. 3.33, where -250 cm $\leq z \leq 250$ cm, $\phi_{sector1} = 3.5^{\rm o}$, $\phi_{sector5} = 183.5^{\rm o}$ and $0 \leq R \leq 250$ cm), we learn that the field differences between these two sectors are acceptably small. The maximum value of the field difference is less than 15 Gauss near the beam line area. The field symmetry is also demonstrated by its effect on scattered electron trajectories in the following section.

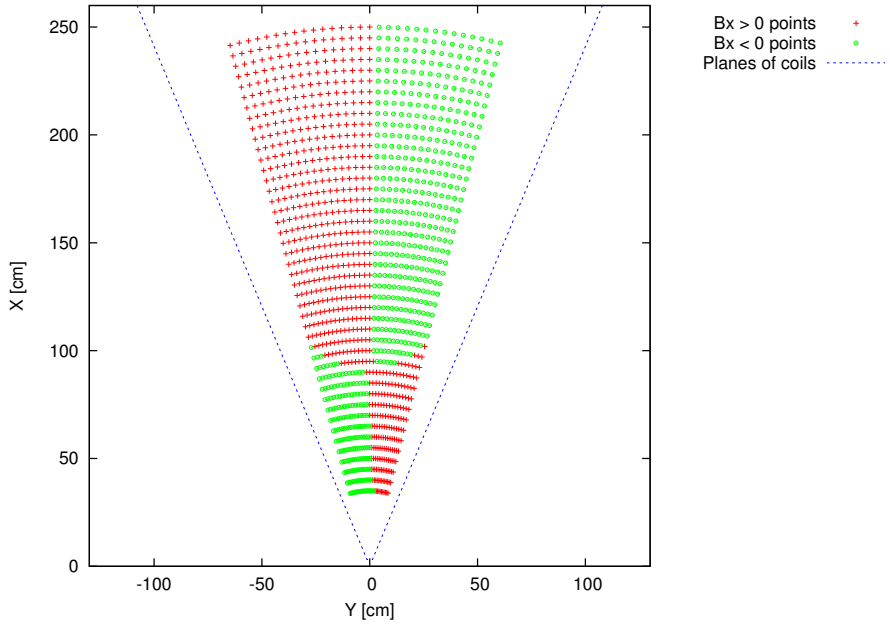

Figure 3.27: Positive and negative B_x regions (indicated by red crosses and green dots, respectively) on an upstream $z = -190$ cm plane in sector 1

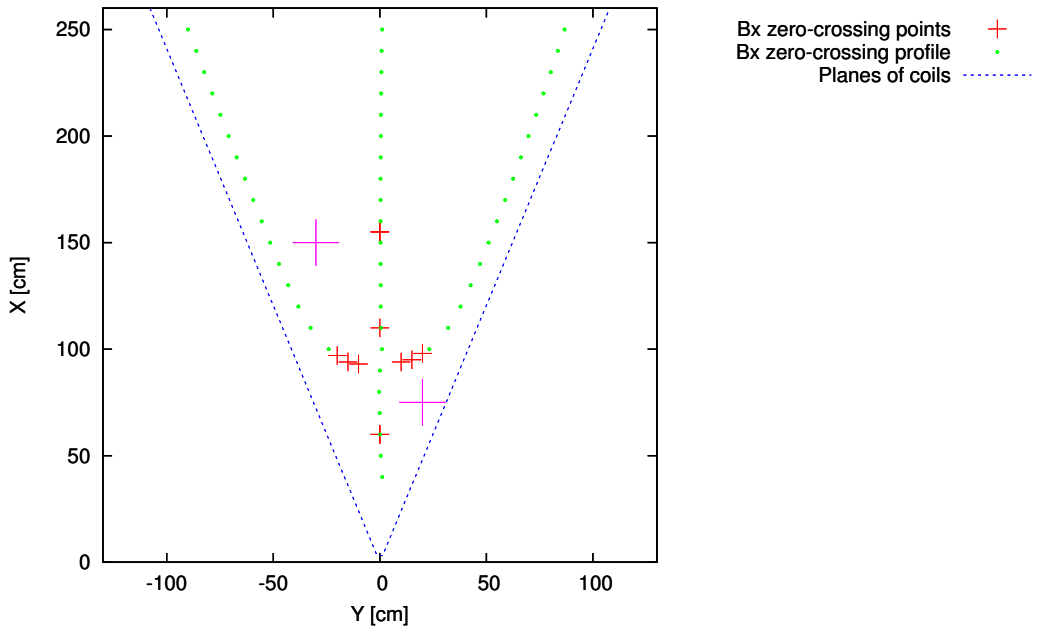

Figure 3.28: Zero-crossing points for B_x components on an upstream $z = -190$ cm plane in sector 1. The green dots define the boundaries between the positive and negative field regions; the red crosses indicate the zero-crossing positions found by the simulation programs; the positive field regions are indicated by the large pink plus sign.

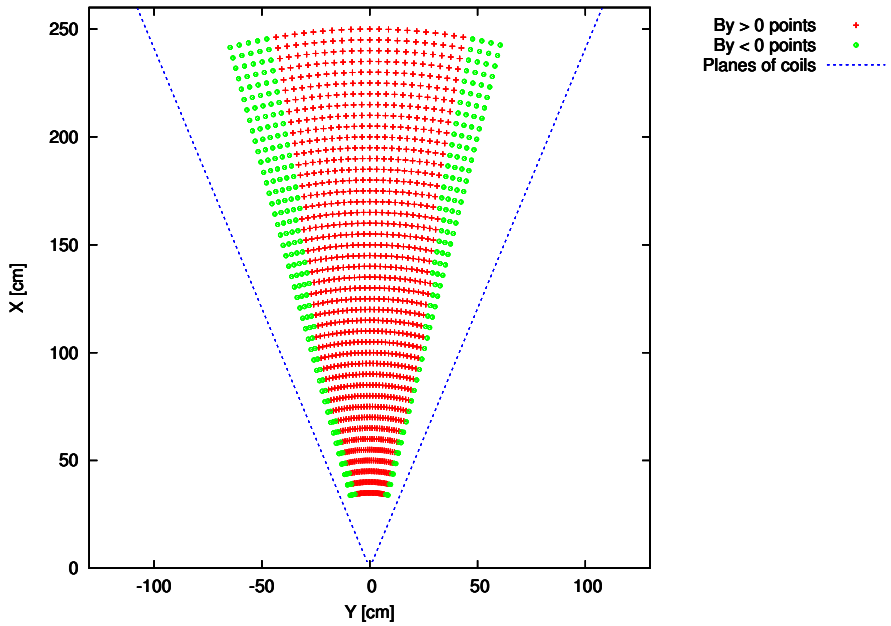

Figure 3.29: Positive and negative B_y regions (indicated by red crosses and green dots, respectively) on an upstream $z = -190$ cm plane in sector 1

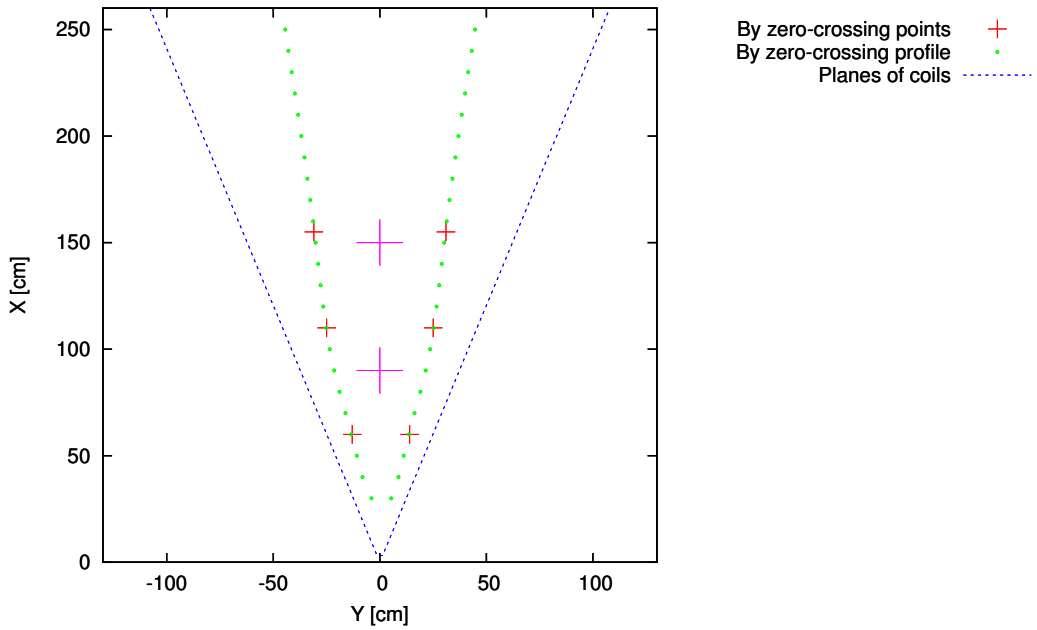

Figure 3.30: Zero-crossing points for B_y components on an upstream $z = -190$ cm plane in sector 1. The green dots define the boundaries between the positive and negative field regions; the red crosses indicate the zero-crossing positions found by the simulation programs; the positive field regions are indicated by the large pink plus sign.

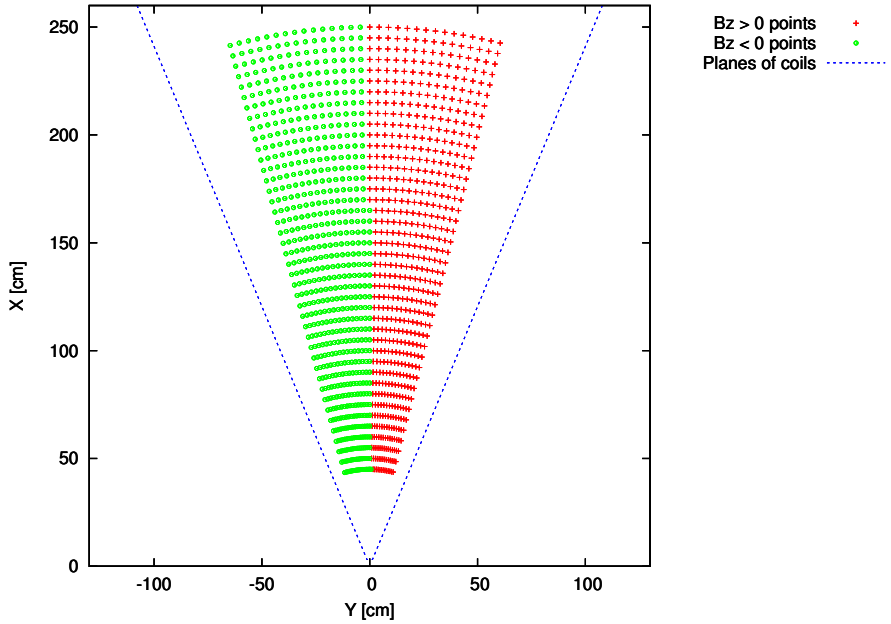

Figure 3.31: Positive and negative B_z regions (indicated by red crosses and green dots, respectively) on an upstream $z = -190$ cm plane in sector 1

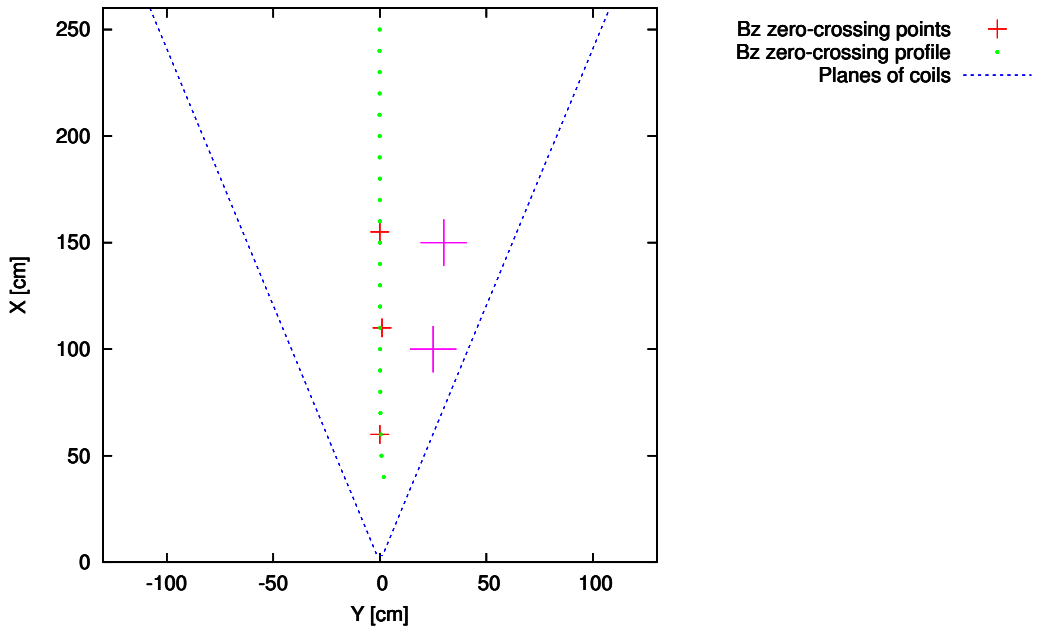

Figure 3.32: Zero-crossing points for B_z components on an upstream $z = -190$ cm plane in sector 1. The green dots define the boundaries between the positive and negative field regions; the red crosses indicate the zero-crossing positions found by the simulation programs; the positive field regions are indicated by the large pink plus sign.

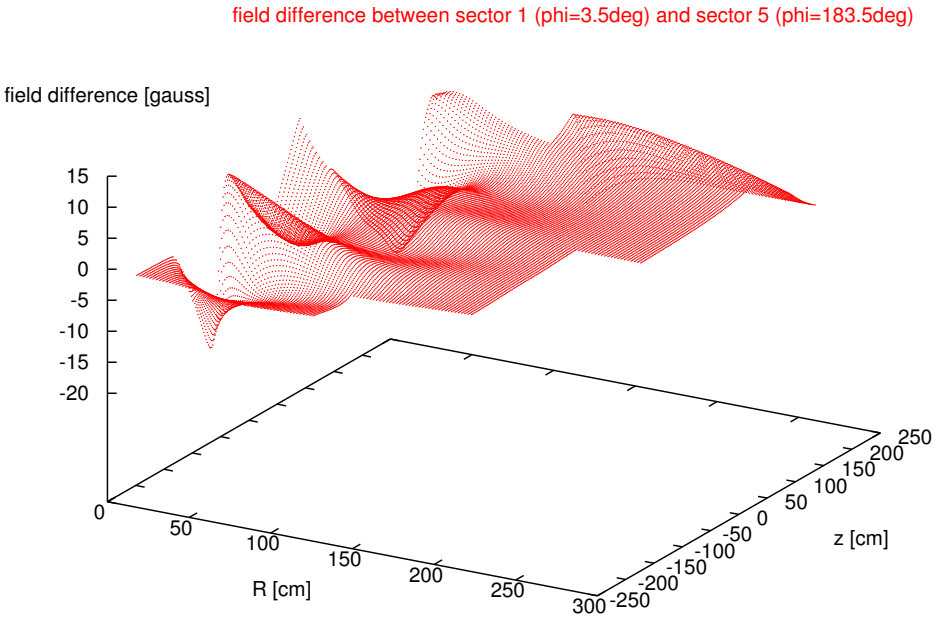

Figure 3.33: Field difference between sector 1 and sector 5

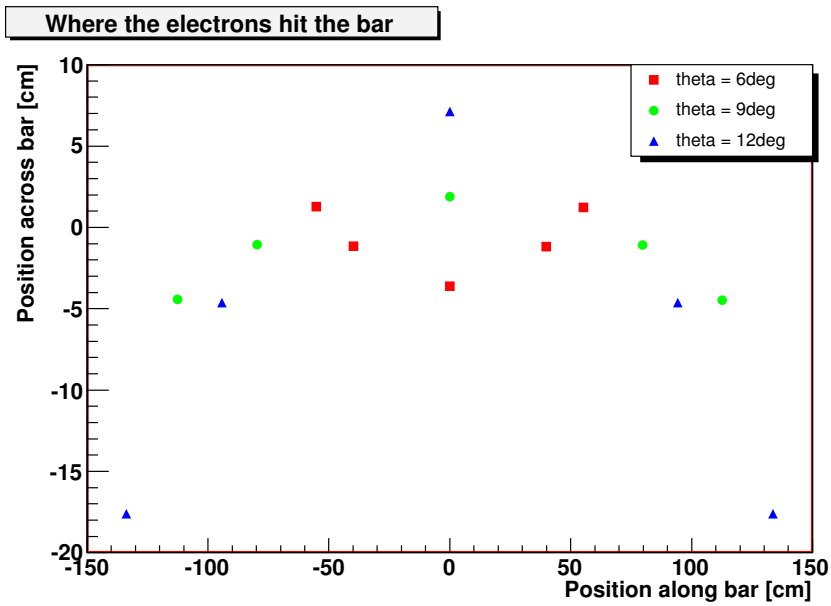

Figure 3.34: Averaged electron trajectory positions for the eight sectors on the detector bars. The x and y coordinates are measured transverse and along the detector bars for each sector, respectively, from the center of the bar.

3.4.4 The Scattered Electron Trajectories

Tracing the scattered electron trajectories is a convenient and direct tool for illustrating the magnetic field properties and testing the field calculations. For this purpose, we set the conditions that the center of target is at $z = -650.0$ cm, the incident electron energy is 1.165 GeV, the center of each detector bar is at $z = 580$ cm with a 325 cm distance to beam line and the normal to the surface of the detector bars makes an angle of 19^o with respect to the Z-axis. A family of electron trajectories was generated for passing through each sector of the magnetic field, with $\theta = 6^o,\ 9^o,\ 12^o$ and $\phi = 0,\ \pm 10^o,\ \pm 14^o$. The scattering angle θ and the azimuthal angle ϕ_{sector} are specified at the nominal target position, and the azimuthal angles defined in each sector start from the mid-plane that bisects that sector[7]. These electron trajectories are traced, and the positions where the trajectories intersect detector bars are recorded. The averaged positions where the electrons hit the Cerenkov detector bars are plotted in Fig. 3.34, where the horizontal axis corresponds to ϕ at the target, and the vertical axis corresponds to θ at the target, respectively. The standard deviations of each of these points, arising from the sector to sector variations, are about $\sigma_x = 0.05$ cm and $\sigma_y = 0.09$ cm (these are smaller than the plotting points themselves). Note that an actual detector bar is only 200 cm long, and hence some electrons, such as those with angles $\theta = 12^o$, $\phi = \pm 14^o$ will not actually contribute to the Čerenkov detector signals.

The sampled field symmetry is checked by the scatter plots Fig. 3.35 and Fig. 3.36, where the electron intersections with angle $\theta = 6^o$, $\phi_{sector} = 0^o$ and electrons with angle $\theta = 12^o$, $\phi_{sector} = 10^o$ are shown for each sector (note the significant reduction in the range of the plots compared to Fig. 3.34).

3.4.5 Effects of the Field Mapper Misalignments

In the magnetic field mapping (to be discussed in Chapter 4), if the magnetic field mapper is not well aligned with respect to the QTOR magnet, the Hall probes may move along a plane that is not

[7]These electron scattering angles are specified for testing purposes only. Their actual range will be determined by the final collimator design.

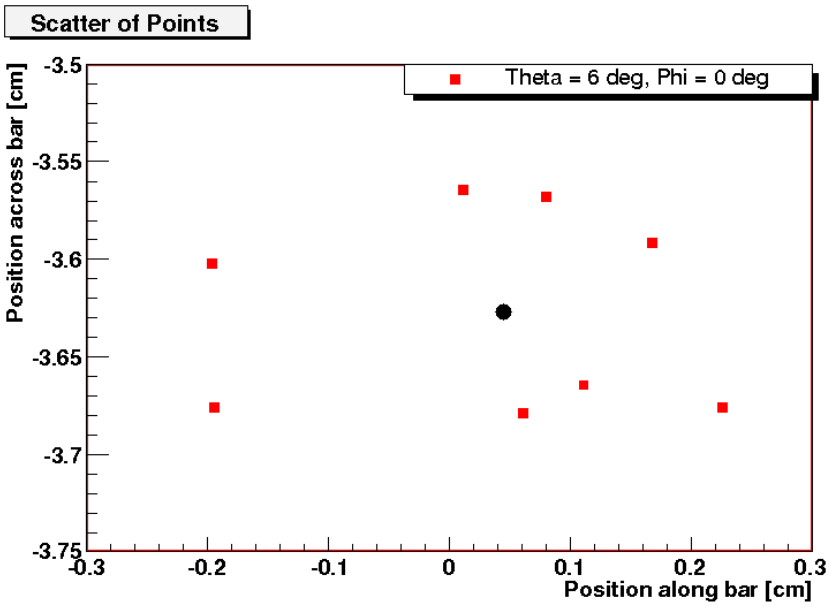

Figure 3.35: Trajectory intersections from the eight sectors with the detector bars for $\theta = 6^{o}$ and $\phi_{sector} = 0^{o}$ (the average hit position is indicated by a black round-dot)

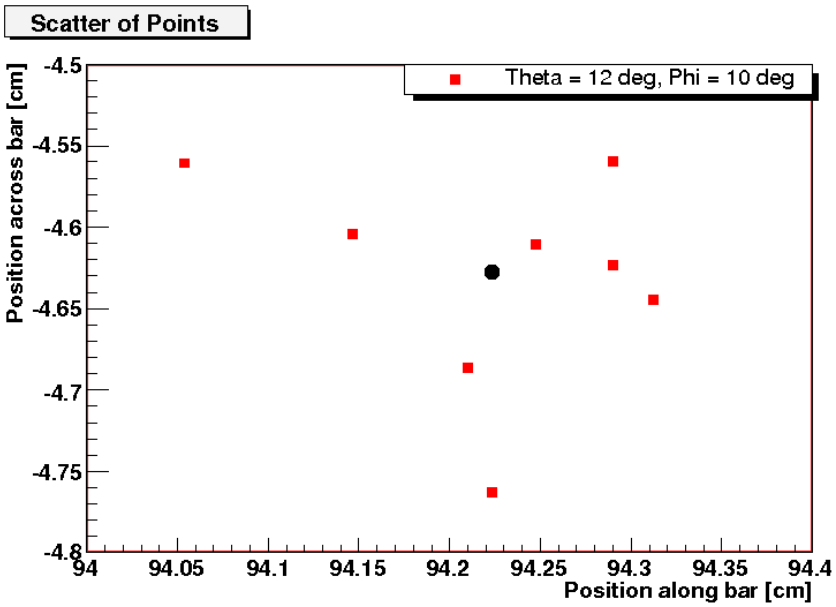

Figure 3.36: Trajectory intersections from the eight sectors with the detector bars for $\theta = 12^{o}$ and $\phi_{sector} = 10^{o}$ (the average hit position is indicated by a black round-dot)

perfectly perpendicular to the symmetry axis of the QTOR (equivalent to a rotation of the QTOR about the X-axis or Y-axis in the reference frame of the field mapper). As a result, the zero-crossing points found by the magnetic field mapper will appear at positions that are different from the predictions of the QTOR simulations. There is a similar situation in the case that the field mapper has an offset in Z direction. For these reasons, the simulation programs should have the capability to locate zero-crossing points in a selected plane so that the offsets of the QTOR magnet with respect to the field mapper along the Z axis, or rotations about the X-axis or Y-axis, can be taken into account (the offsets of the QTOR magnet with respect to the field mapper along the X or Y axes, or azimuthal rotations about the Z-axis, were considered in section 5.2.2).

An additional FORTRAN program (scan_plane.f) was developed and integrated into the QTOR simulation programs for this purpose. This program can locate the zero-crossing points in a selected plane (referred to as the "scan-plane") that is defined by the angles between the direction of its normal vector and the coordinate axes of the TOROID frame, as well as the intersecting point of the plane with the Z-axis. The parameters used to describe this plane are:

- α – angle from the normal vector to the X-axis,
- β – angle from the normal vector to the Y-axis,
- γ – angle from the normal vector to the Z-axis,
- and $(0,\ 0,\ Z_0)$ – coordinates of the intersecting point of the scan-plane with the Z-axis.

Calculations based on the "scan_plane.f" routine were performed to analyze the effects of field mapper orientation change with respect to the QTOR axes. In order to simplify the discussion of calculated results, only the positions of the $B_y = 0$ points are considered here.

We define the following scan-planes:

- scan-plane #0: $\alpha = 90^{\text{o}}$, $\beta = 90^{\text{o}}$, $\gamma = 0^{\text{o}}$, $Z_0 = -190$ cm (corresponding to the normal field mapper location, i.e., there is no field mapper misalignment with respect to the QTOR),

- scan-plane #1: $\alpha = 90^o$, $\beta = 90^o$, $\gamma = 0^o$, $Z_0 = -195$ cm (corresponding to that the field mapper has an offset in Z direction, i.e., the field mapper is shifted 5 cm along Z-axis from its normal position),

- scan-plane #2: $\alpha = 88^o$, $\beta = 90^o$, $\gamma = 2^o$, $Z_0 = -190$ cm (corresponding to that the field mapper is tilted a small angle with respect to the QTOR, i.e., the field mapper is rotated 2^o about the Y-axis from its normal orientation).

Fig. 3.37 indicates the B_y zero crossing positions at different scan-planes in sector 1 (coils are placed at their nominal locations). The distance between two B_y zero-crossing points that have same X coordinate can reflect the changes of the B_y zero-crossing positions. Table 3.3 shows some of these distances on different scan-planes. These distances are sensitive to the the field mapper misalignments. The region of greatest sensitivity is between $X \sim 30$ cm and $X \sim 130$ cm, as shown in Fig. 3.38. From these plots and the table, we see that the positions of the $B_y = 0$ points change with the scan-plane orientations and positions. However, they do not appear to change very much. For example, for the B_y zero-crossing points with $X = 100$ cm , a 5 cm shift of the field mapper along Z-axis causes a ~ 1.1 cm displacement of zero-crossing points in Y direction; a 2^o rotation of the field mapper about the Y-axis causes a ~ 0.83 cm displacement of the zero-crossing points in Y direction.

3.4.6 Effects of Coil Displacements

If coils are misaligned from their nominal locations, the zero-crossing positions will shift noticeably from their nominal values. The effects of coil displacement on the zero-crossing positions can also be investigated via the "scan_plane.f" routine, as introduced in section 3.4.5. For example, we displaced coils randomly with rms position offset $\sigma_{XYZ} = 1.0$ cm and rms angle offset $\sigma_{ANG} = 1.0^o$, and then located the zero crossing points in different scan-planes (refer to section 3.4.5 for the definition of scan-plane parameters). A calculation is shown in Table 3.4 and Fig. 3.39, where Table 3.4 lists a set of coil displacement parameters (refer to 3.2.2), and Fig. 3.39 indicates the B_y

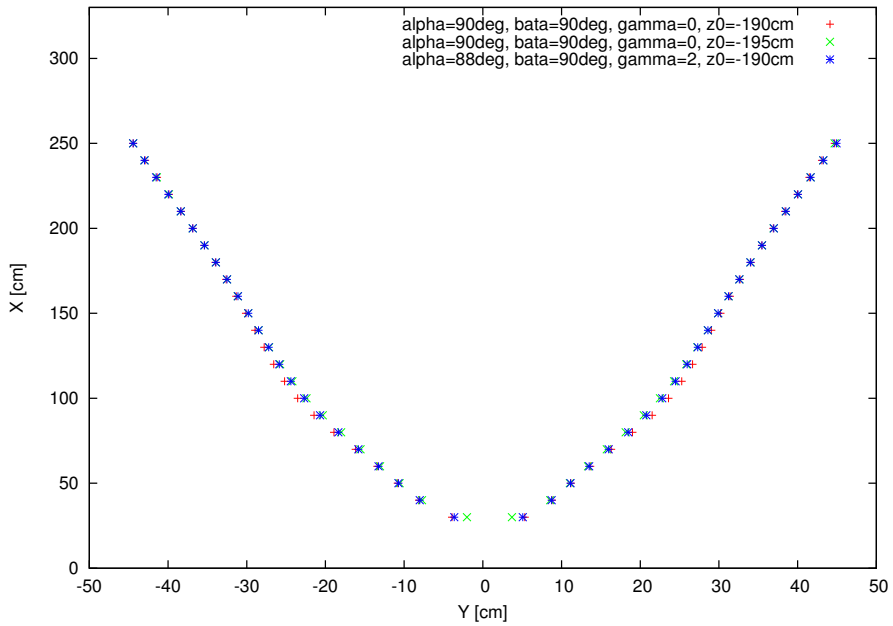

Figure 3.37: Zero-crossing positions in different scan-planes (nominal coil placement)

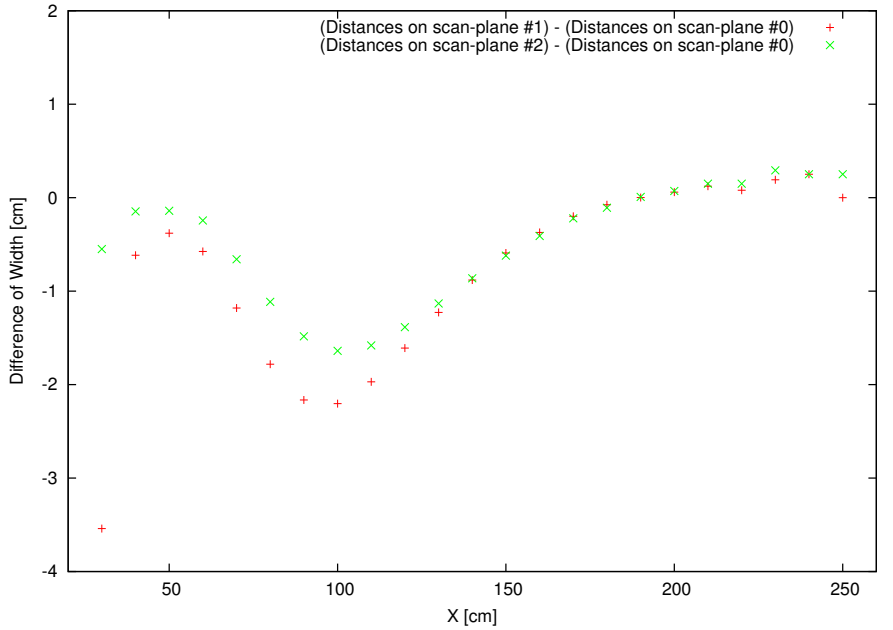

Figure 3.38: Variation of the distances between $B_y = 0$ points with scan planes

X coordinate (sector frame)	scan-plane # 0 $\alpha = 90^o$ $\beta = 90^o$ $\gamma = 0^o$ $Z_0 = -190$ cm	scan-plane # 1 $\alpha = 90^o$ $\beta = 90^o$ $\gamma = 0^o$ $Z_0 = -195$ cm	scan-plane # 2 $\alpha = 88^o$ $\beta = 90^o$ $\gamma = 2^o$ $Z_0 = -190$ cm
30	9.250	5.709	8.700
40	16.907	16.291	16.760
50	22.006	21.626	21.866
60	27.006	26.430	26.762
70	32.466	31.285	31.807
80	37.944	36.162	36.830
90	42.951	40.786	41.467
100	47.121	44.918	45.482
110	50.465	48.495	48.884
120	53.219	51.610	51.833
130	55.651	54.423	54.519
140	57.967	57.085	57.104
150	60.307	59.715	59.687
160	62.744	62.372	62.334
170	65.305	65.106	65.084
180	68.013	67.937	67.905
190	70.837	70.839	70.845
200	73.762	73.821	73.834
210	76.750	76.872	76.900
220	79.850	79.929	80.000
230	82.875	83.067	83.167
240	86.000	86.250	86.250
250	89.125	89.125	89.375

Table 3.3: Distances between $B_y = 0$ points in sector 1 (in units of cm)

zero-crossing positions for different scan-planes in sector 1. From Fig. 3.39, we can see that the zero-crossing positions are very sensitive to the coil locations. This is the basis of our selection of the zero-crossing analysis technique to infer the actual coil locations in the QTOR.

Coil Position	Coil #	dX [cm]	θ_x [deg]	dY [cm]	θ_y [deg]	dZ [cm]	θ_z [deg]
1	2	0.945	-1.389	1.019	-0.075	1.349	0.805
2	3	1.218	0.631	-0.072	0.069	-0.991	-1.858
3	4	-0.431	0.224	1.930	1.160	0.582	-0.891
4	5	-0.002	0.728	0.138	0.656	0.642	0.408
5	6	-0.767	0.024	0.072	-0.407	-1.245	0.336
6	7	-0.734	-0.547	1.223	1.217	0.095	-2.290
7	8	-0.896	1.400	1.746	1.124	-0.780	-1.331
8	9	-0.179	1.116	-0.770	-2.267	1.642	-0.453

Table 3.4: Coil displacement parameters

3.5 Accuracy of Approximations in the Magnetic Field Calculations

Many approximations are involved in the magnetic field simulation programs of QTOR. In order to assess the accuracy of the simulation results, we performed some extra calculations to evaluate these approximations from the following points of view:

- assessment of the validity of approximations,
- uncertainties of the magnetic field calculation,
- and uncertainties in positions of zero-crossing points.

The details of these evaluations are discussed below.

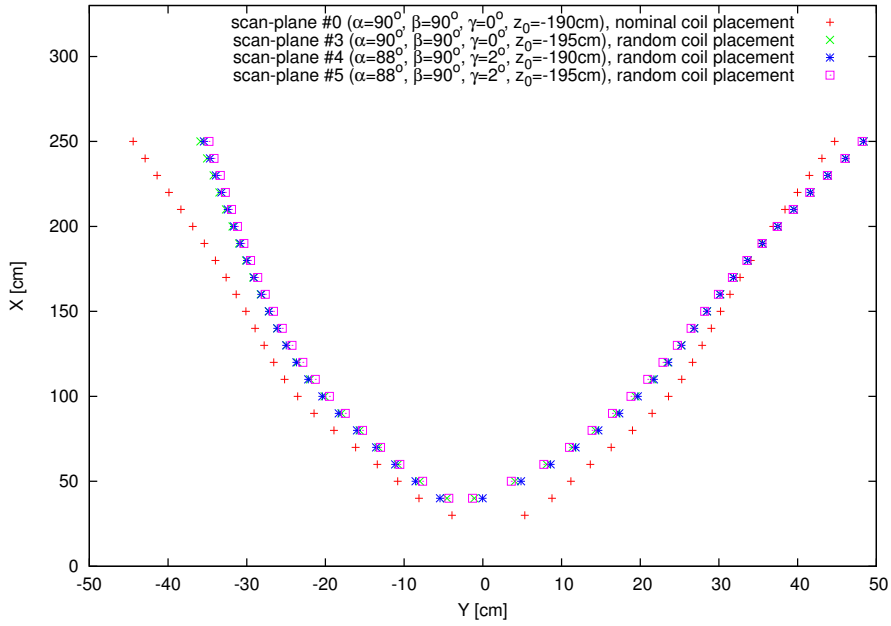

Figure 3.39: B_y zero-crossing positions (random coil placement), which depend on the coil placements, and vary with the QTOR misalignments.

3.5.1 Assessment of the Validity of Approximations

The major approximation in the QTOR field simulation is to divide the conductor into many small elements, and then treat each element of the conductor as a current element. Since we calculate the magnetic field by performing a numerical integration over the current elements, the smaller the dimensions of the current elements, the greater the accuracy that can be achieved[8]. However, if the conductor is divided into much smaller sized pieces, there will be many more current elements in total. Thus, the magnetic field calculation will require more computing time due to the increased number of current elements. On a PBS (Portable Batch System) cluster of eight 1.6 GHz CPU computers, the typical computing time for generating a field map of eight sectors[9] is about a week if the conductor is divided into many bars of $\sim$ 2 cm length, and the cross-section is further divided into four segments (see Fig. 3.4 for reference). Considering both the accuracy and computing time,

[8]Double precision is used in all simulation programs in order that the round-off errors are minimized. The machine precision for the simulation is 2.22×10^{-16} for double precision data.

[9]The grid size is ΔR = 2 cm, ΔZ = 2 cm, $\Delta\phi = 1^{\circ}$.

the balanced choice in the simulation is to find appropriate (as small as practical) dimensions for the current elements, which correspond to a reasonable computing time.

When the dimensions of the current elements are defined, the effect of the finite element size on the calculated field values needs to be assessed. The following procedure was adopted for this assessment:

- Firstly, we isolate a piece of 2 cm length of conductor (referred to as "conductor element"), and define a coordinate system as shown in Fig. 3.40.

- Then, we divide this conductor element into 4 sub-conductors, and calculate the magnetic field $\mathbf{B}_L$ at a selected point (x, y, z) by treating each sub-conductor as a segment current element (referred to as "large current element"; this is actually the same approximation we have adopted in the QTOR simulation program).

- Next, we re-divide the original conductor element into 20 layers along the Z-axis, and each layer of conductor is further divided into about 200×200 tiny pieces (in the X-Y plane) according to conductor's geometry (there are $\sim 7 \times 10^5$ sub-conductors in total in this 2 cm length of conductor). We treat each of the sub-conductors as a current element (referred to as "small current element", the dot-matrix representation in Fig. 3.41 describes the geometry of the conductor cross-section, and shows the positions of the small current elements on the X-Y plane), and then calculate their magnetic field $\mathbf{B}_S$ at the same field point (x, y, z). Since the small current elements are very tiny, they represent the current density distribution more accurately than the large current element. Therefore, the calculated value of $\mathbf{B}_S$ can be treated as the "true" value of the magnetic field at point $(x,\ y,\ z)$.

- Finally, for each grid point in the space around the conductor element, we evaluate the uncertainties of the magnetic field as:

$$\left|\Delta\mathbf{B}(x, y, z)\right| = \left|\mathbf{B}_L(x, y, z) - \mathbf{B}_S(x, y, z)\right|. \tag{3.59}$$

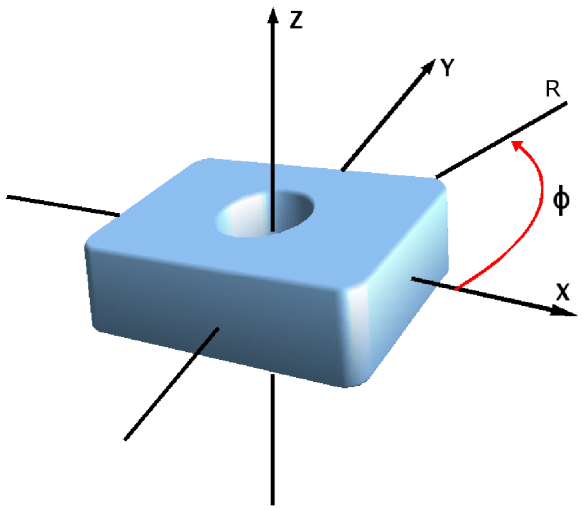

Figure 3.40: Coordinate system for magnetic field calculation of the conductor element

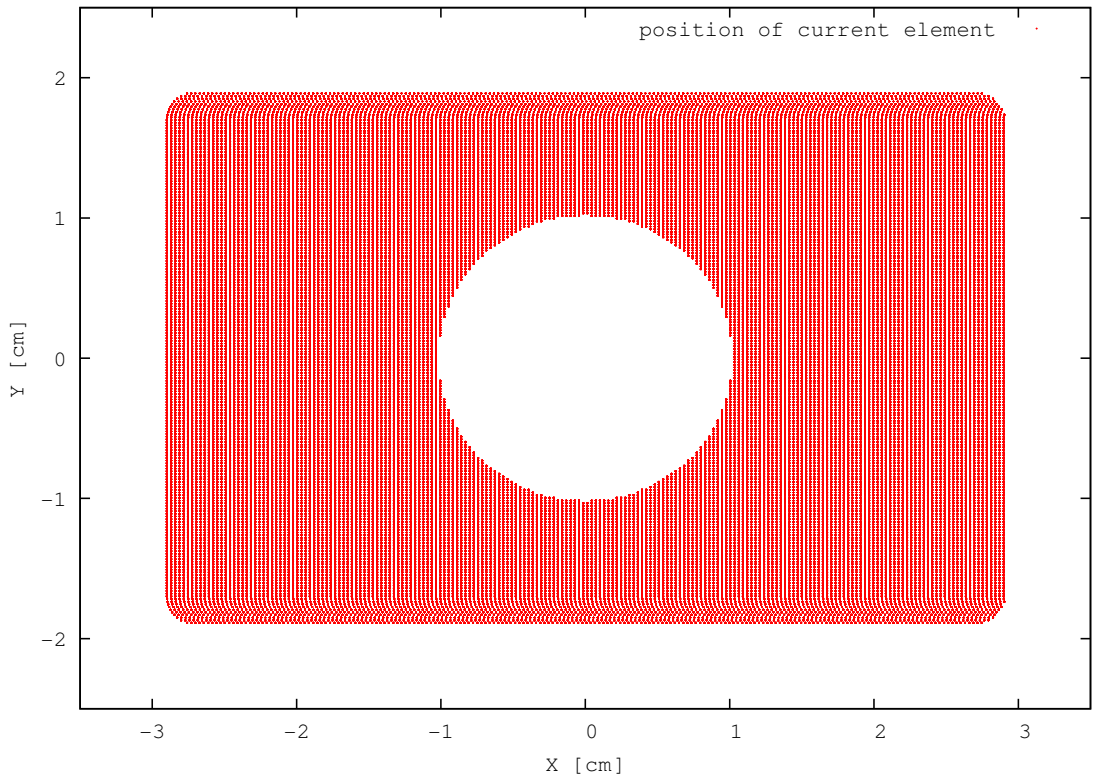

Figure 3.41: Dot-matrix representation of the conductor cross section showing the position of each tiny current element.

The calculated "true field" B_s and the uncertainty ΔB are shown in Fig. 3.42 (current is 8615.0 A, as per the QTOR simulation), where the test points are selected in the X-Y plane (where the magnetic field value is a maximum for a given radius R). The calculated values from the small current elements are indicated by the red crosses, and the uncertainties, i.e., the differences of field values, are indicated by the green crosses. From Fig. 3.42, we can see that:

- the magnetic field values and the corresponding uncertainties decrease with the increasing distance from the test point to conductor center, as expected,
- the current element approximation (large current element) we used in the QTOR simulation generally has good accuracy except at the regions that are very close to the surface of the conductor[10].

3.5.2 Uncertainties of the Magnetic Field Calculation

Many sources contribute to the uncertainties of the magnetic field calculation, such as the uncertainties of current element positions and orientations (due to the uncertainties in coil dimension measurements, uncertainities in approximations of coil geometry, etc.), round-off error accumulation, and so on. The most important uncertainties are produced by the finite current element approximation, as discussed in the previous section.

In order to obtain a quick estimate of the uncertainties in the magnetic field simulation, only the uncertainties from finite current element approximations are considered here. By using the position information for current elements that we have obtained in the QTOR simulation (see Fig. 3.16 for reference) and the uncertainties determined above, we can calculate the distances R_i from the test point $(x_0,\ y_0,\ z_0)$ to each conductor element in the coils of QTOR, and in turn work out the magnetic field uncertainty at the test point through summing over all their contributions to the uncertainties

[10] At a $\sim$ 7 cm distance to the conductor surface, the relative uncertainty is 1.1% (18.3 $\pm$ 0.2 Gauss), and at a $\sim$ 2 cm distance to the conductor surface, the relative uncertainty is 5.3% (85.2 $\pm$ 4.5 Gauss), for instance. In the Q^p_{Weak} experiment, however, the collimator was designed so that the electrons travel with at least a 2 cm clearance to any part of the QTOR, whether it is the coil or support structure. Therefore, it is not necessary to obtain a high accuracy in the regions that are very close to the conductor.

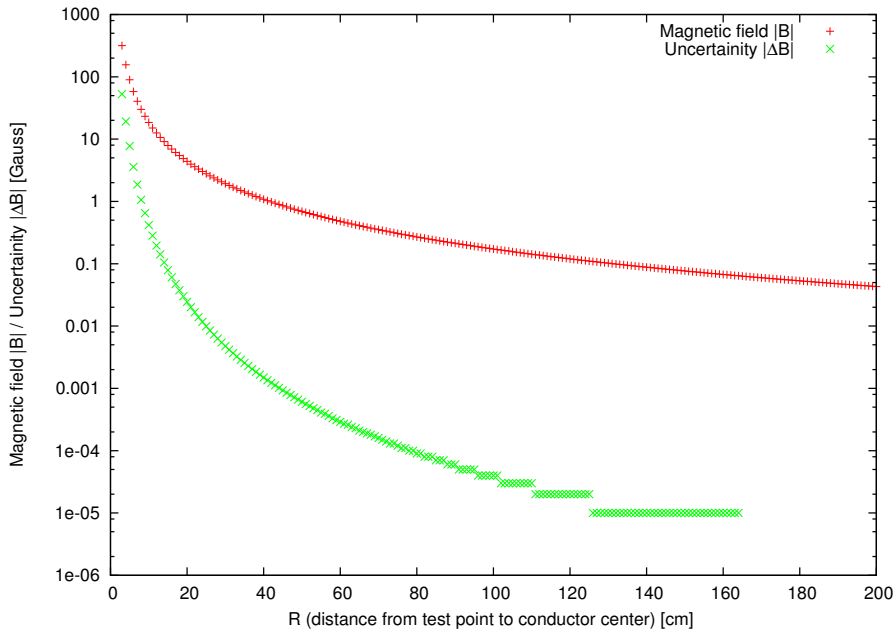

Figure 3.42: Magnetic field compare for different sized current elements

as:

$$\left|\Delta\mathbf{B}(x_0,\ y_0,\ z_0)\right| \sim \sum_i \left|\Delta\mathbf{B}(R_i)\right|. \tag{3.60}$$

Note that equation 3.60 overestimates the uncertainties since we simply add the amplitudes together, and do not consider the direction and sign of $\Delta\mathbf{B}(R_i)$. However, it does provide a quick estimate of an upper bound for field uncertainties.

Fig. 3.43 is an example (uncertainty map) that shows the result of the uncertainty calculation on the X-Z plane in sector 1 (the corresponding magnetic field maps are shown in Fig. 3.21 – 3.23), and Fig. 3.44 shows the uncertainty map on the $z = -190$ cm plane (upstream end of the magnet) in sector 1 (the corresponding magnetic field maps are shown in Fig. 3.24 – 3.26). Since the uncertainty at a field point is mainly determined by the nearby current elements, the points with large field uncertainities are located very close to the coils. At a radial distance $\sim$ 25 cm to the beam axis, where the number of current elements per unit volume is larger than other regions, the relative uncertainities have the maximum value ($\sim$ 2%). Within the envelope of electron trajectories, the

field uncertainities are far less than 5 Gauss. A quick estimation gives a value of 20 Gauss·m on the field integral uncertainities if we take 5 Gauss as the averaged field uncertainty and 4 m as the path length of electron in the magnetic field region, i.e., the simulation programs can calculate field integrals ($\sim$ 0.67 T·m) with an uncertainty smaller than 0.3%.

3.5.3 Uncertainties in Zero-Crossing Points

The uncertainties in zero-crossing positions can be estimated in terms of the magnetic field uncertainties in the calculation, and gradients at the zero-crossing point, i.e.,

$$\left|\Delta S_{\xi}\right| = \left| \Delta B_{\zeta} \Big/ \frac{\partial B_{\zeta}}{\partial S_{\xi}} \right|, \tag{3.61}$$

where $\xi = x,\ y$, or z, and $\zeta = x,\ y$, or z. Equation 3.61 shows that the larger the field gradients, the greater the accuracy that can be achieved in the location of the zero-crossing points. Therefore, in the zero crossing calculations and measurements, the zero crossing points should be selected as close to the high field gradient regions as possible. For the proposed zero-crossing points for the field mapping at the upstream $z = -190$ cm plane, we calculated their position uncertainties, as shown in Table 3.5, from which we see that the uncertainties in the calculation of the zero crossing positions are $\sim 0.03 - 0.23$ cm.

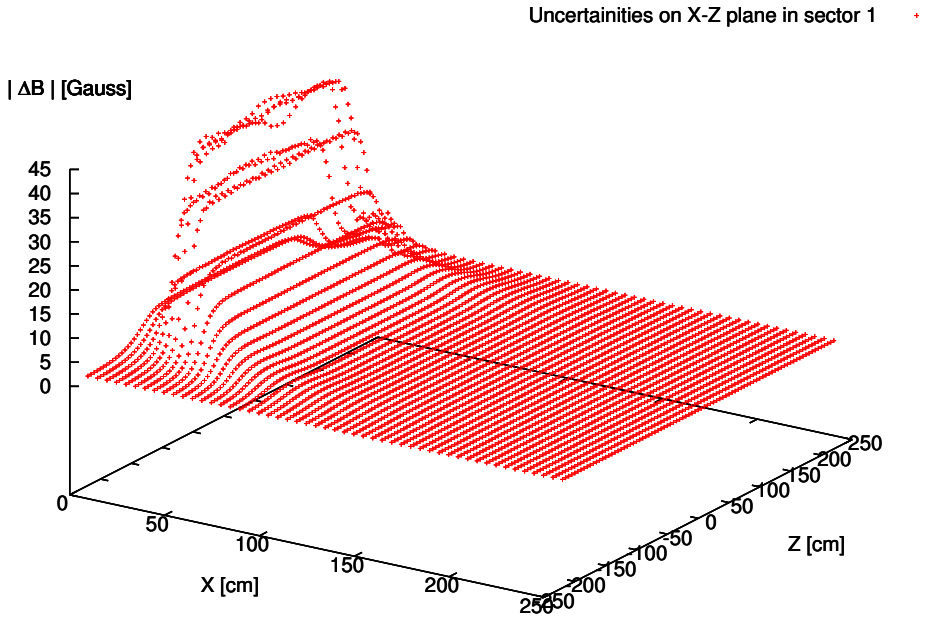

Figure 3.43: An uncertainty map on the X-Z plane in sector 1.

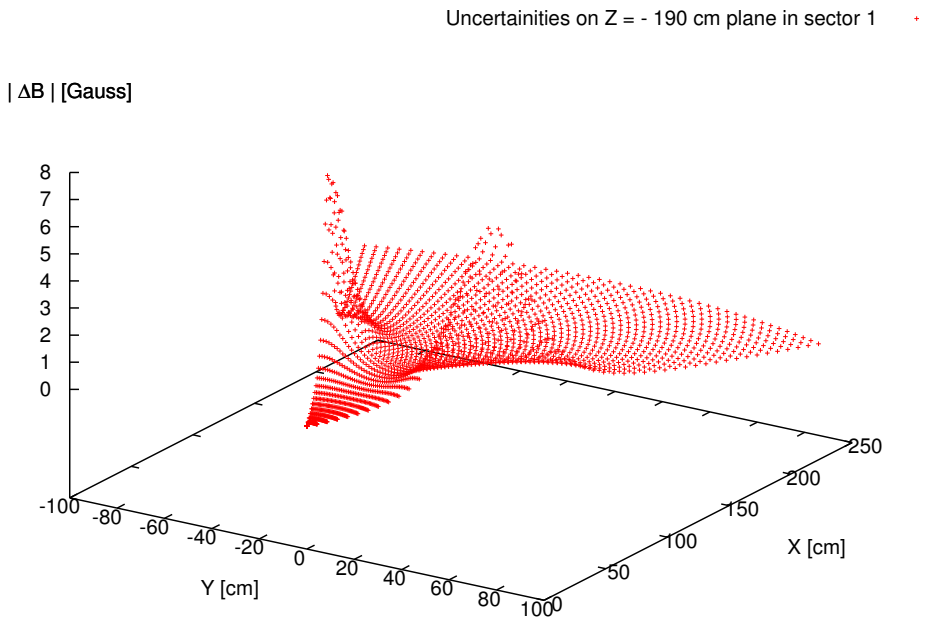

Figure 3.44: An uncertainty map on $z = -190$ cm plane (upstream end of the QTOR) in sector 1.

Field Components	*Coordinates* [cm]	*Field uncertainities* [Gauss]	*Gradients* [Gauss/cm]	*Zero-crossing uncertainties* [cm]
B_x	(155, 0.35, -190)	0.13	2.57	0.05
B_y	(155, -31.72, -190)	0.16	4.34	0.04
	(155, 30.79, -190)	0.16	4.35	0.04
B_z	(155, 0.03, -190)	0.13	3.77	0.04
B_x	(110, 0.55, -190)	0.41	3.58	0.12
B_y	(110, -25.20, -190)	0.94	20.68	0.05
	(110, 25.27, -190)	0.93	20.62	0.05
B_z	(110, 0.12, -190)	0.41	15.90	0.03
B_x	(60, 0.13, -190)	0.95	7.76	0.13
B_y	(60, -13.42, -190)	1.45	18.90	0.08
	(60, 13.65, -190)	1.41	18.64	0.08
B_z	(60, 0.42, -190)	0.95	14.15	0.07
B_x	(94.34, -15, -190)	0.92	4.27	0.22
	(95.21, 15, -190)	0.91	4.07	0.23

Table 3.5: Uncertainties of zero crossing positions

Chapter 4

Magnetic Field Mapping

Field mapping will play a very important role in the calibration and field verification of the QTOR magnet. A specific field mapping device [38] [39], originally developed by TRIUMF[1] for the G^0 experiment, will be used to perform this task. This chapter briefly introduces the field mapping device, the control and data acquisition software, and the field mapping procedure.

4.1 Basic Requirements for the Field Mapping

Magnetic field calculations and electron trajectory studies indicate that misalignments of the QTOR coils will cause displacements of the electron trajectories on the detector bars, which in turn lead to enhanced sensitivity to helicity correlated beam motion in the Q^p_{Weak} experiment, an important source of systematic error. Consequently, the coil misalignments must be kept as small as possible. This requires that the actual locations of the coils should be measured to high precision. As stated previously, QTOR is a toroidal magnet composed of 8 resistive coils placed symmetrically about the central beam axis, and its magnetic field can be completely determined if sufficient knowledge of the coils, including the dimensions, positions and orientations, is available. The coil dimensions were directly measured by the manufacturer and augmented by additional on-site measurements.

[1] The Tri-University Meson Facility in Vancouver, Canada's national laboratory for particle and nuclear physics.

However, the positions and orientations of coils in the support stand must be separately determined. Determination of the position and orientation of each coil is the major issue in the final installation/calibration phase of the QTOR magnet, and is discussed in this chapter. The previous chapter (Chapter 3) briefly introduced the distribution of zero-crossing points on planes perpendicular to the beam axis, in the QTOR fringe-field regions. In order to determine the location of the coils to high precision, we can use a field mapping device to scan the fringe-field regions of QTOR to locate a series of zero-crossing points of specific components of the magnetic field. This information can then be used to reconstruct the coil locations (this technique [40] [41] will be discussed in detail in the next chapter). After the reconstruction of the coil locations, we can then use the field simulation programs to calculate the exact QTOR magnetic field. Additional information can be obtained from direct measurements in the "high" field (or "gap") regions. These measurements will be performed to confirm the field integrals, using selected field points along the elastic electron trajectories, so that we can gain additional confidence in the field simulations. Thus, the field mapping should meet the following two basic requirements:

- it must enable us to locate the zero-crossing points at the upstream/downstream fringe-field regions of the QTOR magnet (called the zero-crossing measurement);
- it must provide accurate measurements at selected field points within the envelope of the elastic electron trajectories in order to evaluate the field integrals (called the direct field measurement),

with the aim of determining the coil displacements to an accuracy of ± 1.5 mm in coil position and $\pm 0.1^{\circ}$ in coil angle and matching the field integrals for the eight coils to an accuracy of $\sim 0.4\%$.

4.2 Field Mapper

An automated magnetic field mapper (i.e., a magnetic field verification system) is available to perform the field mapping of QTOR. This system [38] was developed earlier for the verification of

the G^0 toroidal magnet for the G^0 experiment at Jefferson Laboratory. In order to meet the field mapping requirements, its magnetic field probes can move along pre-defined scan paths to locate the zero-crossing points of specific field components to high precision, and/or measure the magnetic field at any selected point in three dimensions. The field mapper is capable of providing a position determination of ±0.3 mm and a magnetic field determination of ±0.2 Gauss. The actual field mapper consists of the field mapping device itself plus control and DAQ software, which are briefly described below.

4.2.1 Field Mapping Device

The field mapping device consists of three main systems: the motion system, the probe/sensor system and the control and DAQ (data-acquisition) system. The motion system is a three dimensional Cartesian linear motion assembly (a 3-axis gantry, see Fig. 4.1). A probe boom mounted on an axis carriage can move along three orthogonal axes over a range of 4 m × 4 m × 2 m. The probe/sensor system (see Fig. 4.2 and 4.3) consists of Hall probes (obscured from view), temperature sensors, clinometers, and photodiodes, which are mounted on the tip of the probe boom, and move with the boom. The magnetic fields are measured by two high precision 3-axis Hall Effect transducers [42] (active volume 0.25 mm × 0.25 mm × 0.2 mm). In order to match the probe axes to the sector frame axes of QTOR[2], and to cross-check the field values, the two probes are mounted adjacent to each other, but with the x-axis and y-axis of the second probe rotated by 45^o around the z-axis with respect to the first probe[3]. The temperature sensors measure the ambient temperature and are used to correct for the effects of changing temperatures. The probe holder angular orientation in space is also recorded as it moves through the mapping volume. Clinometers mounted on the probe holder are used to measure the tilt angles of the Hall probe axes so that necessary corrections can be made to the measured magnetic field component values. A system of photodiodes and laser beams [43]

[2]If the axes of a Hall probe are parallel to the axes of a sector frame, respectively, then the readings from that Hall probe can be directly treated as the the magnetic field component values at the measurement points in that sector frame.

[3]The first Hall probe matched to the sector 1 frame can be used to directly measure the field components in sectors 1, 3, 5, 7, and the second Hall probe matched to the sector 2 frame can be used to directly measure the field components in sectors 2, 4, 6, 8. At a same measurement point, the readings from one Hall probe can be used to verify the readings from another Hall probe.

is used to calibrate the position of the probes in the lab frame. There are some mechanical contact sensors mounted on the outside of the probes/sensors housing, which are used for safety purposes and serve as stop switches. When these contact sensors are triggered (i.e. when the probe/sensors housing makes contact with other objects), they will signal the control system to halt the motion of the probe boom immediately.

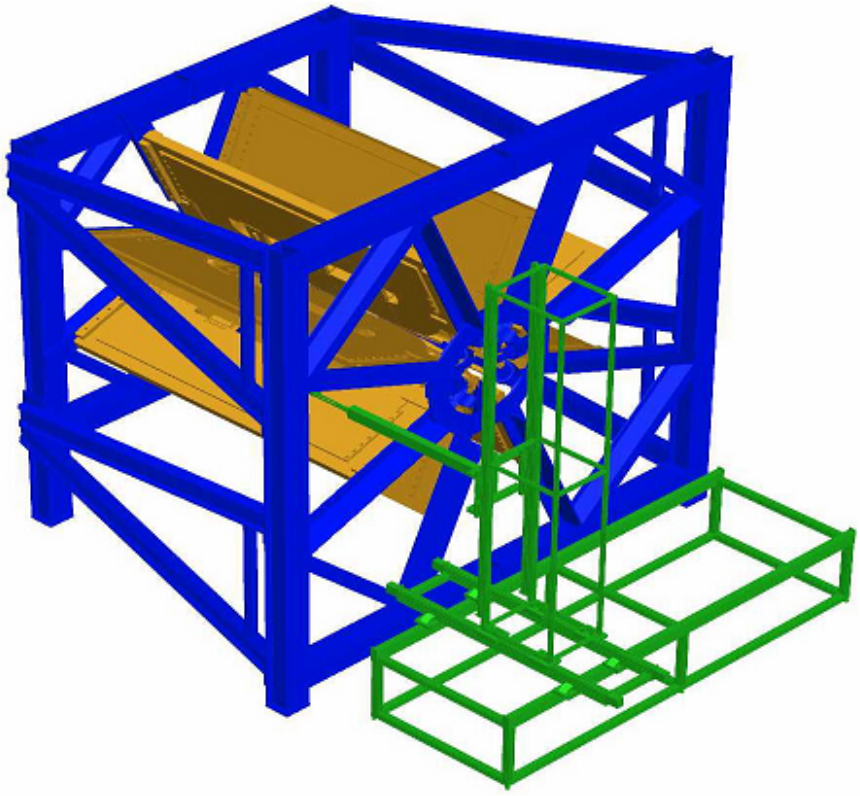

Figure 4.1: The magnetic field probes carried by the 3D motion system measure the field of QTOR at any selected field point.

The control system layout is shown in Fig. 4.4. The 3-dimension linear motion system (i.e., the gantry) is guided by a DMC[4] control system (PCI[5] GALIL controller card[6]), and driven by servo

[4]DMC (Dynamic Matrix Control) is a control algorithm, which uses a linear step response model to predict future output changes as a linear combination of future input moves (a weighted sum of past input changes), so as to drive the output as close to the setpoint as possible in a least-squares sense.

[5]Peripheral Component Interconnect, a standard which specifies a computer bus for attaching peripheral devices to a computer motherboard.

[6]A PCI-based high precision motion control device developed by Galil Motion Control, Inc. (California, USA)

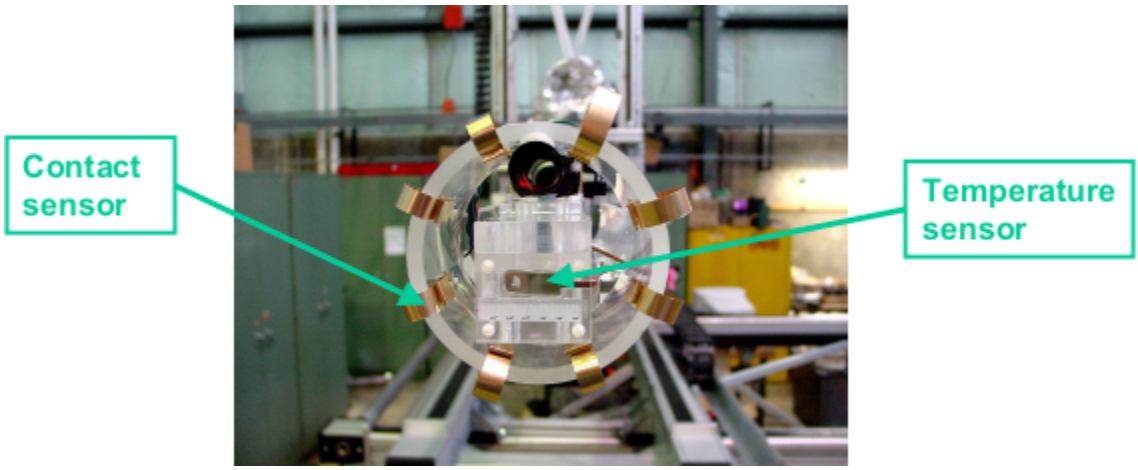

Figure 4.2: Front view of probe assembly. The Hall probes (obscured from view) are located behind the temperature sensor.

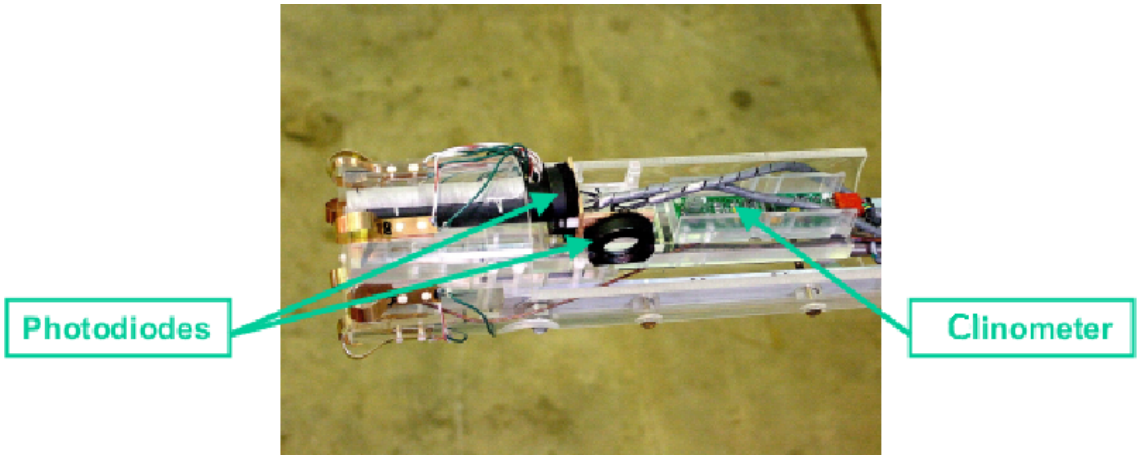

Figure 4.3: Side view of probe assembly

amplifiers. All digital and analog signals of the probes/sensors are read out via digital I/O[7] and ADC[8] channels on a series of PCI DAQ cards, and then processed on a Windows-based PC[9].

4.2.2 Supervisory Control and Data Acquisition Software

A supervisory control and data acquisition program provides an interface between the user and the field mapping device. Through this system, the user can control the motion of the probe boom, read out the data from probes and sensors, and then record, process and analyze these data. For the QTOR magnetic field mapping, this program automatically controls the field mapping device and measures the field values at a series of selected space points according to an input script, and then produces an output file that contains the magnetic field and other relevant data. From analysis of these data, we can determine the zero-crossing points, generate the actual field map, calculate the field integrals, and so on.

The supervisory control and data acquisition software was developed in the LabVIEW integrated development environment[10] by using the G language[11]. The resulting software package consists of a number of subsystems (all wrapped within a LabVIEW-based program), and was named as MaVeriK (**M**agnetic **V**erification **K**ernel)[12]. Fig. 4.5 shows the graphical user interface of MaVeriK.

MaVeriK makes use of LabView's multi-threaded management mechanism. All threads can be executed in parallel. The programs consist of two major sequences: the initialization and main program loop(s). Initialization sets up the initial gantry parameters, loads the forward and backward interpolation tables, creates ADC data notifiers and generates ADC data occurrences, loads the DMC initialization file as well as the collision-avoidance data, initializes the PCI cards and sets up global reference variables, etc.

[7] Input/Output

[8] Analog-to-Digital Converter

[9] Personal Computer

[10] LabVIEW is an integrated development environment, which creates programs in block diagram form. LabVIEW programs are also called virtual instruments, or VIs, because their appearance and operation imitate physical instruments, such as oscilloscopes and multimeters. Every VI uses functions that manipulate input from the user interface or other sources and display that information or move it to other files or other computers.

[11] The G language is an easy to use graphical programming language on which LabView is based. It simplifies the computation, process monitoring and control, and test and measurement applications.

[12] MaVeriK program authors: E. Gamroth, A. Horning, C. Hynes, L. Lee, T. Ries (2001).

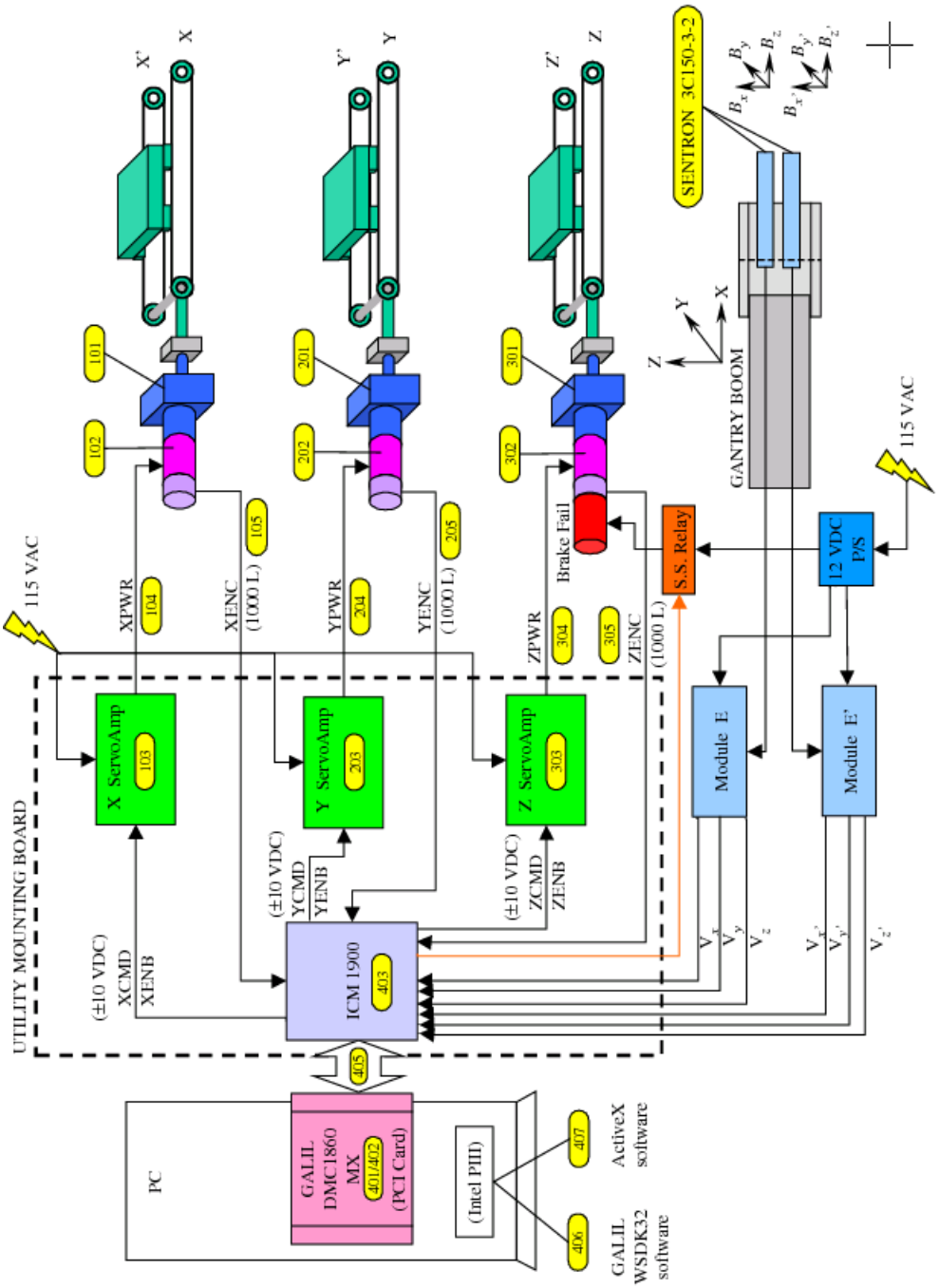

Figure 4.4: Layout of the control system [38]

The main program includes:

- Gantry kernel loop: this loop includes automatic control mode and manual control mode, which controls all of the movements of the gantry (controls the motion and communicates with the low-level motor control macro running on the GALIL card). All GALIL controls, except for certain types of "emergency" stops (hardware and software) are controlled by this loop. Some data acquisition is also carried out by this loop. This loop firstly parses position/motion commands from the GUI (graphical user interface), then performs the coordinate transformations (magnet coordinates → gantry coordinates → shaft encoder coordinates) and the safety check. The safety check is a collision-avoidance routine, which checks for potential collisions and illegal motions. If a movement is safe, the motion commands will be passed to the GALIL motor-controller card.

- ADC data loop: this loop acquires data from sensors and communicates (via built-in National Instruments drivers for some cards, and custom/OEM[13] drivers for other cards) with the ADC and I/O cards, then passes data to the ADC display loop. It calls the VI (a VI is a "Virtual Instrument" or subprogram/subroutine) "AI[14] Multi-Devices" which sets up the ADC channels and thermocouple board, then requests data from them. The data are read and sent out via a "notifier" (a logical event flag/pointer). By using a notifier, multiple objects can receive the data.

- ADC display loop: this loop updates all of the indicators that are related to the ADC cards. This includes the Histogram, Oscilloscope, Power Spectrum, and the ADC Indicator Displays.

- Gantry information loop: this loop controls the updating of information about the gantry. This loop has no control over the GALIL controller card; it is only used to interrogate the card for the current GALIL values and then displays them on the front panel.

- GUI handler loop: this loop controls what indicators and controls are shown on the front

[13] Original Equipment Manufacturer
[14] Analog Input

panel, that is to control data displays on main GUI panels, control the display of command parameters and buttons. It also handles the toggling between manual/automatic/jog modes.

- Menu loop: this loop controls the menu on the front panel. When a menu item is selected, this loop decides what happens. This loop also controls the stop button.
- Jog mode control loop: this loop is a convenient tool for empirical determination of keep-in zones, and is usually employed in conjunction with the contact sensors, which are mounted on the tip of the probe boom.
- Gantry position data acquisition log loop: this loop is used to store the present and historic position of the gantry.

The most important subroutines combined in these loops are the motion control subroutine, the data acquisition subroutine and the safety subroutine.

4.3 Field Mapping Procedure

The procedure for the field mapping includes the selection of measurement points, the field mapper installation, the field measurements, and the data analysis, which are briefly discussed below.

The field measurements, including the zero-crossing measurements and the direct field measurements, will be carried out at pre-selected space points. The selection of zero-crossing points is based on studies of the actual magnet, and includes consideration of the obstructions posed by the support stand, plumbing and electrical connections, etc. The manufactured coil data and nominal coil locations are used to find the approximate positions of zero-crossing points on both an upstream plane of constant z (perpendicular to beam axis, $z = -190$ cm, for example) and a downstream plane of constant z (perpendicular to beam axis, $z = 190$ cm, see Fig. 3.28–Fig. 3.32 for reference). From these simulated zero-crossing points, we propose to scan approximately 30 zero-crossing points per sector, for eight sectors of QTOR. A possible set of 28 zero-crossing points is shown in Table 4.1. The field mapper will scan a region ±3 cm around each of these points in the X or Y direction to

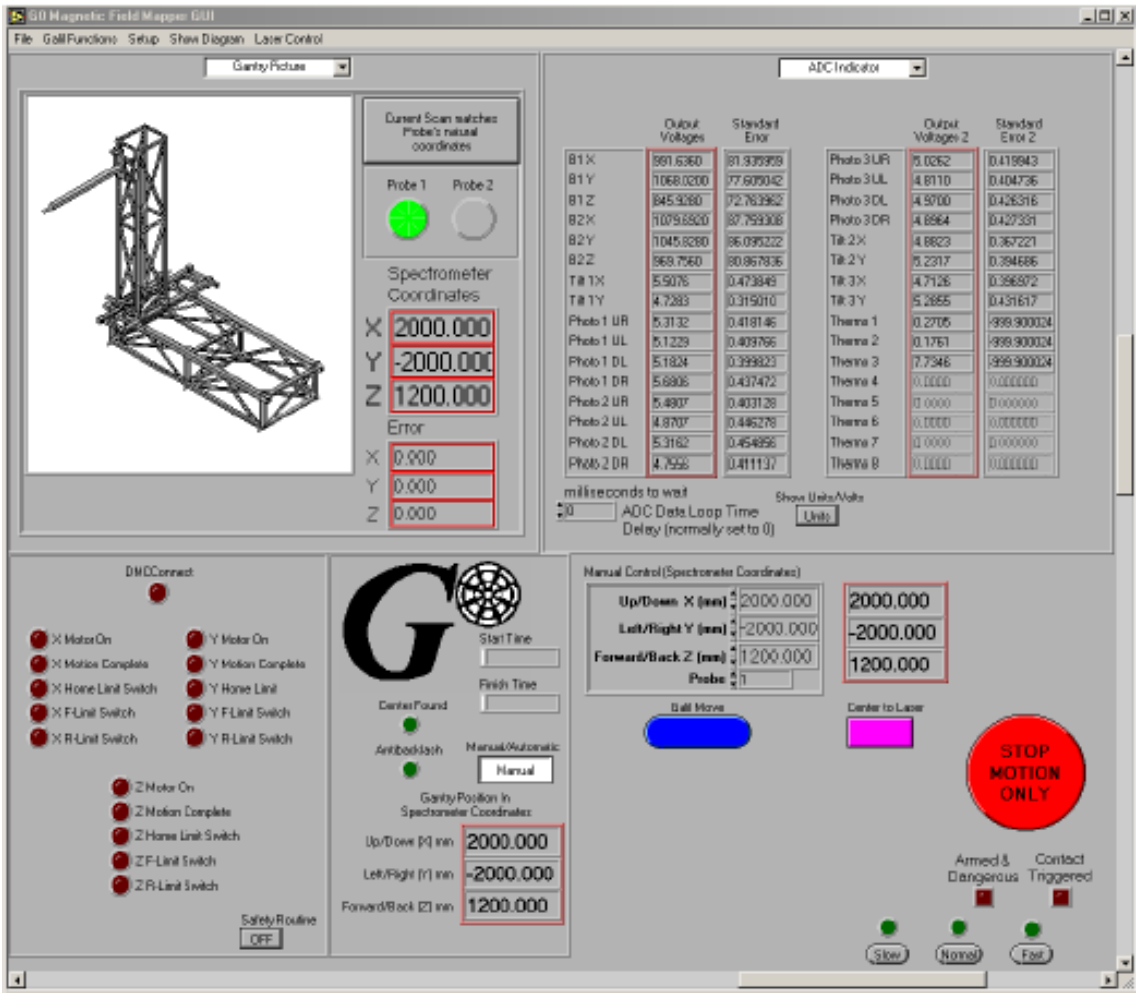

Figure 4.5: Main graphical user interface (GUI) of MaVeriK

determine positions of the experimental zero-crossing points. The scan lines on an upstream plane of constant Z ($z = -190$ cm) are indicated in Fig. 4.6.

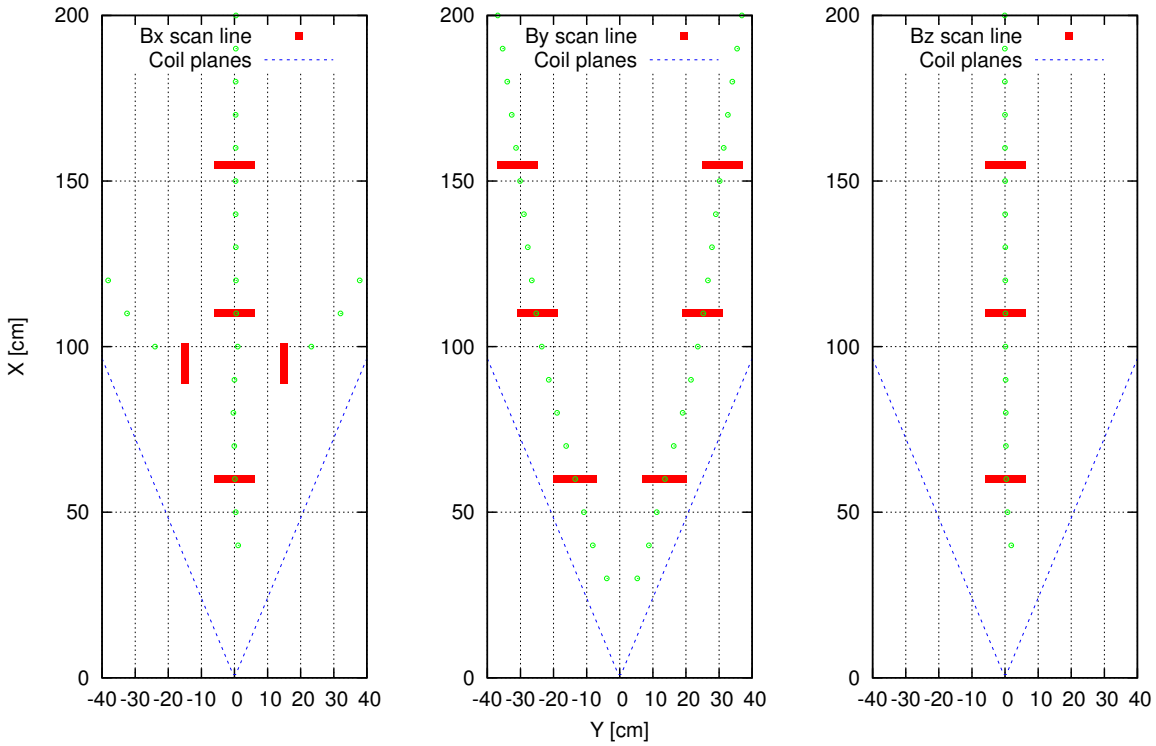

Figure 4.6: Scan lines on an upstream plane of constant z ($z = -190$ cm). The bold red lines indicate the positions of scan lines and scan directions for the zero-crossing points of B_x (left), B_y (middle) and B_z (right).

The points for the direct field measurements should be within the envelope of the elastic electron trajectories. The more points we select, the greater the accuracy we can achieve for the field integral confirmation and the direct field verification. The measurement for each point will take an average of about 10 seconds. For a grid of 2000 field points in one octant, we will need at least 45 hours to carry out the measurements, corresponding to 54 MWH power consumption in the case of operation at full current (8615 A, 1.2 MW). The final selection of the grid of field points to be measured will depend on future budgetary decisions associated with the power costs to run the magnet.

The field mapper installation should be carried out as early as one or two months before the

Location	*Scan direction*	*Field component (zero-crossing type)*	*Approximate zero-crossing coordinates* (±0.5 cm *in scan direction)*	*Number of zero-crossing points*
upstream z = -190 plane	Y	B_x	(155, 0, -190)	1
		B_y	(155, -31, -190) (155, 31, -190)	2
		B_z	(155, 0, -190)	1
		B_x	(110, 0, -190)	1
		B_y	(110, -25, -190) (110, 25, -190)	2
		B_z	(110, 0, -190)	1
		B_x	(60, 0, -190)	1
		B_y	(60, -13, -190) (60, 13, -190)	2
		B_z	(60, 0, -190)	1
	X	B_x	(95, -15, -190) (95, 15, -190)	2
downstream z = 190 plane	Y	B_x	(155, 0, 190)	1
		B_y	(155, -31, 190) (155, 31, 190)	2
		B_z	(155, 0, 190)	1
		B_x	(110, 0, 190)	1
		B_y	(110, -25, 190) (110, 25, 190)	2
		B_z	(110, 0, 190)	1
		B_x	(60, 0, 190)	1
		B_y	(60, -13, 190) (60, 13, 190)	2
		B_z	(60, 0, 190)	1
	X	B_x	(95, -15, 190) (95, 15, 190)	2

Table 4.1: Selection of scan directions and zero-crossing points for the upstream and downstream area (SECTOR frame, in unit of cm). The coordinates are approximate (±0.5 cm) crossing coordinates in the scan direction.

actual field measurements are to take place. Not only are there tasks, such as transporting the mapper to the test site, re-assembling, rechecking, debugging wiring (and so on) that need to be done, but we also need to recalibrate the gantry (survey/alignment, via laser-tracker) and tune-up the mapper via calibration studies and practice/dummy scans. The actual measurements should follow the steps below:

- measure the zero-crossing points of specific B-field components,
- adjust individual coil positions if the data analysis indicates that is necessary,
- remeasure the zero-crossing points,
- make direct field measurements for confirming the field integrals, etc.

The data analysis consists of the direct verification of the fields, the confirmation of the field integrals, and the reconstruction of the individual coil locations. When we obtain the values at the selected grid of field points, we can interpolate the data for any desired field point. Comparing this field map with the simulated map, we can directly verify the magnetic field. The actual field integrals can eventually be evaluated by tracing scattered electrons through the actual field and measuring their trajectories. The most important data analysis for field mapping is the reconstruction of the coil locations by using the zero-crossing analysis technique, which will be discussed in detail in the next chapter.

4.4 Field Mapping Issues

There are a number of unresolved issues regarding the field mapping of the QTOR. For example, the electric power consumption utilized in the future field mapping process will be an important consideration due to the limited field mapping budget. One way to mitigate this problem is to perform the field mapping at reduced current (4000 A, for instance), and then scale the results to the

full driven current[15]. The geometry of the desired grid of field points can also be adjusted to reduce the electric power consumption. The field mapper is originally designed for mapping G^0 toroidal magnet, and its Hall probes only have a measurement range of ±0.2 T. In the Q^p_{Weak} experiment, the maximum field strength is $\sim$ 0.5 T. Therefore, the Hall probes need to be changed to ones with wider measurement ranges if we are to perform the direct field measurement in the high field regions (to verify the field integrals). In addition, the collision-avoidance routine in the MaVeriK software will need to be modified according to the geometry of QTOR so that the probes do not collide with obstructions, such as the coil carrier, the stand, coil connection jumpers, leads, and so on. These issues must be resolved before the actual field measurement can be conducted.

[15]However, this procedure does not guarantee the coils do not move slightly at high current and thus result in a QTOR field profile of different symmetry. A full current field map is therefore highly desirable.

Chapter 5

Analyzing Zero-Crossing Measurements

The magnetic fields of the QTOR can be completely determined if sufficient knowledge of the current distribution within the coils and their positions and orientations are known. We know the overall coil dimensions from directly measuring the manufactured coils, and have reasonable estimates of the current distribution within the coils. However, their positions and orientations are difficult to infer from the direct measurements when the QTOR is assembled. Therefore, the accurate determination of the position and orientation of each coil is the major task in the final installation/calibration of the QTOR. A previous chapter (Chapter 3) discussed briefly the existence of zero-crossing points, at planes of constant z in the fringe-field regions of the QTOR that are sensitive to coil positions. In order to determine the location of the coils to high precision, we can use a field mapping device to scan and locate a series of zero-crossing points in specific components of the magnetic field, and then use this information to reconstruct the coil locations. This zero-crossing analysis technique for inferring the coil locations is described in detail in this chapter.

5.1 Zero-Crossing Methodology

The basic idea of the zero-crossing method is to set up a so-called "sensitivity matrix" that represents the derivatives of zero-crossing points with respect to discrete displacements of the coils from their

nominal positions. Considering these effects to first order only, a set of linear equations can be constructed by using the measured and simulated zero-crossing positions, the sensitivity matrix, and the unknown positions and orientations of coils. This set of equations can then be solved for the unknowns, as discussed below:

We define the zero-crossing point $\xi_{i,n}^{\alpha,\gamma}$ and zero-crossing displacement $\Delta\xi_{i,n}^{\alpha,\gamma}$, where

- $n = 1 \ldots 8$ refers to the n^{th} sector,
- $i = 1 \ldots 28$ refers to the i^{th} zero-crossing point in the n^{th} sector (we select 28 zero-crossing points per sector for purposes of discussion),
- α is a label that specifies the field component ($\alpha = 1,\ 2,\ 3$ corresponds to B_x, B_y, B_z) that changes sign at this point,
- γ is a label that characterizes the implied scan direction (the direction along which the zero-crossing displacement will be measured, $\gamma = 1,\ 2,\ 3$ corresponds to scans in the X, Y and Z direction, respectively).

All of the above quantities are specified in the sector reference frame (refer to Fig. 3.3). We also define coil displacements from their nominal position as $\Delta\zeta_m^{\beta}$, where

- $m = 1 \ldots 8$ is the coil number,
- β is the type of coil displacement ($\beta = 1,\ 3,\ 5$ corresponds to displacements of the coil centers in the X, Y, Z directions, respectively, and $\beta = 2,\ 4,\ 6$ corresponds to the coil rotation angles about the coordinate axes. Here we are using a different coordinate system, as shown in Fig. 5.1. For example, ζ^1 refers to the X coordinate of the coil center, and ζ^5 refers to the θ_y, the coil rotation angle with respect to Y-axis).

Because the zero-crossing position ξ is determined by the coil locations, i.e., ξ is a function of coil location parameter ζ, then, to the first order, we can write

$$\Delta\xi_{i,n}^{\alpha,\gamma} = \sum_{m=1}^{8} \sum_{\beta=1}^{6} \left(\frac{\partial \xi_{i,n}^{\alpha,\gamma}}{\partial \zeta_m^{\beta}} \right) \Delta\zeta_m^{\beta} \,. \tag{5.1}$$

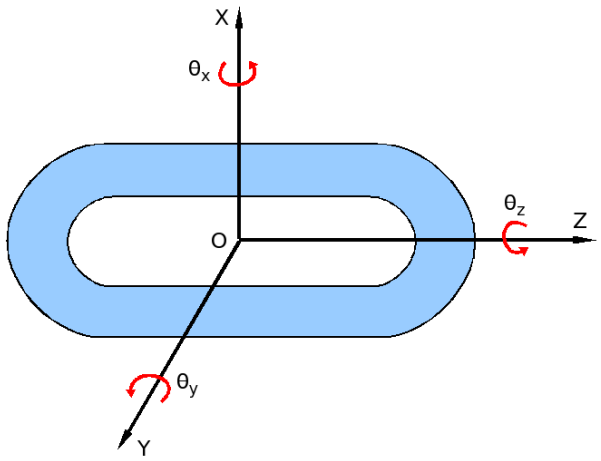

Figure 5.1: Coil location parameters

The calculation of the partial derivatives $\partial\xi_{i,n}^{\alpha,\gamma}/\partial\zeta_m^{\beta}$ is discussed in section 5.2.2.

It cannot be assumed that the QTOR will be properly aligned in position and rotation with respect to the magnetic field mapper[1]. This also affects the measured zero-crossing positions. To make provision for this misalignment, three degrees of freedom — displacements along the X-axis and Y-axis, and rotation about the Z-axis, are introduced. Since two separate setups of the field mapper are required (for mapping at the upstream and downstream ends), a total of six degrees of freedom are introduced. These are specified by $m = 9, \beta = 1 \ldots 6$. Note that these degrees of freedom are not a complete representation of the QTOR displacement with respect to the mapper; they are the most important ones[2], however. The discussion of the derivatives $\partial\xi_{i,n}^{\alpha,\gamma}/\partial\zeta_{m=9}^{\beta}$ is presented in section 5.2.2. The misalignment of the Hall probe axes with the lab frame axes can be characterized by six angles as discussed in section 5.2.2. Thus, $m = 10, \beta = 1 \ldots 6$ applies to Hall probe 1 and $m = 11, \beta = 1 \ldots 6$ applies to Hall probe 2.

[1]Note that the magnetic field mapper is treated as the reference frame in this discussion.

[2]The displacements of QTOR along the Z-axis and rotations about the X-axis or Y-axis have smaller effect on the zero-crossing positions, as discussed in section 3.4.5.

With these additions, equation 5.1 is replaced by

$$\Delta\xi_{i,n}^{\alpha,\gamma} = \sum_{m=1}^{11}\sum_{\beta=1}^{6}\left(\frac{\partial\xi_{i,n}^{\alpha,\gamma}}{\partial\zeta_m^{\beta}}\right)\Delta\zeta_m^{\beta}, \tag{5.2}$$

which contains $i \times n$ ($28 \times 8 = 224$) linear equations. These equations are the linear equations for coil displacements, where all $\Delta\xi_{i,n}^{\alpha,\gamma}$ form a vector $\mathbf{Z}$ (the zero-crossing displacement vector), all $\Delta\zeta_m^{\beta}$ form a vector $\mathbf{U}$ (the misalignment vector for the coils, the Hall probes and the field mapper), and the $(m \times \beta) \times (i \times n) = (11 \times 6) \times (28 \times 8)$ matrix (denoted as $\mathbf{S}$) with element $\partial\xi_{i,n}^{\alpha,\gamma}/\partial\zeta_m^{\beta}$ is the so-called sensitivity matrix. The vector expression of equation 5.2 can then be written as:

$$\mathbf{Z} = \mathbf{S} \cdot \mathbf{U} \tag{5.3}$$

with explicit representation:

$$\begin{pmatrix} \Delta\xi_{1,1}^{\alpha,\gamma} \\ \Delta\xi_{2,1}^{\alpha,\gamma} \\ \vdots \\ \Delta\xi_{28,1}^{\alpha,\gamma} \\ \Delta\xi_{1,2}^{\alpha,\gamma} \\ \vdots \\ \vdots \\ \Delta\xi_{28,8}^{\alpha,\gamma} \end{pmatrix} = \begin{pmatrix} \frac{\partial\xi_{1,1}^{\alpha,\gamma}}{\partial\zeta_1^1} & \frac{\partial\xi_{1,1}^{\alpha,\gamma}}{\partial\zeta_2^1} & \cdots & \frac{\partial\xi_{1,1}^{\alpha,\gamma}}{\partial\zeta_{11}^1} & \frac{\partial\xi_{1,1}^{\alpha,\gamma}}{\partial\zeta_1^2} & \cdots & \cdots & \frac{\partial\xi_{1,1}^{\alpha,\gamma}}{\partial\zeta_{11}^6} \\ \frac{\partial\xi_{2,1}^{\alpha,\gamma}}{\partial\zeta_1^1} & \frac{\partial\xi_{2,1}^{\alpha,\gamma}}{\partial\zeta_2^1} & \cdots & \frac{\partial\xi_{2,1}^{\alpha,\gamma}}{\partial\zeta_{11}^1} & \frac{\partial\xi_{2,1}^{\alpha,\gamma}}{\partial\zeta_1^2} & \cdots & \cdots & \frac{\partial\xi_{2,1}^{\alpha,\gamma}}{\partial\zeta_{11}^6} \\ \vdots & \vdots & & \vdots & \vdots & & & \vdots \\ \frac{\partial\xi_{28,1}^{\alpha,\gamma}}{\partial\zeta_1^1} & \frac{\partial\xi_{28,1}^{\alpha,\gamma}}{\partial\zeta_2^1} & \cdots & \frac{\partial\xi_{28,1}^{\alpha,\gamma}}{\partial\zeta_{11}^1} & \frac{\partial\xi_{28,1}^{\alpha,\gamma}}{\partial\zeta_1^2} & \cdots & \cdots & \frac{\partial\xi_{28,1}^{\alpha,\gamma}}{\partial\zeta_{11}^6} \\ \frac{\partial\xi_{1,2}^{\alpha,\gamma}}{\partial\zeta_1^1} & \frac{\partial\xi_{1,2}^{\alpha,\gamma}}{\partial\zeta_2^1} & \cdots & \frac{\partial\xi_{1,2}^{\alpha,\gamma}}{\partial\zeta_{11}^1} & \frac{\partial\xi_{1,2}^{\alpha,\gamma}}{\partial\zeta_1^2} & \cdots & \cdots & \frac{\partial\xi_{1,2}^{\alpha,\gamma}}{\partial\zeta_{11}^6} \\ \vdots & \vdots & & \vdots & \vdots & \ddots & & \vdots \\ \vdots & \vdots & & \vdots & \vdots & & \ddots & \vdots \\ \frac{\partial\xi_{28,8}^{\alpha,\gamma}}{\partial\zeta_1^1} & \frac{\partial\xi_{28,8}^{\alpha,\gamma}}{\partial\zeta_2^1} & \cdots & \frac{\partial\xi_{28,8}^{\alpha,\gamma}}{\partial\zeta_{11}^1} & \frac{\partial\xi_{28,8}^{\alpha,\gamma}}{\partial\zeta_1^2} & \cdots & \cdots & \frac{\partial\xi_{28,8}^{\alpha,\gamma}}{\partial\zeta_{11}^6} \end{pmatrix} \cdot \begin{pmatrix} \Delta\zeta_1^1 \\ \Delta\zeta_2^1 \\ \vdots \\ \Delta\zeta_{11}^1 \\ \Delta\zeta_1^2 \\ \vdots \\ \vdots \\ \Delta\zeta_{11}^6 \end{pmatrix}. \tag{5.4}$$

The misalignment vector $\mathbf{U}$ contains $m \times \beta$ ($11 \times 6 = 66$) unknowns. The elements of the zero-crossing displacement vector $\mathbf{Z}$ can be obtained by experimental measurements and information from the field simulation programs, as described in section 5.2.1. Likewise, the derivatives in the sensitivity matrix $\mathbf{S}$ can be calculated from the field simulation programs. Hence, we can solve for

the misalignment vector **U** by using:

$$\mathbf{U} = \mathbf{S}^{-1} \cdot \mathbf{Z} \tag{5.5}$$

if the inverse of the matrix **S** exists.

5.2 Algorithms

5.2.1 Zero-Crossing Displacement Vector

In the magnetic field programs, the normal zero-crossing points $\xi^{\,0}$ are calculated at nominal coil positions and orientations without any coil displacement, and, of course, with proper mapper alignment and correct probe alignments. The experimental (or simulated) zero-crossing points ξ' can be measured by the field mapper. Thus, the experimental zero-crossing displacements can be obtained through:

$$\Delta\xi_{i,n}^{\alpha,\gamma} = \left(\xi_{i,n}^{\alpha,\gamma}\right)' - \left(\xi_{i,n}^{\alpha,\gamma}\right)^0 ; \tag{5.6}$$

these are used to construct the zero-crossing displacement vector **Z**.

5.2.2 Sensitivity Matrix

The elements in the sensitivity matrix are derivatives for the coil displacements, the Hall probe misalignments and the QTOR misalignment with respect to the field mapper coordinates (i.e., the derivatives of the zero-crossing positions as a function of the locations of the coils, Hall probes and QTOR magnet). They are obtained through the following procedure.

Derivatives for the coil displacements

In the field simulation programs, we allow each coil to shift a distance of δx or δy or δz along the respective X, Y, or Z axes, or to rotate through an angle of $\delta\theta_x$ or $\delta\theta_y$ or $\delta\theta_z$ about the X, Y, or Z axis, as shown in Fig. 5.1. For each discrete shift or rotation (refer to section 3.2.2), we calculate 28 zero-crossing points for each sector. Thus, we obtain all the required zero-crossing points ξ''

for each of 48 discrete coil displacements (i.e., each coil has 6 types of displacement), from which we can calculate the derivatives for the coil displacements. For example, for the derivatives that correspond to the i^{th} zero-crossing point in sector n, due to displacement of coil 2 by δy, we would write

$$\frac{\partial \xi_{i,n}^{\alpha,\gamma}}{\partial \zeta_{m=2}^{\beta=3}} = \frac{\left(\xi_{i,n}^{\alpha,\gamma}\right)'' - \left(\xi_{i,n}^{\alpha,\gamma}\right)^0}{\delta y}, \tag{5.7}$$

and for a rotation of coil 4 by $\delta\theta_z$,

$$\frac{\partial \xi_{i,n}^{\alpha,\gamma}}{\partial \zeta_{m=4}^{\beta=6}} = \frac{\left(\xi_{i,n}^{\alpha,\gamma}\right)'' - \left(\xi_{i,n}^{\alpha,\gamma}\right)^0}{\delta \theta_z}. \tag{5.8}$$

In this way, we can work out all the elements that have superscript $\beta = 1 \ldots 6$ and subscript $m = 1 \ldots 8$ on ζ to fill in the sensitivity matrix.

Derivatives for the QTOR misalignment with respect to the field mapper

As mentioned in the previous section, the measured values for the positions of the zero-crossing points are affected by the QTOR misalignments with respect to the field mapper. In the simulation programs, these misalignments are defined by 6 parameters: δx_u, δy_u, $\delta \phi_u$, δx_d, δy_d, $\delta \phi_d$[3], which are the QTOR shifts in X, Y directions and azimuthal rotations with respect to the field mapper (note that we treat the field mapper as reference frame, instead of the QTOR) for the field mapper located at upstream or downstream ends of the toroidal magnet[4].

At the upstream or downstream ends of the QTOR, we have a set of calculated zero-crossing points $\xi_{i,n}^{\alpha,\gamma}$. If we can obtain another set of zero-crossing positions ξ''' in the reference system of the field mapper in the case that the QTOR is misaligned with respect to the mapper (the QTOR shifts and rotations can be simulated via shifts and rotations of coils, see section 3.2.2 for reference), we can then calculate the derivatives for the QTOR misalignment. For example, for the mapper located at the upstream end of the QTOR, we write the derivatives that correspond to the i^{th} zero-crossing

[3]The subscript "u" refers to "upstream", and the subscript "d" refers to "downstream".

[4]We ignore possible shifts in Z direction and other rotations in order to simplify the calculation.

point in sector n with zero-crossing displacements in Y ($\alpha = 2$) direction as:

$$\frac{\partial \xi_{i,n}^{\alpha,\gamma}}{\partial \zeta_{m=9}^{\beta=1}} = \frac{\left(\xi_{i,n}^{\alpha,\gamma}\right)''' - \left(\xi_{i,n}^{\alpha,\gamma}\right)^0}{\delta x_u} \tag{5.9}$$

$$\frac{\partial \xi_{i,n}^{\alpha,\gamma}}{\partial \zeta_{m=9}^{\beta=2}} = \frac{\left(\xi_{i,n}^{\alpha,\gamma}\right)''' - \left(\xi_{i,n}^{\alpha,\gamma}\right)^0}{\delta y_u} \tag{5.10}$$

$$\frac{\partial \xi_{i,n}^{\alpha,\gamma}}{\partial \zeta_{m=9}^{\beta=3}} = \frac{\left(\xi_{i,n}^{\alpha,\gamma}\right)''' - \left(\xi_{i,n}^{\alpha,\gamma}\right)^0}{\delta \phi_u} \tag{5.11}$$

In this way, we can work out all the elements that have superscript $\beta = 1 \ldots 6$ and subscript $m = 9$ on ζ to fill in the sensitivity matrix.

Derivatives for the Hall probe misalignments

After the best effort at aligning the 3-D Hall probes, we have three effective axes for each Hall probe: $\mathbf{n}_x$, $\mathbf{n}_y$ and $\mathbf{n}_z$ specified in the lab frame. The Hall probes measure the different magnetic field components along the directions of these axes. However, we cannot assume that $\mathbf{n}_x$, $\mathbf{n}_y$ and $\mathbf{n}_z$ are mutually exactly orthogonal and aligned with the axes of the lab frame. We define 6 parameters to describe the misalignments of each Hall probe. They are the polar angles and the azimuthal angles (specified in Fig. 5.2) for each axis of each Hall probe in the lab frame. The polar angles and the azimuthal angles for probe axes are defined in a canonical pattern as:

- for the $\mathbf{n}_x$-axis, the polar angle is the angle between Z-axis and $\mathbf{n}_x$, and the azimuthal angle is the angle between X-axis and the projection of $\mathbf{n}_x$ on the X-Y plane,
- for the $\mathbf{n}_y$-axis, the polar angle is the angle between X-axis and $\mathbf{n}_y$, and the azimuthal angle is the angle between Y-axis and the projection of $\mathbf{n}_y$ on the Y-Z plane,
- and for the $\mathbf{n}_z$-axis, the polar angle is the angle between Y-axis and $\mathbf{n}_z$, and the azimuthal angle is the angle between Z-axis and the projection of $\mathbf{n}_z$ on the Z-X plane.

These parameters are denoted in Table 5.1.

Axis of Probe	*Polar Angle (θ)*	*Azimuthal Angle (ϕ)*
$\mathbf{n}_{1x}$	$\pi/2 + \delta\theta_{1x}$	$\delta\phi_{1x}$
$\mathbf{n}_{1y}$	$\pi/2 + \delta\theta_{1y}$	$\delta\phi_{1y}$
$\mathbf{n}_{1z}$	$\pi/2 + \delta\theta_{1z}$	$\delta\phi_{1z}$
$\mathbf{n}_{2x}$	$\pi/2 + \delta\theta_{2x}$	$\delta\phi_{2x}$
$\mathbf{n}_{2y}$	$\pi/2 + \delta\theta_{2y}$	$\delta\phi_{2y}$
$\mathbf{n}_{2z}$	$\pi/2 + \delta\theta_{2z}$	$\delta\phi_{2z}$

Table 5.1: Hall probe misalignment parameters defined in the lab frame, where the subscripts '1' and '2' refer to the first and the second Hall probes, respectively. Note that for Hall probe 2 the coordinate system is rotated azimuthally by 45° (clockwise), i.e., the coordinate system is in fact the sector 2 frame, so that the axes of probe 2 coincide with the coordinate axes of even numbered sector frames.

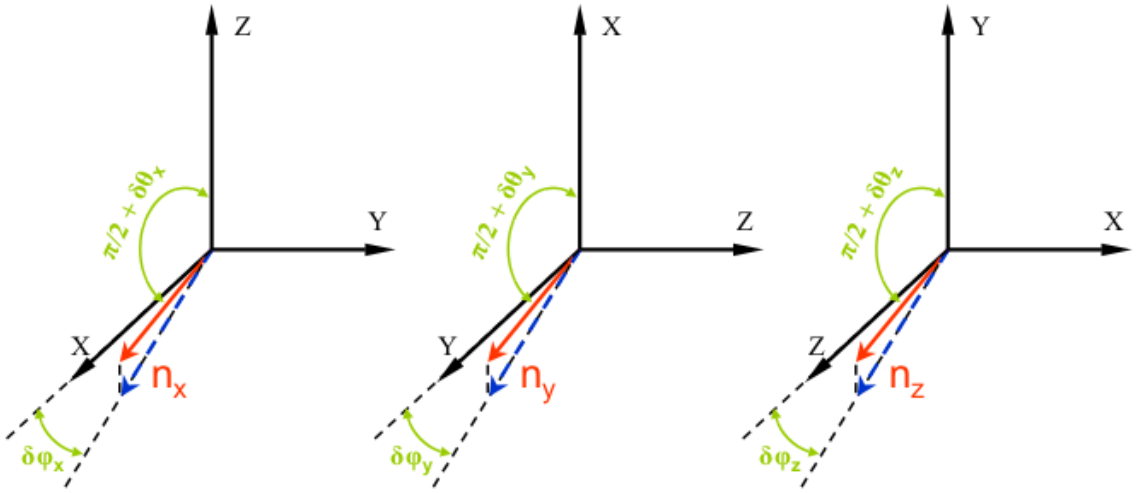

Figure 5.2: Misalignment angles for the Hall probes. The directional vector of a probe axis is indicated by a red arrow, and its projection is indicated by a blue arrow.

In general, a directional vector **n** can be expressed using the polar and azimuthal angles and unit vectors **i**, **j** and **k** as:

$$\mathbf{n} = \sin\theta\ \cos\phi\ \mathbf{i} + \sin\theta\ \sin\phi\ \mathbf{j} + \cos\theta\ \mathbf{k} \tag{5.12}$$

If the quantities, such as $\delta\theta_{1x}$, $\delta\phi_{1x}$, and so on, are assumed to be very small, we can use the small angle approximation to write out the $\mathbf{n}_x$, $\mathbf{n}_y$ and $\mathbf{n}_z$[5] as (note the canonical pattern of angles):

$$\mathbf{n}_x = \mathbf{i} + \delta\phi_x\,\mathbf{j} - \delta\theta_x\,\mathbf{k} \tag{5.13}$$

$$\mathbf{n}_y = -\delta\theta_y\,\mathbf{i} + \mathbf{j} + \delta\phi_y\,\mathbf{k} \tag{5.14}$$

$$\mathbf{n}_z = \delta\phi_z\,\mathbf{i} - \delta\theta_z\,\mathbf{j} + \mathbf{k} \tag{5.15}$$

The modified Hall probe readings will thus be $\mathbf{B}\cdot\mathbf{n}_x$, $\mathbf{B}\cdot\mathbf{n}_y$, $\mathbf{B}\cdot\mathbf{n}_z$, where **B** is expressed in the lab frame (which is coincident with the sector 1 frame), and thus the Hall probe readings are:

$$B_x^* = B_x + \delta\phi_x B_y - \delta\theta_x B_z \tag{5.16}$$

$$B_y^* = -\delta\theta_y B_x + B_y + \delta\phi_y B_z \tag{5.17}$$

$$B_z^* = \delta\phi_z B_x - \delta\theta_z B_y + B_z \tag{5.18}$$

In order to simplify the explanation, an example of working out the zero-crossing displacements and derivatives is given here. Consider a scan in the Y-direction, where B_x changes sign. We can write:

$$B_x = 0 + \Big(\frac{\partial B_x}{\partial y}\Big)_{y_0}(y - y_0) = \Big(\frac{\partial B_x}{\partial y}\Big)_{y_0}\Delta y. \tag{5.19}$$

Here, y_0 is the y-coordinate of the true zero-crossing point where $B_x = 0$, y is the y-coordinate of the apparent zero-crossing point (at $B_x^* = 0$), and $(\partial B_x/\partial y)_{y_0}$ is the field gradient at y_0 for the field component B_x in the Y-direction (this can be calculated in the field simulation programs). By substituting for B_x from equation 5.19 into equation 5.16 with $B_x^* = 0$ (because it is at the measured

[5]The subscripts for probes are omitted here.

zero-crossing point), we obtain:

$$\Delta y = \frac{-\delta\phi_x B_y + \delta\theta_x B_z}{\left(\frac{\partial B_x}{\partial y}\right)_{y_0}}. \tag{5.20}$$

From equation 5.20, we can work out the derivatives (the elements of the sensitivity matrix) for the Hall probe misalignment as:

$$\frac{\Delta y}{\delta\phi_x} = -B_y / \left(\frac{\partial B_x}{\partial y}\right)_{y_0} \tag{5.21}$$

$$\frac{\Delta y}{\delta\theta_x} = B_z / \left(\frac{\partial B_x}{\partial y}\right)_{y_0}. \tag{5.22}$$

The above are the elements with superscript $\beta = 1, 2$ and subscript $m = 10$ (Hall probe 1) or $m = 11$ (Hall probe 2) in the sensitivity matrix. Similarly, we can calculate all the quantities involving $\delta\phi_y$, $\delta\theta_y$, $\delta\phi_z$ and $\delta\theta_z$ for all the required derivatives with $m = 10, 11$ and $\beta = 1 \ldots 6$ in the sensitivity matrix. It is to be noted that the above expressions apply to sector 1, where the sector frame and lab frame coincide. For purposes of generalizing the previous results to other sectors, the Hall probe vectors $\mathbf{n}_x$, $\mathbf{n}_y$ and $\mathbf{n}_z$, as well as the magnetic field components must be re-expressed in terms of components along the **i**, **j** and **k** directions of the specific sector frame. A complete set of the directional vectors and derivatives for Hall probe misalignments are given in Appendix C.

5.2.3 Solving the Linear Equations

When all the zero-crossing displacements and derivatives are obtained, the vector **Z** and sensitivity matrix **S** are completely determined. Because there may be widely varying errors in the experimental zero-crossing positions, we must take into account these experimental uncertainties. Typically, there are many more equations (say 224) than there are unknowns. Hence a weighted least-squares fit is necessary to deduce the coil position and angle offsets when solving these linear equations. In addition, when dealing with these linear equations, the sensitivity matrix is often numerically very close to singular. This can result in the failure of some algorithms, such as the Gaussian elim-

ination, LU decomposition[6], and so on. In order to overcome these difficulties, the singular value decomposition (SVD) technique was adopted for solving equation 5.3. The relevant theory and algorithms used in our zero-crossing analysis programs can be found in the text *Numerical Recipes* (see reference [44]).

5.3 Demonstration of the Zero-Crossing Technique

The objective of the zero-crossing measurements is to determine all coil positions to $\sim \pm 1.5$ mm and coil angles to $\sim \pm 0.1^{\rm o}$. In order to verify that the zero-crossing analysis programs can correctly interpret the zero-crossing data, we have performed some tests with simulated data. The test method is as follows:

- Using the field simulation programs, we set the coil positions and orientations to be distributed randomly with rms position offset $\sigma_{XYZ} = 0.25$ cm and rms angular offset $\sigma_{ANG} = 0.1^{\rm o}$.
- The magnetic field from these new coil positions results in a new set of data for the zero-crossing points. The zero-crossing displacements are then obtained from the above zero-crossing points and the nominal ones.
- The zero-crossing analysis programs are then used to extract the coil displacements, and compare with the known values above.

Using the method above, we conducted a number of tests. The results show that the fitted coil displacements have excellent agreement with the actual (simulated) coil displacements[7]. An example is shown in Fig. 5.3, in which the recovered coil offsets agree with the starting conditions within the rounding error. Note that in this test no uncertainties were attributed to the simulated zero-crossing points.

[6]LU decomposition is a numerical analysis method for solving linear equations or finding the inverse of a matrix through writing a matrix as the product of a lower and upper triangular matrix to decompose it.

[7]Based on the experience of the magnetic field mapping for the G^0 experiment, the zero-crossing analysis technique works well for the coils displaced about several centimeters.

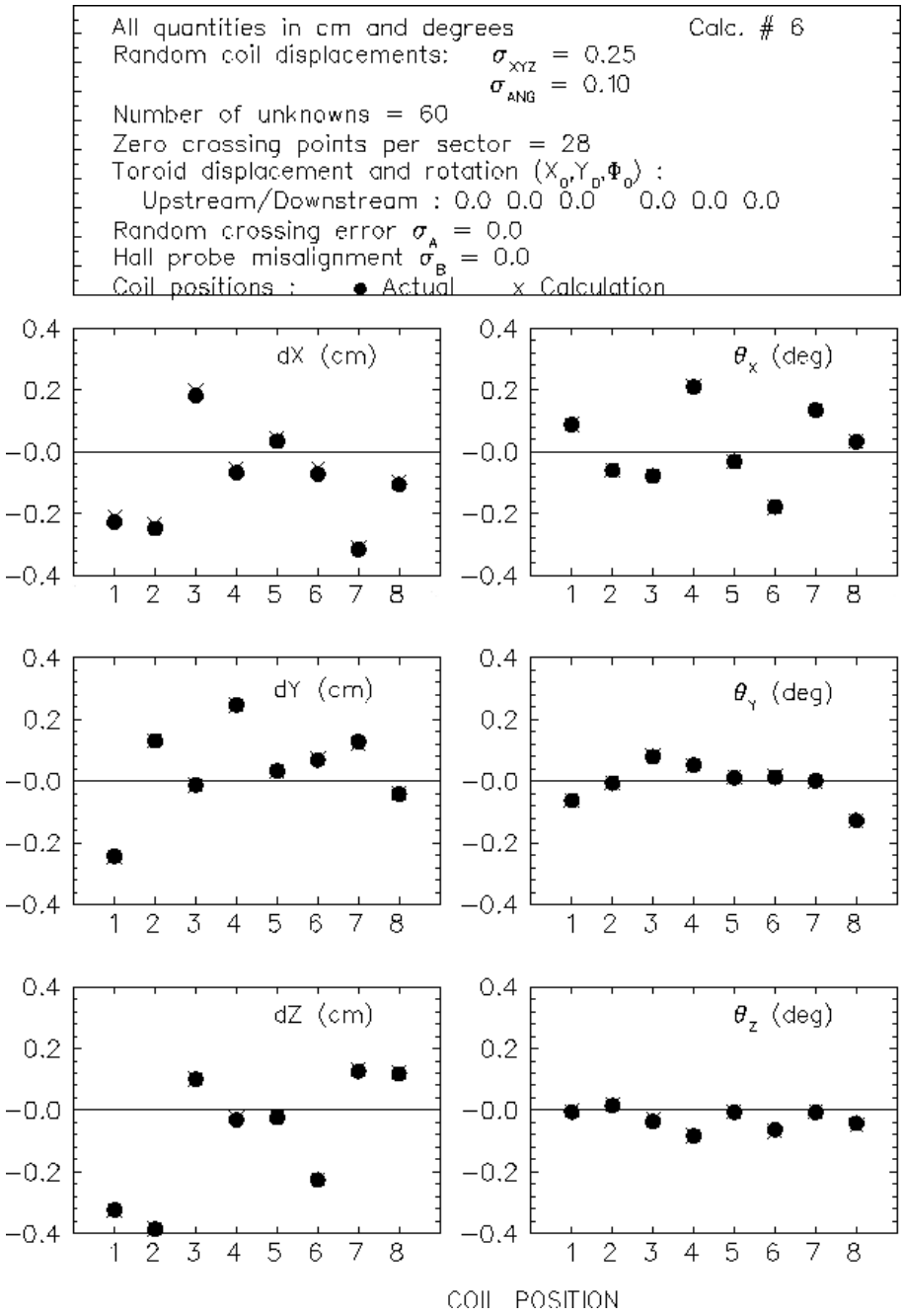

Figure 5.3: An example of reproduction of coil displacements from the simulated zero-crossing positions. The simulated coil displacements are indicated by solid circles, and the reproduced coil displacements from the simulated zero-crossing positions are indicated by crosses.

Chapter 6

Summary and Conclusion

This thesis has presented a detailed description for the magnetic field simulation and mapping of the Q^p_{Weak} experiment at Jefferson Laboratory that will provide the first precision measurement of the proton's weak charge by measuring the parity-violating asymmetry in e-p elastic scattering. The experimental background, scientific motivation and setup were discussed in Chapter 1. A key piece of apparatus in the experiment, the magnetic spectrometer (QTOR), plays the role of separating the elastic and inelastic events and focusing the elastic electrons onto the detectors for the asymmetry measurement. An in-depth numerical study of the QTOR is required for optimizing the design, installation, calibration and ultimate performance. The present study of QTOR involved the magnetic field simulation, field mapping plans and data analysis techniques, which were discussed as the principal focus for this thesis.

The QTOR has 8 coils to produce the required toroidal magnetic field for the experiment. However, the manufactured coils for the QTOR have a number of dimensional inconsistencies with respect to the design specifications. Modelling the non-regular-shaped coils then becomes the first significant challenge. A model based on the realistic coils was built through incorporating the measured dimensions of coils into the simulation programs. Many calculations were performed using this realistic coil model, and some calculated results were discussed in the thesis.

The field calculations need to be verified by experiment. An automated magnetic field mapping

device will be available to measure the field (to verify the field integrals) and map the zero-crossing points, in order to infer the coil positions and orientations in the final QTOR assembly. The field mapper includes a motion system, a probe/sensor system, and a supervisory control system, which were briefly introduced in chapter 4.

One of the most important field mapping objectives is to precisely infer the QTOR coil locations. This can be done through measuring zero-crossing positions, and then implementing the zero-crossing analysis programs. This zero-crossing analysis technique was discussed in detail in this thesis. As the QTOR has not been fully assembled and installed in the test site at MIT-Bates Laboratory, the actual magnetic field mapping can not be conducted yet. However, initial results from analyzing the simulated zero-crossing points have shown excellent agreement in reproducing the assembled coil locations.

Basically, the above investigation of the magnetic field of QTOR has provided:

- a simulated field map based on the as-built coils, which can be used in simulation studies for the Q^p_{Weak} experiment, systematic error analysis, and so on,
- a powerful tool (the package of the zero-crossing analysis programs) for the future determination of individual coil locations and adjustments when the QTOR is installed on site,
- and a set of nominal zero-crossing points as input for the zero-crossing analysis programs and the reference for the work to be done with the magnetic field mapping device.

Since the information about the manufactured coils has been incorporated into the computer codes, we can obtain an accurate field map and sets of zero-crossing points in the event that assembly conditions differ from the original design. For example, the distance from the coil centers to the beam line was recently changed from 91.44 cm to 92.71 cm as a result of experience with the initial test assembly of the magnet at the MIT-Bates, and a new field map then was produced for this condition.

The planned full installation of the QTOR at the MIT-Bates test site will take place during the summer, 2007. We are ready for the first actual field mapping at that time with these calculated

results and simulation/analysis tools on hand. All test data and experience accumulated in the first actual test will be valuable for the final field mapping when the QTOR is installed at the Q^p_{Weak} experimental site (Hall C, Jefferson Laboratory) in 2009.

Bibliography

[1] W.-M. Yao *et al.*, "The Review of Particle Physics", Journal of Physics G, 33, 1 (2006)

[2] Y. Fukuda *et al.*, "Evidence for Oscillation of Atmospheric Neutrinos", Phys. Rev. Lett., 81, 1562-1567 (1998)

[3] Nobel Web, "The Nobel Prize in Physics 1979", Website (2006), `http://nobelprize.org/nobel_prizes/physics/laureates/1979/`

[4] B. Povh *et al.*, "Particles and Nuclei: An Introduction to the Physical Concepts", 4th Edition, Springer-Verlag (2004)

[5] M. E. Peskin *et al.*, "An Introduction to Quantum Field Theory", Westview Press (1995)

[6] J. Erler *et al.*, "Weak Charge of the Proton and New Physics", Phys. Rev. D68, 016006 (2003)

[7] J. Erler and M. J. Ramsey-Musolf, "Weak Mixing Angle at Low Energies", Phys. Rev. D72, 073003 (2005)

[8] C. S. Wu *et al.*, "Experimental Test of Parity Conservation in Beta Decay", Phys. Rev., 105,1413 (1957)

[9] M. N. Rosenbluth, "High Energy Elastic Scattering of Electrons on Protons", Phys. Rev. 79, 615-619 (1950)

[10] I. A. Qattan *et al.*, "Precision Rosenbluth Measurement of the Proton Elastic Form Factors", Phys. Rev. Lett., 94, 142301 (2005)

[11] M. J. Musolf *et al.*, "Intermediate-energy Semileptonic Probes of the Hadronic Neutral Current", Phys. Rep., 239, 1 (1994)

[12] R. D. Young *et al.*, "Extracting Nucleon Strange and Anapole Form Factors from World Data", Phys. Rev. Lett., 97, 102002 (2006)

[13] S. C. Bennett *et al.*, "Measurement of the 6S $\rightarrow$ 7S Transition Polarizability in Atomic Cesium and an Improved Test of the Standard Model", Phys. Rev. Lett., 82, 2484-2487 (1999)

[14] G. P. Zeller *et al.*, "A Precise Determination of Electroweak Parameters in Neutrino-Nucleon Scattering", Phys. Rev. Lett., 88, 091802 (2002)

[15] J. T. Londergan and A. W. Thomas, "Implications of current constraints on parton charge symmetry", J. Phys. G: Nucl. Part. Phys. 31 (2005)

[16] QWEAK Collaboration, "The Q^p_{Weak} Experiment: A Search for Physics at the TeV Scale via a Measurement of Proton's Weak Charge", JLAB Report No. E-02-020, Dec. 2004

[17] CERN, "GEANT - Detector Description and Simulation Tool", CERN Geneva (1993)

[18] J. Allison *et al.*, "Geant4 Developments and Applications", IEEE Transactions on Nuclear Science, 53 No. 1 (2006)

[19] S. Agostinelli *et al.*, "Geant4 - A Simulation Toolkit", Nuclear Instruments and Methods, A 506 (2003)

[20] J. Birchall, "Qweak Document 102-v1", Nov. 2003 `http://www.jlab.org/qweak/`

[21] M. Gericke, "Qweak Document 623-v1", Jan. 2007 `http://www.jlab.org/qweak/`

[22] P. L. Anthony *et al.* [SLAC E158 Collaboration], "Observation of Parity Nonconservation in Moller Scattering", Phys. Rev. Lett. 92, 181602 (2004)

[23] P. L. Anthony *et al.* [SLAC E158 Collaboration], "Precision Measurement of the Weak Mixing Angle in Moller Scattering", Phys. Rev. Lett., 95, 081601 (2005)

[24] R. Carlini, "Qweak Document 582-v1", July 2006, `http://www.jlab.org/qweak/`

[25] W. T. H. van Oers, "Qweak Document 547-v1", Feb. 2006, `http://www.jlab.org/qweak/`

[26] A. Acha *et al.* [HAPPEX collaboration], "Precision Measurements of the Nucleon Strange Form Factors at $Q^2 \sim 0.1$ $(\mathrm{GeV})^2$", Phys. Rev. Lett. 98, 032301 (2007)

[27] K. A. Aniol *et al.* [HAPPEX Collaboration],"Constraints on the nucleon strange form factors at $Q^2 \sim 0.1$ GeV^2", Phys. Lett. B 635, 275 (2006)

[28] K. A. Aniol *et al.* [HAPPEX Collaboration], "Parity-violating electron scattering from He-4 and the strange electric form factor of the nucleon", Phys. Rev. Lett. 96, 022003 (2006)

[29] D. S. Armstrong *et al.* [G0 Collaboration], "Strange quark contributions to parity-violating asymmetries in the forward G0 electron proton scattering experiment", Phys. Rev. Lett. 95, 092001 (2005)

[30] F. E. Maas *et al.*, "Evidence for strange quark contributions to the nucleon's form factors at $Q^2 = 0.108$ $(\mathrm{GeV/c})^2$", Phys. Rev. Lett. 94, 152001 (2005)

[31] F. E. Maas *et al.* [A4 Collaboration], "Measurement of strange quark contributions to the nucleon's form factors at $Q^2 = 0.230$ $(\mathrm{GeV/c})^2$", Phys. Rev. Lett. 93, 022002 (2004)

[32] R. Alarcon, "The BLAST Project at MIT-Bates", Czech. J. Phys., 52, C517 (2002)

[33] W. Falk *et al.* "Qweak Document 596-v1", Aug. 2006, `http://www.jlab.org/qweak/`

[34] Vector Fields Limited, "OPERA-3d Reference Manual", Sept. 1999, 24 Bankside, Kidlington, Oxford, OX5 1JE, England, http://www.vectorfields.com/

[35] ANSYS, Inc., "ANSYS, Inc. Theory Reference", Nov. 2004, Southpointe, 272 Technology Drive, Canonsburg, PA 15371, USA, http://www.ansys.com/

[36] J. D. Jackson, "Classical Electrodynamics", 3rd Edition, John Wiley & Sons, Inc. (1998)

[37] T. Pang, "An Introduction to Computational Physics", Cambridge University Press (1997)

[38] L. Lee *et al.*, "The G0 magnetic field mapper project (TRIUMF/G0 design note)", G0 Internal Report G0-99-050 (1999)

[39] W. Falk and L. Lee, "Magnetic Verification of the G0 Superconducting Magnet System", G0 Internal Report G0-02-089 (2002)

[40] R. Laszewski, "On the Magnetic Verification and Acceptance Procedure for the G0 Spectometer", G0 Internal Report G0-99-020 (1999)

[41] R. Laszewski, "G0 Spectometer Dimensional Tolerances and Verification", G0 Internal Report G0-96-001 (1996)

[42] C. Schott and R. S. Popovic, "Integrated 3-D Hall Magnetic Field Sensor", Proceedings of Transducers '99 (1999)

[43] D. H. Beck, "Laser Alignment System for the Final Acceptance Magnetic Verification Test of the Superconducting Magnet System", G0 Internal Report G0-99-045 (1999)

[44] W. H. Press *et al.*, "Numerical Recipes in Fortran 77", 2nd Edition, Cambridge University Press, (1992)

Appendix A

Original QTOR Design Drawings

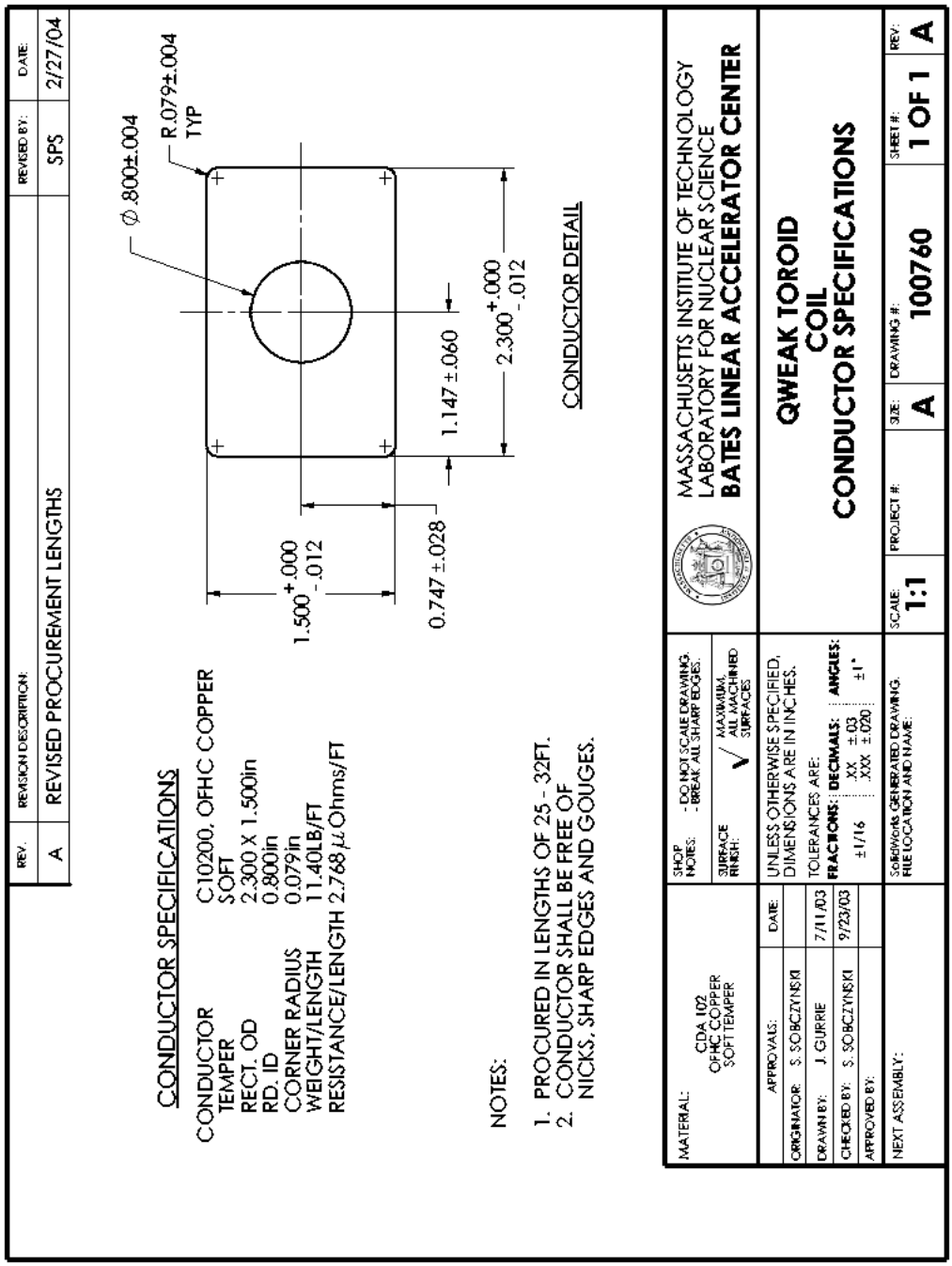

Figure A.1: Cross-section of the copper conductor

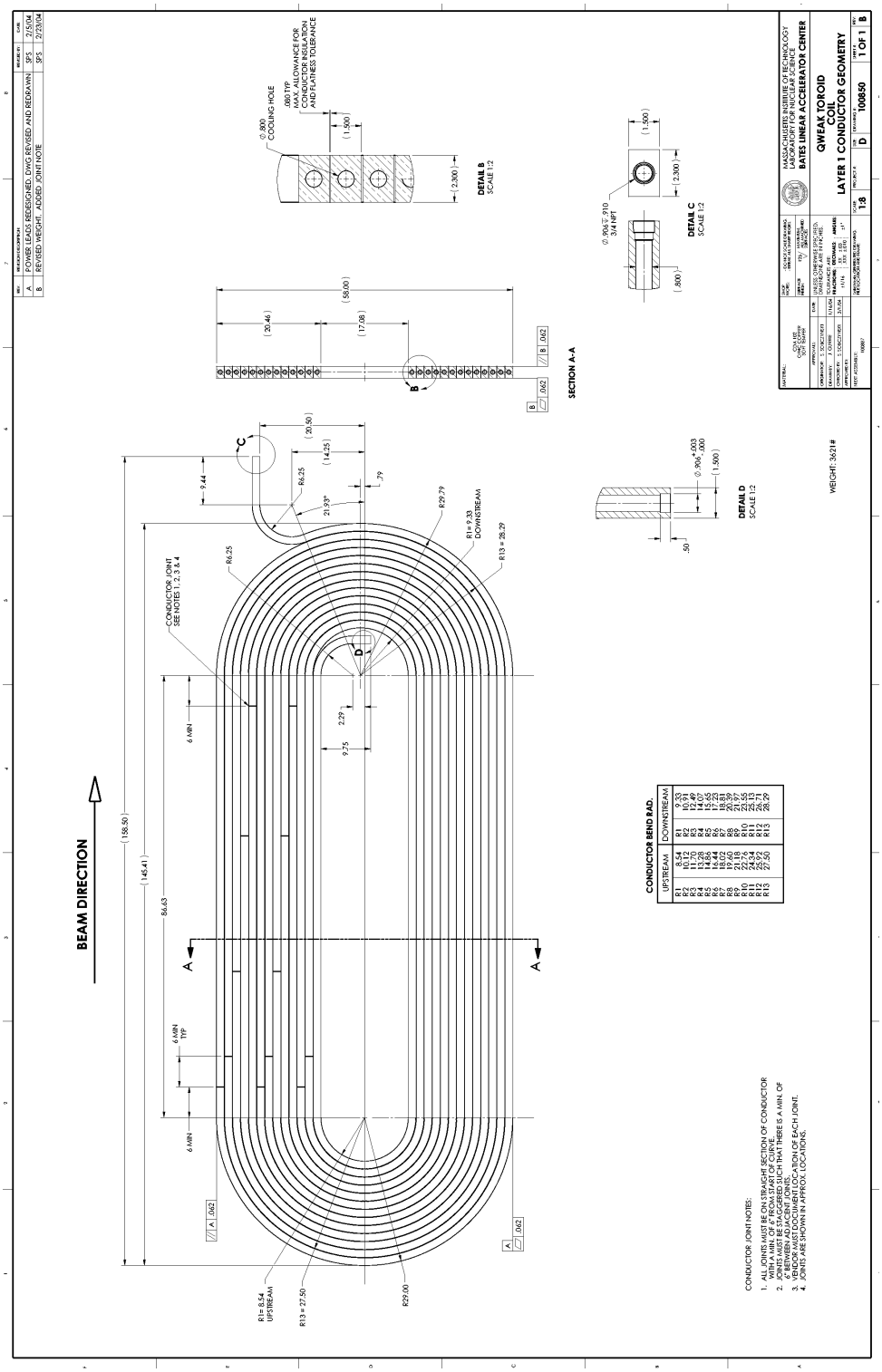

Figure A.2: Layer-1 coil conductor layout

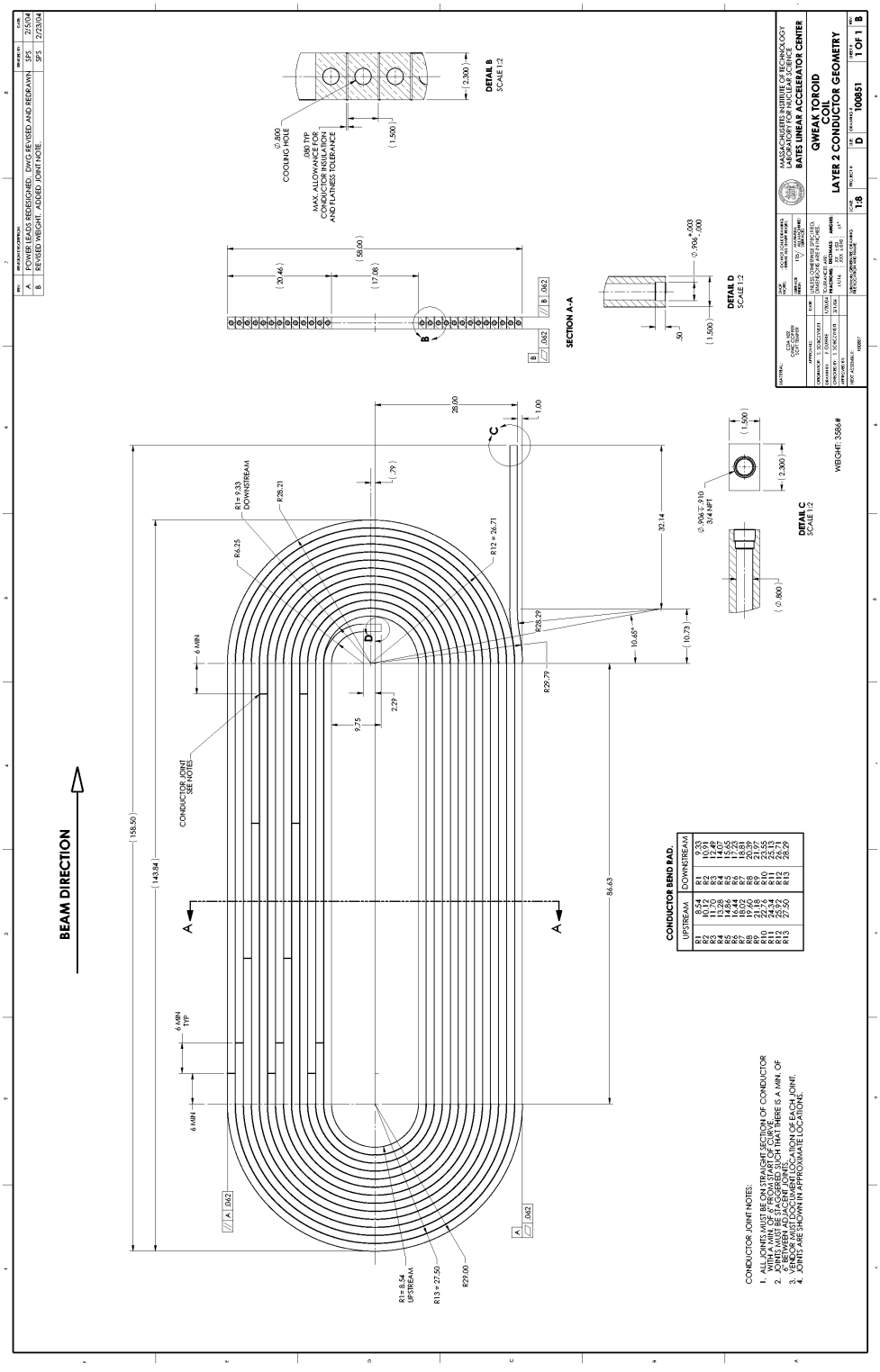

Figure A.3: Layer-2 coil conductor layout

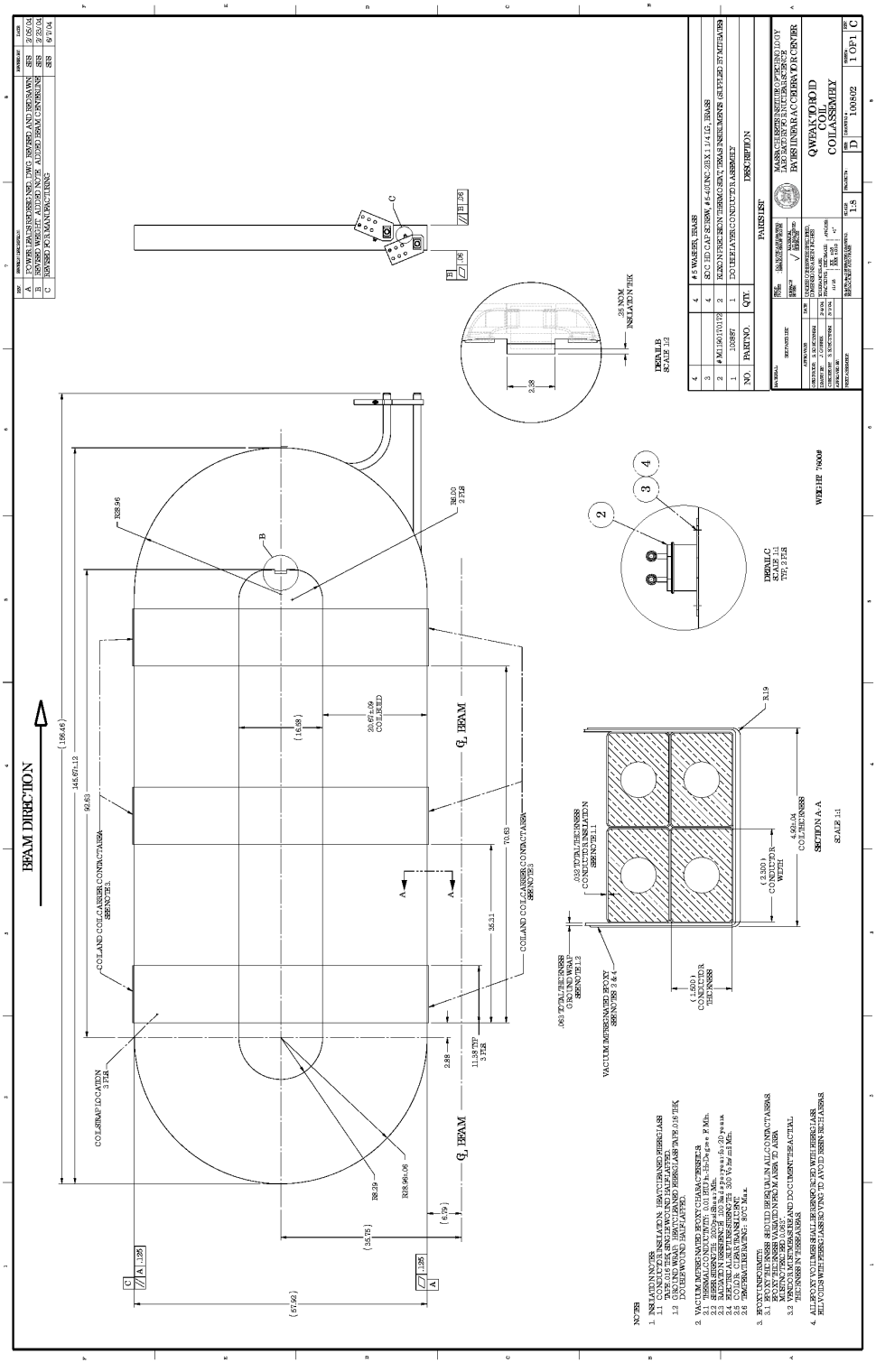

Figure A.4: Coil assembly diagram

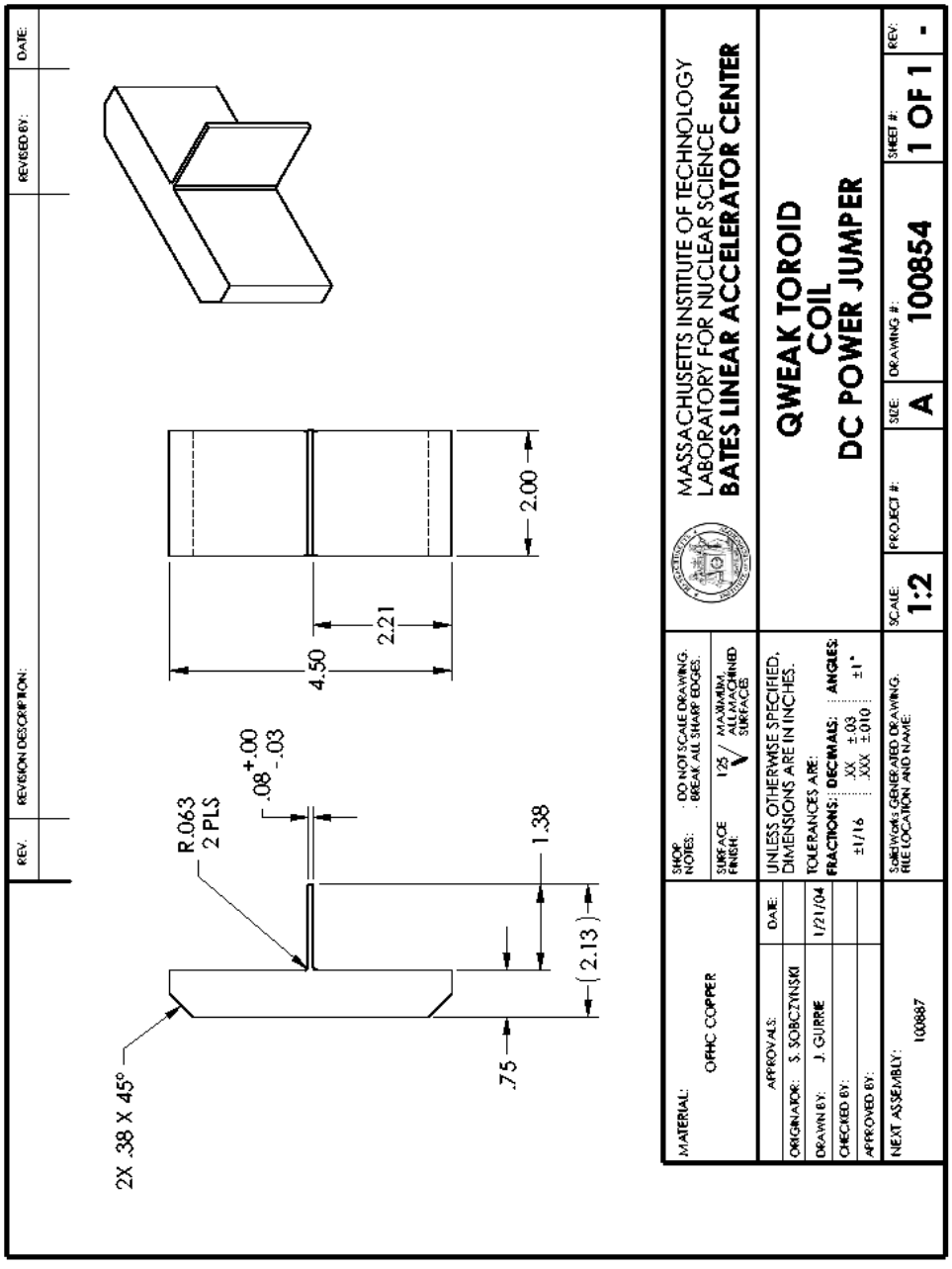

Figure A.5: Inter-pancake connection pieces

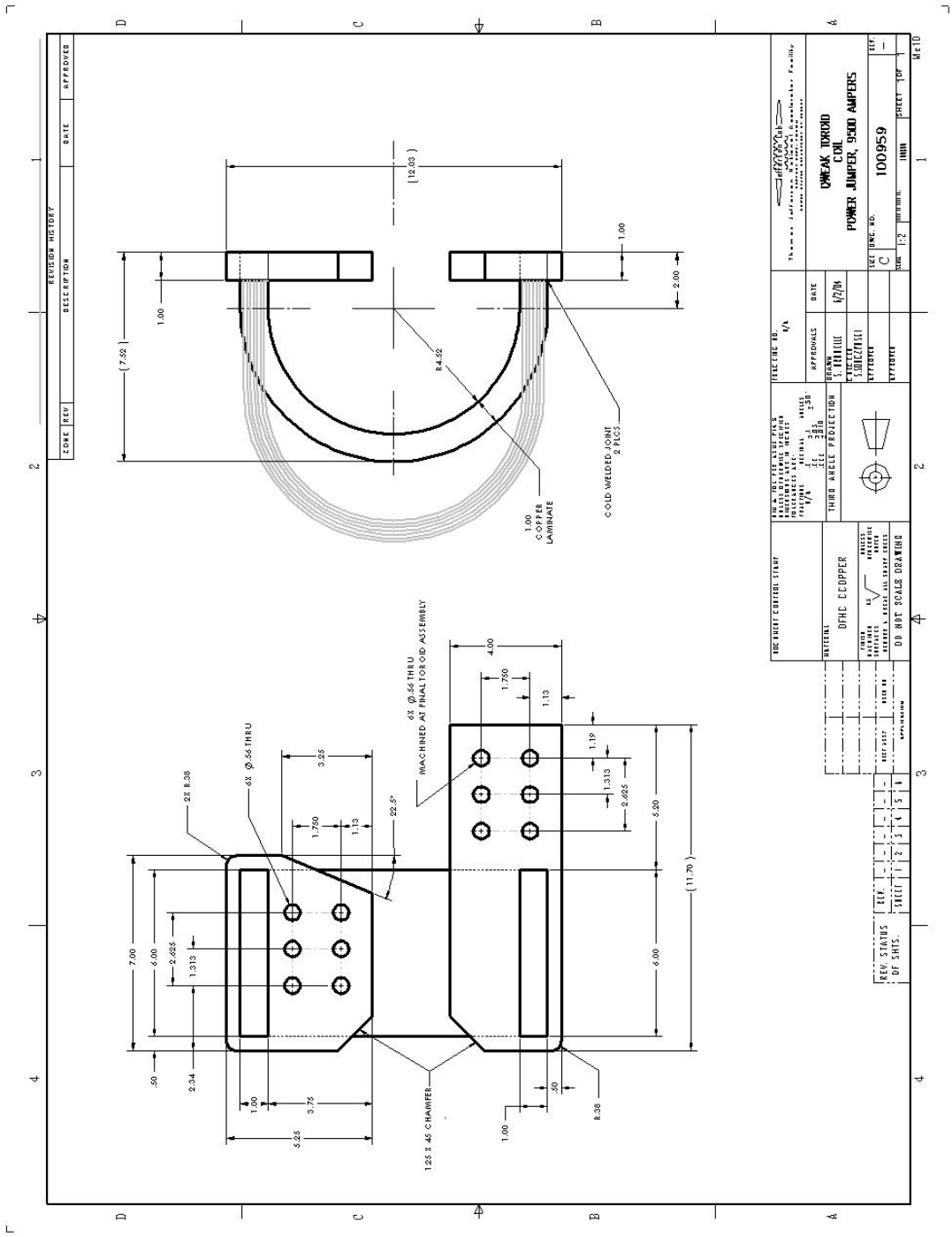

Figure A.6: Inter-coil connection elements

Appendix B

Dimensions of the Manufactured Coils

The control reports issued by the maufacturer list a set of data for the coil dimensions. Some further measurements were made on site at the MIT-Bates. The following data are the reconciled results, reduced to the bare copper dimensions (in units of mm). Fig. B.1 shows where the coil dimensions were measured, and the first column below indicates the corresponding measurement. Note that the measurements indicated by number 32 and 33, as well as the measurements indicated by number 31 for coil 2, are actually deductions made from an analysis of the other data.

Dimensions for coil layer-1 [mm]

	COIL 1	COIL 2	COIL 3	COIL 4	COIL 5	COIL 6	COIL 7	COIL 8	COIL 9	MEAN
1	441.6	441.8	440.6	443.6	445.1	444.9	442.0	442.4	440.6	442.5
2	445.6	451.5	449.2	451.9	453.0	450.9	448.3	452.2	451.3	450.4
3	443.2	452.8	449.7	449.6	452.1	450.5	450.1	453.3	452.1	450.4
4	443.2	449.4	447.4	450.7	451.6	449.4	449.1	448.9	450.5	448.9
5	437.2	442.9	443.3	444.2	444.0	444.5	442.3	441.6	444.3	442.7
6	1483.5	1481.8	1478.8	1483.9	1481.2	1479.5	1482.1	1484.2	1478.9	1481.6
7	1484.6	1484.8	1480.2	1484.7	1482.3	1484.1	1481.3	1482.4	1480.0	1482.7
8	1482.3	1485.3	1480.8	1485.2	1483.2	1485.1	1481.9	1484.0	1484.0	1483.5
9	1483.2	1485.3	1483.8	1485.0	1484.4	1484.8	1482.4	1484.7	1483.2	1484.1
10	1485.5	1485.7	1485.0	1481.8	1484.7	1484.6	1484.3	1485.2	1483.0	1484.4
11	1486.8	1484.6	1485.2	1479.9	1483.4	1483.5	1484.5	1484.1	1486.2	1484.2
12	1485.0	1483.5	1485.1	1481.9	1483.6	1483.7	1483.6	1485.2	1485.8	1484.2
13	1481.5	1482.2	1484.5	1482.8	1482.2	1485.1	1481.4	1485.3	1486.9	1483.5
14	1482.6	1482.6	1482.2	1483.0	1482.5	1485.7	1479.7	1484.8	1487.6	1483.4
15	1485.1	1483.2	1481.0	1479.0	1481.2	1484.8	1480.6	1483.4	1485.0	1482.6
16	1484.0	1482.6	1479.7	1480.4	1480.3	1481.2	1481.2	1483.9	1482.2	1481.7
17	521.0	524.1	519.2	522.4	520.2	519.1	520.4	522.5	518.0	520.8
18	516.1	518.8	515.2	515.8	515.2	516.8	517.1	516.1	514.5	516.2
19	523.6	516.0	517.4	513.7	516.0	515.0	516.8	515.8	515.9	516.7
20	522.3	515.0	517.8	516.5	515.4	517.5	515.3	519.0	518.5	517.5
21	523.3	514.9	515.5	515.9	517.2	515.8	519.1	520.9	520.6	518.1
22	521.0	515.9	519.1	517.9	516.0	515.6	519.7	519.1	520.4	518.3
23	521.2	515.1	517.8	517.3	515.5	517.4	516.8	516.1	517.8	517.2
24	520.1	515.8	518.0	516.6	515.3	517.9	517.7	515.0	518.1	517.2
25	516.5	518.2	518.2	515.6	515.4	518.4	516.0	517.1	518.2	517.1
26	523.4	524.9	521.0	520.2	519.0	520.8	519.9	521.4	517.3	520.9
27	3683.3	3677.9	3674.2	3674.9	3677.2	3676.0	3674.6	3683.5	3679.1	3677.9
28	2643.7	2643.1	2642.8	2641.6	2641.8	2641.8	2641.4	2643.5	2642.9	2642.5
29	519.3	517.3	515.6	518.1	518.8	516.3	517.4	521.1	518.9	518.1
30	520.4	517.6	515.9	515.2	516.6	517.8	515.9	518.9	517.4	517.3
31	599.3	594.4	592.2	592.7	591.0	594.8	594.4	599.8	597.9	595.2
32	2563.7	2565.9	2566.2	2567.0	2569.6	2563.3	2564.4	2564.8	2563.9	2565.4
33	2181.8	2178.1	2177.8	2175.1	2176.7	2176.3	2176.0	2180.4	2179.4	2178.0

Dimensions for coil layer-2 [mm]

	COIL 1	COIL 2	COIL 3	COIL 4	COIL 5	COIL 6	COIL 7	COIL 8	COIL 9	MEAN
1	438.1	441.0	442.8	444.9	441.6	445.2	439.9	441.4	443.4	442.0
2	443.4	449.3	452.5	452.1	452.1	451.1	449.5	451.6	448.9	450.1
3	441.0	454.3	450.5	448.6	454.0	451.3	450.8	452.2	450.4	450.4
4	440.5	447.4	449.6	446.9	450.6	451.5	447.6	449.5	448.7	448.0
5	436.4	441.4	443.7	446.1	442.4	443.9	440.1	441.6	445.4	442.3
6	1480.5	1478.8	1482.2	1482.0	1481.2	1483.8	1480.0	1484.5	1481.3	1481.6
7	1482.8	1480.0	1479.1	1482.4	1481.0	1484.0	1481.0	1481.5	1484.0	1481.8
8	1480.7	1481.2	1484.3	1485.3	1482.6	1485.9	1482.7	1483.7	1485.1	1483.5
9	1480.6	1481.3	1486.6	1482.7	1485.1	1484.9	1483.2	1484.7	1483.7	1483.6
10	1483.5	1482.8	1484.0	1481.0	1484.8	1484.5	1484.3	1485.1	1484.8	1483.9
11	1486.8	1484.9	1485.3	1479.4	1484.5	1483.9	1484.9	1485.6	1485.3	1484.5
12	1486.4	1483.0	1485.0	1479.2	1484.0	1483.1	1484.6	1484.2	1482.9	1483.6
13	1483.6	1482.3	1485.0	1480.3	1483.0	1484.3	1483.1	1483.1	1482.9	1483.1
14	1484.2	1482.2	1483.9	1482.7	1482.2	1483.7	1481.2	1485.2	1483.8	1483.2
15	1482.4	1478.5	1482.4	1483.0	1479.6	1483.2	1478.8	1483.6	1485.7	1481.9
16	1478.7	1479.7	1480.8	1480.7	1479.3	1482.5	1481.8	1483.0	1483.2	1481.1
17	520.1	517.0	517.1	519.0	520.2	517.0	519.7	519.0	515.7	518.3
18	515.6	515.9	516.9	516.0	515.3	517.4	516.2	515.9	514.9	516.0
19	521.4	515.7	516.1	516.3	515.5	516.9	516.6	517.0	517.2	517.0
20	520.5	517.7	517.3	516.2	517.1	516.2	517.4	517.5	519.5	517.7
21	518.5	518.7	517.7	518.1	518.5	521.1	521.5	522.5	522.5	519.9
22	522.3	520.6	522.3	518.0	519.4	521.5	520.5	524.0	522.1	521.2
23	521.8	516.0	516.1	515.9	516.6	516.8	517.2	516.7	520.5	517.5
24	524.5	514.8	518.6	514.4	515.0	515.8	517.6	516.3	517.7	517.2
25	522.9	517.0	517.7	518.4	514.9	516.3	517.1	517.0	515.1	517.4
26	523.8	519.7	519.5	516.6	518.5	517.5	520.1	519.0	515.2	518.9
27	3634.8	3635.2	3635.3	3633.4	3636.9	3638.5	3641.2	3641.6	3640.1	3637.5
28	2643.2	2640.8	2639.7	2642.1	2643.1	2641.0	2643.8	2642.4	2641.9	2642.0
29	474.4	475.8	478.7	475.1	477.4	480.0	478.8	479.9	479.9	477.8
30	517.2	518.8	516.9	516.3	516.4	517.5	518.8	519.2	518.3	517.7
31	554.4	553.7	549.7	554.1	553.3	560.2	558.8	557.6	558.9	555.6
32	2563.2	2562.7	2568.7	2563.1	2567.2	2560.8	2563.8	2564.8	2562.9	2564.1
33	2180.5	2177.7	2175.1	2174.2	2178.8	2175.9	2182.0	2179.3	2177.6	2177.9

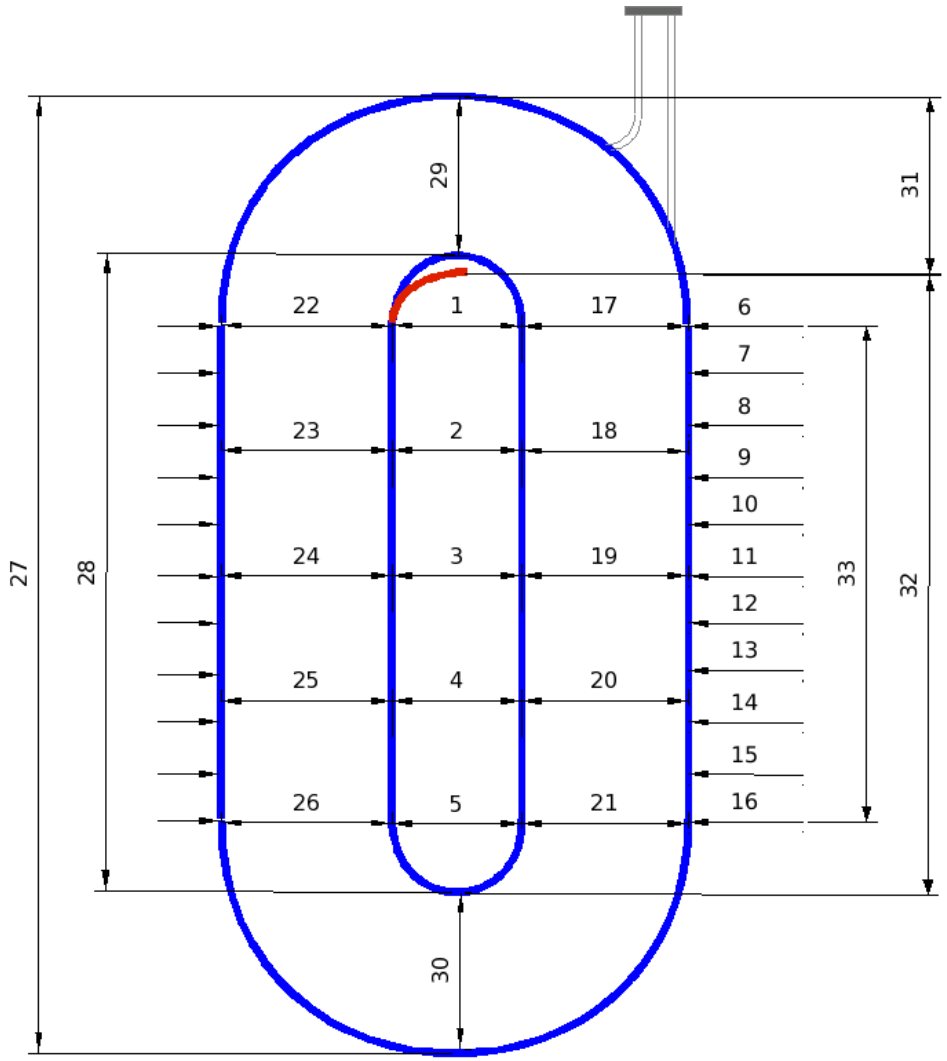

Figure B.1: Schematic of a coil, showing where the coil dimensions were measured (numbered 1 - 33). The red arc indicates the position of a quarter-turn where the layer-1 and layer-2 pancakes are connected by a copper connection bar (see Fig. A.5).

Appendix C

Directional Vectors and Derivatives for Hall Probe Misalignment Calculations

In section 5.2.2, we gave an example of working out the derivatives for the Hall probe #1 misalignment by expressing the Hall probe readings in terms of the Hall probe directional vectors (refer to equations 5.12 – 5.22). A complete set of the directional vectors and derivatives for Hall probe misalignments for probe #1 and probe #2 in different sectors at downstream and upstream positions are listed in the following tables. Note that the set of angles $\delta\theta_x$, $\delta\phi_x$, etc. is specified separately for each Hall probe. When the mapper is moved from the upstream to the downstream position, the vertical orientation of the X-axis must be preserved.

Probe # 1			
Field mapper location	Sector	Unit vectors of the sector frame in terms of unit vectors of the sector 1 frame (lab frame)	Directional vectors in terms of unit vectors of the sector frame
upstream	1	$\mathbf{i}' = \mathbf{i}$ $\mathbf{j}' = \mathbf{j}$ $\mathbf{k}' = \mathbf{k}$	$\mathbf{n}'_x = \mathbf{i}' + \delta\phi_x\,\mathbf{j}' - \delta\theta_x\,\mathbf{k}'$ $\mathbf{n}'_y = -\delta\theta_y\,\mathbf{i}' + \mathbf{j}' + \delta\phi_y\,\mathbf{k}'$ $\mathbf{n}'_z = \delta\phi_z\,\mathbf{i}' - \delta\theta_z\,\mathbf{j}' + \mathbf{k}'$
(facing downstream)	3	$\mathbf{i}' = \mathbf{j}$ $\mathbf{j}' = -\mathbf{i}$ $\mathbf{k}' = \mathbf{k}$	$\mathbf{n}'_x = -\mathbf{j}' + \delta\phi_x\,\mathbf{i}' - \delta\theta_x\,\mathbf{k}'$ $\mathbf{n}'_y = \delta\theta_y\,\mathbf{j}' + \mathbf{i}' + \delta\phi_y\,\mathbf{k}'$ $\mathbf{n}'_z = -\delta\phi_z\,\mathbf{j}' - \delta\theta_z\,\mathbf{i}' + \mathbf{k}'$
	5	$\mathbf{i}' = -\mathbf{i}$ $\mathbf{j}' = -\mathbf{j}$ $\mathbf{k}' = \mathbf{k}$	$\mathbf{n}'_x = -\mathbf{i}' - \delta\phi_x\,\mathbf{j}' - \delta\theta_x\,\mathbf{k}'$ $\mathbf{n}'_y = \delta\theta_y\mathbf{i}' - \mathbf{j}' + \delta\phi_y\,\mathbf{k}'$ $\mathbf{n}'_z = -\delta\phi_z\,\mathbf{i}' + \delta\theta_z\,\mathbf{j}' + \mathbf{k}'$
	7	$\mathbf{i}' = -\mathbf{j}$ $\mathbf{j}' = \mathbf{i}$ $\mathbf{k}' = \mathbf{k}$	$\mathbf{n}'_x = \mathbf{j}' - \delta\phi_x\,\mathbf{i}' - \delta\theta_x\,\mathbf{k}'$ $\mathbf{n}'_y = -\delta\theta_y\mathbf{j}' - \mathbf{i}' + \delta\phi_y\,\mathbf{k}'$ $\mathbf{n}'_z = \delta\phi_z\,\mathbf{j}' + \delta\theta_z\,\mathbf{i}' + \mathbf{k}'$
downstream	1	$\mathbf{i}' = \mathbf{i}$ $\mathbf{j}' = -\mathbf{j}$ $\mathbf{k}' = -\mathbf{k}$	$\mathbf{n}'_x = \mathbf{i}' - \delta\phi_x\,\mathbf{j}' + \delta\theta_x\,\mathbf{k}'$ $\mathbf{n}'_y = -\delta\theta_y\mathbf{i}' - \mathbf{j}' - \delta\phi_y\,\mathbf{k}'$ $\mathbf{n}'_z = \delta\phi_z\,\mathbf{i}' + \delta\theta_z\,\mathbf{j}' - \mathbf{k}'$
(facing upstream)	3	$\mathbf{i}' = \mathbf{j}$ $\mathbf{j}' = -\mathbf{i}$ $\mathbf{k}' = \mathbf{k}$	$\mathbf{n}'_x = -\mathbf{j}' - \delta\phi_x\,\mathbf{i}' + \delta\theta_x\,\mathbf{k}'$ $\mathbf{n}'_y = \delta\theta_y\mathbf{j}' - \mathbf{i}' - \delta\phi_y\,\mathbf{k}'$ $\mathbf{n}'_z = -\delta\phi_z\,\mathbf{j}' + \delta\theta_z\,\mathbf{i}' - \mathbf{k}'$
	5	$\mathbf{i}' = -\mathbf{i}$ $\mathbf{j}' = -\mathbf{j}$ $\mathbf{k}' = \mathbf{k}$	$\mathbf{n}'_x = -\mathbf{i}' + \delta\phi_x\,\mathbf{j}' + \delta\theta_x\,\mathbf{k}'$ $\mathbf{n}'_y = \delta\theta_y\mathbf{i}' + \mathbf{j}' - \delta\phi_y\,\mathbf{k}'$ $\mathbf{n}'_z = -\delta\phi_z\,\mathbf{i}' - \delta\theta_z\,\mathbf{j}' - \mathbf{k}'$
	7	$\mathbf{i}' = -\mathbf{j}$ $\mathbf{j}' = \mathbf{i}$ $\mathbf{k}' = \mathbf{k}$	$\mathbf{n}'_x = \mathbf{j}' + \delta\phi_x\,\mathbf{i}' + \delta\theta_x\,\mathbf{k}'$ $\mathbf{n}'_y = -\delta\theta_y\mathbf{j}' + \mathbf{i}' - \delta\phi_y\,\mathbf{k}'$ $\mathbf{n}'_z = \delta\phi_z\,\mathbf{j}' - \delta\theta_z\,\mathbf{i}' - \mathbf{k}'$

Table C.1: Directional vectors for Hall probe 1

Probe # 2			
Field mapper location	Sector	Unit vectors of the sector frame in terms of unit vectors of the sector 2 frame (lab frame rotated 45° clockwise)	Directional vectors in terms of unit vectors of the sector frame
upstream (facing downstream)	2	$\mathbf{i}' = \mathbf{i}$ $\mathbf{j}' = \mathbf{j}$ $\mathbf{k}' = \mathbf{k}$	$\mathbf{n}'_x = \mathbf{i}' + \delta\phi_x\,\mathbf{j}' - \delta\theta_x\,\mathbf{k}'$ $\mathbf{n}'_y = -\delta\theta_y\mathbf{i}' + \mathbf{j}' + \delta\phi_y\,\mathbf{k}'$ $\mathbf{n}'_z = \delta\phi_z\,\mathbf{i}' - \delta\theta_z\,\mathbf{j}' + \mathbf{k}'$
	4	$\mathbf{i}' = \mathbf{j}$ $\mathbf{j}' = -\mathbf{i}$ $\mathbf{k} = \mathbf{k}'$	$\mathbf{n}'_x = -\mathbf{j}' + \delta\phi_x\,\mathbf{i}' - \delta\theta_x\,\mathbf{k}'$ $\mathbf{n}'_y = \delta\theta_y\mathbf{j}' + \mathbf{i}' + \delta\phi_y\,\mathbf{k}'$ $\mathbf{n}'_z = -\delta\phi_z\,\mathbf{j}' - \delta\theta_z\,\mathbf{i}' + \mathbf{k}'$
	6	$\mathbf{i}' = -\mathbf{i}$ $\mathbf{j}' = -\mathbf{j}$ $\mathbf{k}' = \mathbf{k}$	$\mathbf{n}'_x = -\mathbf{i}' - \delta\phi_x\,\mathbf{j}' - \delta\theta_x\,\mathbf{k}'$ $\mathbf{n}'_y = \delta\theta_y\mathbf{i}' - \mathbf{j}' + \delta\phi_y\,\mathbf{k}'$ $\mathbf{n}'_z = -\delta\phi_z\,\mathbf{i}' + \delta\theta_z\,\mathbf{j}' + \mathbf{k}'$
	8	$\mathbf{i}' = -\mathbf{j}$ $\mathbf{j}' = \mathbf{i}$ $\mathbf{k}' = \mathbf{k}$	$\mathbf{n}'_x = \mathbf{j}' - \delta\phi_x\,\mathbf{i}' - \delta\theta_x\,\mathbf{k}'$ $\mathbf{n}'_y = -\delta\theta_y\mathbf{j}' - \mathbf{i}' + \delta\phi_y\,\mathbf{k}'$ $\mathbf{n}'_z = \delta\phi_z\,\mathbf{j}' + \delta\theta_z\,\mathbf{i}' + \mathbf{k}'$
downstream (facing upstream)	2	$\mathbf{i}' = -\mathbf{j}$ $\mathbf{j}' = -\mathbf{i}$ $\mathbf{k}' = -\mathbf{k}$	$\mathbf{n}'_x = -\mathbf{j}' - \delta\phi_x\,\mathbf{i}' + \delta\theta_x\,\mathbf{k}'$ $\mathbf{n}'_y = \delta\theta_y\mathbf{j}' - \mathbf{i}' - \delta\phi_y\,\mathbf{k}'$ $\mathbf{n}'_z = -\delta\phi_z\,\mathbf{j}' + \delta\theta_z\,\mathbf{i}' - \mathbf{k}'$
	4	$\mathbf{i}' = \mathbf{j}$ $\mathbf{j}' = -\mathbf{i}$ $\mathbf{k}' = \mathbf{k}$	$\mathbf{n}'_x = -\mathbf{i}' + \delta\phi_x\,\mathbf{j}' + \delta\theta_x\,\mathbf{k}'$ $\mathbf{n}'_y = \delta\theta_y\mathbf{i}' + \mathbf{j}' - \delta\phi_y\,\mathbf{k}'$ $\mathbf{n}'_z = -\delta\phi_z\,\mathbf{i}' - \delta\theta_z\,\mathbf{j}' - \mathbf{k}'$
	6	$\mathbf{i}' = -\mathbf{i}$ $\mathbf{j}' = -\mathbf{j}$ $\mathbf{k}' = \mathbf{k}$	$\mathbf{n}'_x = \mathbf{j}' + \delta\phi_x\,\mathbf{i}' + \delta\theta_x\,\mathbf{k}'$ $\mathbf{n}'_y = -\delta\theta_y\mathbf{j}' + \mathbf{i}' - \delta\phi_y\,\mathbf{k}'$ $\mathbf{n}'_z = \delta\phi_z\,\mathbf{j}' - \delta\theta_z\,\mathbf{i}' - \mathbf{k}'$
	8	$\mathbf{i}' = -\mathbf{j}$ $\mathbf{j}' = \mathbf{i}$ $\mathbf{k}' = \mathbf{k}$	$\mathbf{n}'_x = \mathbf{i}' - \delta\phi_x\,\mathbf{j}' + \delta\theta_x\,\mathbf{k}'$ $\mathbf{n}'_y = -\delta\theta_y\mathbf{i}' - \mathbf{j}' - \delta\phi_y\,\mathbf{k}'$ $\mathbf{n}'_z = \delta\phi_z\,\mathbf{i}' + \delta\theta_z\,\mathbf{j}' - \mathbf{k}'$

Table C.2: Directional vectors for Hall probe 2

Field mapper location: upstream										
Field component	Scan direction	Sector	Corresponding to Eqn. 5.20	$\delta\theta_x$ ×	$\delta\phi_x$ ×	$\delta\theta_y$ ×	$\delta\phi_y$ ×	$\delta\theta_z$ ×	$\delta\phi_z$ ×	Probe
		1		B_z	$-B_y$					1
		2		B_z	$-B_y$					2
		3				$-B_y$	$-B_z$			1
B_x	x	4	$\Delta x\ (\partial B_x/\partial x)$			$-B_y$	$-B_z$			2
		5	=	$-B_z$	$-B_y$					1
		6		$-B_z$	$-B_y$					2
		7				$-B_y$	B_z			1
		8				$-B_y$	B_z			2
		1		B_z	$-B_y$					1
		2		B_z	$-B_y$					2
		3				$-B_y$	$-B_z$			1
B_x	y	4	$\Delta y\ (\partial B_x/\partial y)$			$-B_y$	$-B_z$			2
		5	=	$-B_z$	$-B_y$					1
		6		$-B_z$	$-B_y$					2
		7				$-B_y$	B_z			1
		8				$-B_y$	B_z			2
		1				B_x	$-B_z$			1
		2				B_x	$-B_z$			2
		3		$-B_z$	B_x					1
B_y	y	4	$\Delta y\ (\partial B_y/\partial y)$	$-B_z$	B_x					2
		5	=			B_x	B_z			1
		6				B_x	B_z			2
		7		B_z	B_x					1
		8		B_z	B_x					2
		1						B_y	$-B_x$	1
		2						B_y	$-B_x$	2
		3						B_x	B_y	1
B_z	y	4	$\Delta y\ (\partial B_z/\partial y)$					B_x	B_y	2
		5	=					$-B_y$	B_x	1
		6						$-B_y$	B_x	2
		7						$-B_x$	$-B_y$	1
		8						$-B_x$	$-B_y$	2

Table C.3: Hall probe misalignment derivatives (upstream end of QTOR)

Field mapper location: downstream										
Field component	Scan direction	Sector	Corresponding to Eqn. 5.20	$\delta\theta_x$ ×	$\delta\phi_x$ ×	$\delta\theta_y$ ×	$\delta\phi_y$ ×	$\delta\theta_z$ ×	$\delta\phi_z$ ×	Probe
		1		$-B_z$	B_y					1
		2				B_y	$-B_z$			2
		3				B_y	$-B_z$			1
B_x	x	4	$\Delta x\ (\partial B_x/\partial x)$	B_z	B_y					2
		5	=	B_z	B_y					1
		6				B_y	B_z			2
		7				B_y	B_z			1
		8		$-B_z$	B_y					2
		1		$-B_z$	B_y					1
		2				B_y	$-B_z$			2
		3				B_y	$-B_z$			1
B_x	y	4	$\Delta y\ (\partial B_x/\partial y)$	B_z	B_y					2
		5	=	B_z	B_y					1
		6				B_y	B_z			2
		7				B_y	B_z			1
		8		$-B_z$	B_y					2
		1				$-B_x$	$-B_z$			1
		2		B_z	$-B_x$					2
		3		B_z	$-B_x$					1
B_y	y	4	$\Delta y\ (\partial B_y/\partial y)$			$-B_x$	B_z			2
		5	=			$-B_x$	B_z			1
		6		$-B_z$	$-B_x$					2
		7		$-B_z$	$-B_x$					1
		8				$-B_x$	$-B_z$			2
		1						B_y	B_x	1
		2						B_x	$-B_y$	2
		3						B_x	$-B_y$	1
B_z	y	4	$\Delta y\ (\partial B_z/\partial y)$					$-B_y$	$-B_x$	2
		5	=					$-B_y$	$-B_x$	1
		6						$-B_x$	B_y	2
		7						$-B_x$	B_y	1
		8						B_y	B_x	2

Table C.4: Hall probe misalignment derivatives (downstream end of QTOR)

Appendix D

The Q^p_{Weak} Collaboration

California Institute of Technology

Ramsey-Musolf, Michael

College of William and Mary

Armstrong, David

Averett, Todd

Capuano, Carissa

Finn, J. Michael *

Grimm, Klaus

Dartmouth College

Smith, Timothy

George Washington University

Myers, Katherine

Stokes, Burnham

Hampton University

Keppel, Cynthia

Idaho State University

Forest, Tony

Louisiana Tech University

Johnston, Kathleen

Simicevic, Neven

Wells, Steven

Massachusetts Institute of Technology

Dow, Karen

Franklin, Wilbur

Khol, Michael

Kowalski, Stanley *

Prok, Yelena

Tsentalovich, Evgeni

Mississippi State University

Dunne, James

Dutta, Dipangkar

Ohio University

King, Paul

Opper, Allena

Roche, Julie

Syracuse University

Souder, Paul

Thomas Jefferson National Accelerator Facility

Benesch, Jay

Bosted, Peter

Bruell, Antje

Carlini, Roger *

Chattopadhyay, Swapan

Ent, Rolf

Gaskell, David

Grames, Joseph

Lung, Allison

Mack, David

Majewski, Stanislaw

Meekins, David

Poelker, B.

Smith, Gregory

Suleiman, Riad

Wood, Stephen

Young, Ross

Zorn, Carl

TRIUMF

Davis, Charles

University of Connecticut

Jones, Richard

Joo, Kyungseon

University of Manitoba

Birchall, James

Falk, Willie

Gericke, Michael

Lee, Lawrence

Page, Shelley *

Pan, Jie

Ramsay, W. Desmond

van Oers, W.T.H.

Wang, Peiqing

University of Mexico

Erler, Jens

University of New Hampshire

Covrig, Silviu

Hersman, F. W.

Holtrop, Maurik

Zhu, Hongguo

University of Northern British Columbia

Korkmaz, Elie

University of Virginia

Cates, Gordon

Paschke, Kent

University of Winnipeg

Martin, Jeffery

Micherdzinska, Anna

Virginia Polytechnic Institute and State University

Mammei, Juliette

Mammei, Russell

Morgan, Norman

Pitt, Mark

Yerevan Physics Institute

Mkrtchyan, Hamlet

* The Q^p_{Weak} collaboration spokespersons